

PL-TR-97-2149

MFD-FR-97-15918

## **The Physical Basis for the Lg/P Discriminant: Signal Characteristics and Modeling**

**Theron J. Bennett  
Keith L. McLaughlin  
Ronald W. Cook  
Jerry A. Carter**

**Maxwell Technologies, Inc.  
8888 Balboa Ave.  
San Diego, CA 92123-1506**

**November, 1997**

**Final Report**

**31 July 1995 - 31 July 1997**

**19980630 027**

**Approved for public release; distribution unlimited**



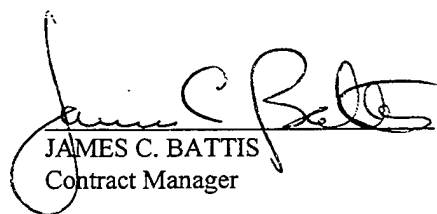
**AIR FORCE RESEARCH LABORATORY  
Space Vehicles Directorate  
29 Randolph Road  
AIR FORCE MATERIEL COMMAND  
HANSCOM AFB, MA 01731-3010**

SPONSORED BY  
Air Force Technical Applications Center  
Directorate of Nuclear Treaty Monitoring  
Project Authorization T/5101

MONITORED BY  
Air Force Research Laboratory  
CONTRACT No. F19628-95-C-0107

The views and conclusions contained in this document are those of the authors and should not be interpreted as representing the official policies, either express or implied, of the Air Force or U.S. Government.

This technical report has been reviewed and is approved for publication.



JAMES C. BATTIS  
Contract Manager



CHARLES P. PIKE, Deputy Director  
Integration and Operations Division

This report has been reviewed by the ESD Public Affairs Office (PA) and is releasable to the National Technical Information Service (NTIS).

Qualified requestors may obtain copies from the Defense Technical Information Center. All others should apply to the National Technical Information Service.

If your address has changed, or you wish to be removed from the mailing list, or if the addressee is no longer employed by your organization, please notify AFRL/VSOE, 29 Randolph Road, Hanscom AFB, MA 01731-3010. This will assist us in maintaining a current mailing list.

Do not return copies of the report unless contractual obligations or notices on a specific document requires that it be returned.

# REPORT DOCUMENTATION PAGE

*Form Approved  
OMB No. 0704-0188*

Public reporting burden for this collection of information is estimated to average 1 hour per response, including the time for reviewing instructions, searching existing data sources, gathering and maintaining the data needed, and completing and reviewing the collection of information. Send comments regarding this burden estimate or any other aspect of this collection of information, including suggestions for reducing this burden, to Washington Headquarters Services, Directorate for Information Operations and Reports, 1215 Jefferson Davis Highway, Suite 1204, Arlington, VA 22202-4302, and to the Office of Management and Budget, Paperwork Reduction Project (0704-0188), Washington, DC 20503.

1. AGENCY USE ONLY (Leave blank)			2. REPORT DATE November, 1997	3. REPORT TYPE AND DATES COVERED Final Report 7/31/95 - 7/31/97	
4. TITLE AND SUBTITLE The Physical Basis for the Lg/P Discriminant: Signal Characteristics and Modeling			5. FUNDING NUMBERS Contract No. F19628-95-C-0107 PE 35999F PR 5101 TA GM WU AG		
6. AUTHOR(S) Theron J. Bennett, Keith L. McLaughlin, Ronald W. Cook, and Jerry A. Carter			8. PERFORMING ORGANIZATION REPORT NUMBER MFD-FR-97-15918		
7. PERFORMING ORGANIZATION NAME(S) AND ADDRESS(ES) Maxwell Technologies, Inc. 8888 Balboa Avenue San Diego, CA 92123-1514			10. SPONSORING/MONITORING AGENCY REPORT NUMBER PL-TR-97-2149		
9. SPONSORING/MONITORING AGENCY NAME(S) AND ADDRESS(ES) Air Force Research Laboratory 29 Randolph Road Hanscom AFB, MA 01731-3010 Contract Manager: James C. Battis/VSBI					
11. SUPPLEMENTARY NOTES					
12a. DISTRIBUTION/AVAILABILITY STATEMENT Approved for public release; distribution unlimited			12b. DISTRIBUTION CODE		
13. ABSTRACT (Maximum 200 words) Effective monitoring of the Comprehensive Test Ban Treaty (CTBT) for low-magnitude events can only be achieved through the use of regional seismic observations. One of the most widely heralded regional discrimination techniques is based on the measurement of Lg/P ratios at regional seismic stations. Although this technique seems to separate events of different source types in many geographic regions, the physical basis for the discriminant and the significance of regional propagation effects on the ratio measurements have generally not been resolved. This study has sought to determine the salient characteristics of Lg/P ratios as a function of frequency for events of different source types from various geographic regions, to assess how the measurements should have been affected by propagation path conditions, and to analyze the results in terms of physical properties of the seismic source mechanism and the propagation path.					
14. SUBJECT TERMS Seismic Discrimination      Regional Lg/P      Spectra Mechanism      Source Propagation				15. NUMBER OF PAGES 98	
				16. PRICE CODE	
17. SECURITY CLASSIFICATION OF REPORT UNCLASSIFIED		18. SECURITY CLASSIFICATION OF THIS PAGE UNCLASSIFIED		19. SECURITY CLASSIFICATION OF ABSTRACT UNCLASSIFIED	
				20. LIMITATION OF ABSTRACT UNLIMITED	

## Table of Contents

	<u>Page</u>
1. Introduction.....	1
1.1 Objectives.....	1
1.2 Accomplishments.....	2
1.3 Report Organization.....	4
2. Database for Regional Discrimination.....	5
2.1 Limitations on Regional Data for Discrimination Studies.....	5
2.2 Data Used for These Studies.....	6
3. Analyses of the Observed Behavior of $L_g/P$ Ratios.....	9
3.1 Background .....	9
3.2 Processing Scheme for $L_g/P$ Ratio Measurements.....	10
3.3 Corrections of $L_g/P$ Ratios for Path Attenuation.....	17
3.3.1 Model for Attenuation Corrections.....	17
3.3.2 Effects of Attenuation Corrections on Observed $L_g/P_g$ Ratios.....	29
4. Theoretical Modeling of $L_g/P_g$ Ratio Behavior.....	34
4.1 Constraints on $Q(L_g)$ -vs- $Q(P_g)$ From $L_g/P_g$ Ratio Observations.....	34
4.2 Synthetic Amplitudes from a World-Wide Collection of Crustal Models.	35
4.3 Random Layering and Choice of a $Q(f,z)$ Model.....	43
4.4 "Empirical" Models of Excitation and Attenuation Based on Synthetic $L_g$ and $P_g$ .....	49
4.5 Clustering Based on Explosion-Earthquake $L_g/P_g$ Ratios.....	57
4.6 Discussion of Theoretical Modeling Results.....	57
5. Discrimination Analysis of the August 16, 1997 Kara Sea Event.....	63
5.1 General Characteristics of Regional Waveform Data.....	63
5.2 Comparison of Band-Pass Filter Results.....	64
5.3 S/P Ratios.....	68
5.4 Horizontal Shear-Wave Observations.....	73
5.5 Results of Discrimination Analysis.....	73

6. Summary and Recommendations.....	75
6.1 Summary of Main Findings.....	75
6.2 Recommendations.....	77
7. References.....	80

## List of Illustrations

		<u>Page</u>
1	Locations of selected explosions, earthquakes, and stations used in analyzing regional signals from western U.S. events.	7
2	Locations of selected explosions, earthquakes, and stations used in analyzing regional signals from Eurasian events.	8
3a	Average $L_g/P_g$ ratios as a function of filter center frequency determined from traditional broad band-pass filter analysis for nuclear explosions in the western U.S. and Eurasia (adapted from Bennett et al., 1997a).	11
3b	Average $L_g/P_g$ ratios as a function of filter center frequency determined from traditional broad band-pass filter analysis for earthquakes in the U.S. and Eurasia (adapted from Bennett et al., 1997a).	12
4	Comparison of $L_g/P_g$ ratios as a function of frequency from peak amplitude (top) and RMS amplitude (bottom) measurements derived using broad band-pass filters for NTS explosions recorded at LLNL station KNB.	14
5	Comparison of $L_g/P_g$ ratios as a function of frequency using narrow band-pass Gaussian filters (top) and Fourier analyses (bottom) for NTS explosions recorded at LLNL station KNB.	16
6	Attenuation at 1 Hz ( $Q_0$ ) from $L_g$ coda adapted from coda-Q studies of Mitchell et al. (cf. Xie and Mitchell, 1990; Mitchell et al., 1996).	21
7	Frequency dependence of attenuation ( $\eta$ ) from $L_g$ coda adapted from work by Mitchell et al. (cf. Xie and Mitchell, 1990; Mitchell et al., 1996).	22
8	Predicted $L_g/P_g$ attenuation correction factors in the surrounding region of a source at NTS for four frequencies assuming $Q_{Pg} = 1.67 Q_{Lg}$ .	24
9	Predicted $L_g/P_g$ attenuation correction factors in the surrounding region of a source at Lop Nor China for four frequencies assuming $Q_{Pg} = 1.67 Q_{Lg}$ .	25
10	Predicted differences in $L_g/P_g$ attenuation correction factors in the surrounding region of a source at NTS for four frequencies based on assumptions of $Q_{Pg} = 2.25 Q_{Lg}$ and of $Q_{Pg} = 1.0 Q_{Lg}$ .	27

11 Predicted differences in  $L_g/P_g$  attenuation correction factors in the surrounding region of a source at Lop Nor China for four frequencies based on assumptions of  $Q_{Pg} = 2.25 Q_{Lg}$  and of  $Q_{Pg} = 1.0 Q_{Lg}$ . 28

12  $L_g/P_g$  ratios as a function of frequency at station KNB for 5 NTS explosions after corrections for attenuation. 31

13  $L_g/P_g$  ratios as a function of frequency at station KNB for 5 earthquakes near NTS after corrections for attenuation. 32

14 Comparison of mean and standard deviations for  $L_g/P_g$  ratios as a function of frequency for NTS explosions and nearby earthquakes recorded at LLNL station KNB before (top) and after (bottom) corrections for attenuation. 33

15 Predicted  $L_g/P_g$  spectral ratios normalized to 1 at 1 Hz for  $Q_{Lg} = 500*f^n$ , for two ratios of  $Q_{Lg}/Q_{Pg}$  and two values of  $\eta$ .  $L_g/P_g$  ratios fall off too quickly as a function of increasing frequency if  $Q$  is independent of frequency,  $\eta = 0$ . 36

16 Map showing the Mooney et al. (1997) world-wide regionalization for the two letter code representative models listed in Table 1. Only the continental models were used to construct regional synthetics for  $L_g/P_g$  analysis. 42

17 The D2 crustal model with and without a 5% RMS random velocity variation used to construct regional synthetics. Shear Q at 1 Hz and density are shown on the left while shear and compressional velocities are shown on the right. 44

18 Comparison of synthetic seismograms with and without the 5% random velocity variation in the layered model shown in Figure 17. Note the more developed  $P_n$  signals and the reduced "spikes" in the  $P_g$  from the randomized structure. 45

19 Comparison of synthetic seismograms with and without the 5% random velocity variation in the layered model shown in Figure 17. Note that the more developed  $S_n$  arrival from the random layered structure and that the isolated "spikes" in the  $L_g$  signal are reduced. 45

20  $L_g/P_g$  earthquake spectral ratios at 600 km for crustal model DA with 0, 2.5, 5.0 7.5, and 10% RMS random layering. General character of the  $L_g/P_g$  spectral ratio is unaffected by the random layering. 46

21  $L_g/P_g$  explosion spectral ratios at 400 km for crustal model DA with 0, 2.5, 5.0 7.5, and 10% RMS random layering. Shallow sediments in this model exhibit a rather large resonance for an explosion source at 1 km depth. 46

22 Comparison of vertical component synthetics (high pass at 0.5 Hz) at 200 km for three  $Q(f)$  models and the randomized crustal velocity model D2 shown in Figure 17. A dip-slip double-couple source (Gzds) at 15 km depth is shown above and an explosive source (Gzi) at 1 km depth is shown below. The earthquake  $L_g$  amplitude is significantly increased relative to the  $P_g$  amplitude for the  $\eta=0.5$ ,  $Q_0=\beta/5$ ,  $Q$  model. The high  $Q$  surface layer model does not sufficiently attenuate the late arriving fundamental surface waves excited by the shallow explosive source. Also, it is clear that the  $\eta=0$ ,  $Q_0=\beta/10$ , high  $Q$  surface layer model contains much shallow propagating energy in the  $Lg$  window that is absent in the low  $Q$  surface models. 47

23 Comparison of vertical component synthetics (high pass at 3.0 Hz) at 200 km for three  $Q(f)$  models and the randomized crustal velocity model D2 shown in Figure 17. A dip-slip double-couple source (Gzds) at 15 km depth is shown above and an explosive source (Gzi) at 1 km depth is shown below. Earthquake  $L_g/P_g$  ratios greater than 1 at frequencies above 3 Hz favor either the  $\eta=0.5$ ,  $Q_0=\beta/5$  or  $\eta=0.0$ ,  $Q_0=\beta/5$  models over the  $\eta=0.0$ ,  $Q_0=\beta/10$  model. Even at frequencies above 3 Hz, the shallow explosion Green's function for the high  $Q$  surface layer model contains shallow propagating energy in the  $Lg$  window not apparent in the low  $Q$  surface layer models. 48

24 Log-likelihood as a function of the model parameters,  $Q_0$  and  $\eta$ , for empirical  $L_g$  and  $P_g$   $Q$  models,  $Q(f) = Q_0 * f^n$ , based on fits to synthetic  $L_g$  and  $P_g$  amplitude versus frequency and distance time-domain measurements for a dip-slip double-couple at a depth of 15 km in the crustal model D2. The inversion assumed  $n=5/6$ . Note the elongate contours and trade-off between  $Q_0$  and  $\eta$ . 51

25  $L_g$   $Q_0$  and  $\eta$  model estimates for all crustal models. Three kinds of double-couple earthquake sources are shown with depth of 10 km and dip-slip, strike-slip, and 45 degree thrust/reverse orientations. The dip-slip orientations show a systematically lower  $Q_0$  and higher  $\eta$ . 53

26  $P_g$   $Q_0$  and  $\eta$  model estimates for all crustal models. Three kinds of double-couple earthquake sources are shown with depth of 10 km and dip-slip, strike-slip, and 45 degree thrust/reverse orientations. The dip-slip orientations show a systematically lower  $Q_0$  and higher  $\eta$ . 53

27  $L_g Q_0$  versus  $P_g Q_0$  model estimates for all crustal models. Three kinds of double-couple earthquake sources are shown with depth of 10 km and dip-slip, strike-slip, and 45 degree thrust/reverse orientations. The dip-slip mechanisms have the largest scatter of the three mechanisms. 54

28  $L_g \eta$  versus  $P_g \eta$  model estimates for all crustal models. Three kinds of double-couple earthquake sources are shown with depth of 10 km and dip-slip, strike-slip, and 45 degree thrust/reverse orientations. 54

29  $L_g Q_0$  and  $\eta$  model estimates for all crustal models. Three kinds of shallow axi-symmetric source are shown with depth of 1 km, explosion (EXP), horizontal tension crack (TC), and compensated linear vector dipole (CLVD). There does not appear to be any systematic differences in the attenuation as a function of mechanism. There is, however, a strong trade-off between  $Q_0$  and  $\eta$ . 55

30  $P_g Q_0$  and  $\eta$  model estimates for all crustal models. Three kinds of shallow axi-symmetric source are shown with depth of 1 km, explosion (EXP), horizontal tension crack (TC), and compensated linear vector dipole (CLVD). There does not appear to be any systematic differences in the attenuation as a function of mechanism. There is however a strong trade-off between  $Q_0$  and  $\eta$ . The results are somewhat more scattered than the  $L_g Q_0$  and  $\eta$  estimates. 55

31  $L_g Q_0$  versus  $P_g Q_0$  model estimates for all crustal models. Three kinds of shallow axi-symmetric source are shown with depth of 1 km, explosion (EXP), horizontal tension crack (TC), and compensated linear vector dipole (CLVD). There does not appear to be any systematic differences in the attenuation as a function of mechanism. The  $P_g Q_0$  values are somewhat more scattered than the  $L_g Q_0$  values. 56

32  $L_g \eta$  versus  $P_g \eta$  model estimates for all crustal models. Three kinds of shallow axi-symmetric source are shown with depth of 1 km, explosion (EXP), horizontal tension crack (TC), and compensated linear vector dipole (CLVD). There does not appear to be any systematic differences in the attenuation as a function of mechanism. The  $P_g \eta$  values are somewhat more scattered than the  $L_g \eta$  values. 56

33 A cluster diagram for the data set of  $L_g/P_g$  ratios at 400 km at 1-2, 2-4 and 4-6 Hz bandpasses. The  $L_g/P_g$  ratios fall into three natural clusters. 58

34 Group 1 consists of majority of models with surface sedimentary layers thicker than 1 km. 58

35	Group 2 consists of models with thin sedimentary layers at the surface underlain by high velocities.	59
36	Group 3 consists of a small number of models with high velocities at the free surface.	59
37	Plot of Explosion $L_g/P_g$ ratio versus dip-slip $L_g/P_g$ ratios in the 1-2 Hz passband for all models. All but a small number of Group #2 models have earthquake $L_g/P_g$ ratios greater than unity in this bandpass. Many of the models in Group #1 have explosion $L_g/P_g$ ratios greater than unity.	60
38	Plot of Explosion $L_g/P_g$ ratio versus dip-slip $L_g/P_g$ ratios in the 2-4 Hz bandpass for all models. All but a small number of Group #1 and #2 models have earthquake $L_g/P_g$ ratios greater than unity in this passband. Only a few of the models in Group #1 have explosion $L_g/P_g$ ratios greater than unity.	60
39	Plot of Explosion $L_g/P_g$ ratio versus dip-slip $L_g/P_g$ ratios in the 4-6 Hz bandpass for all models. All models have earthquake $L_g/P_g$ ratios greater than 0.7. Only two in Group #1 have similar explosion and earthquake $L_g/P_g$ ratios near unity.	61
40	Distribution of the three groupings of models, Cross = Group #1, Solid Triangle = Group #2, and Solid Diamond = Group #3. Grouping/clustering is based upon $L_g/P_g$ ratios of explosion and earthquake sources in three bandwidths.	62
41	Events used in regional signal comparisons for the Kara Sea event of 1997/08/16.	65
42	Comparison of band-pass filter analyses of the signals at station KEV for the 1997/08/16 Kara Sea event (top) and the 1990/10/24 NZ nuclear test (bottom).	66
43	Comparison of band-pass filter analyses of the signals at station NRA0 for the 1997/08/16 Kara Sea event (top) and the 1990/10/24 NZ nuclear test (bottom).	67
44	S/P ratios as a function of frequency observed at 7 regional stations from the 1997/08/16 Kara Sea event.	69
45	S/P ratios as a function of frequency observed at 4 regional stations from 1990/10/24 NZ nuclear test.	70

46	S/P ratios as a function of frequency observed at 4 regional stations from the 1992/12/31 event near NZ.	71
47	S/P ratios as a function of frequency observed at 4 regional stations from the 1995/06/13 event near NZ.	72
48	Horizontal-component records (4-8 Hz passband) at the 4 best regional stations for the 1997/08/16 Kara Sea event.	74

## List of Tables

1	Listing of Mooney et al. (1997) Crust 5.1 representative models with “two-letter” designations used in the current work.	37
---	--	----

## 1. Introduction

### 1.1 Objectives

Regional discrimination methods for distinguishing different types of seismic sources, including potential underground nuclear explosions, earthquakes, chemical explosions, and rockbursts, will provide an important tool for monitoring the Comprehensive Test Ban Treaty (CTBT). Although regional discrimination procedures have been studied for many years, there remain many outstanding issues which need to be resolved before these methods can be relied on for identifying seismic sources. Development of regional discrimination techniques has been impeded by limitations on the database available for testing proposed discriminant measures and by the lack of theoretical understanding of the dependence of regional phase behavior on physical properties of the source and propagation path. In the research project reported here, we have sought to investigate the physical basis for  $L_g/P$  ratio measurements as regional discriminants. Such measurements have been one of the most enduring and promising of the proposed methods. We believe that improving understanding of the effects of source conditions and propagation can make  $L_g/P$  ratios a reliable discrimination technique for widespread application.

To accomplish these research objectives, the program included an empirical element to describe the characteristics of  $L_g/P$  ratios as a function of frequency observed from different types of seismic sources and for various propagation paths representative of those which will be encountered in global CTBT monitoring. In these empirical studies, we developed a consistent procedure to determine spectral  $L_g/P$  ratios and established a basis to correct the  $L_g/P$  measurements for prior knowledge of regional attenuation. The second element of the research program involved the use of theoretical modeling techniques to predict the dependence of  $L_g/P$  ratios on source mechanisms and propagation properties. We attempted to use the observed regional phase behavior to constrain the theoretical models and to investigate the sensitivity of the ratios to the physical behavior in different seismic source mechanisms and to propagation conditions in different tectonic regions. Such physical understanding is critical to knowing why and

where the discriminant will work and what might cause observed discriminant measures to vary from the expected behavior.

### 1.2 Accomplishments

In the empirical element of this research program, we collected regional waveform data from different source types including nuclear explosions, earthquakes, rockbursts, and chemical blasts for a variety of propagation conditions. We have analyzed the distribution of this database with respect to source types, epicentral distances, and tectonic regions. Nuclear explosions in the database were limited to a few source areas (viz. the Nevada Test Site (NTS) in the United States, the former Soviet test sites in eastern Kazakhstan and at Novaya Zemlya, and the Chinese test site at Lop Nor). In addition, the data included several PNE explosions in the former Soviet Union recorded at a single regional station. The observations were recorded at near and intermediate regional distances for NTS, at intermediate and far-regional distances from the former Soviet test sites, and at intermediate and far-regional distances from the Lop Nor explosions. For comparison, earthquakes and other source types in the same or similar tectonic regions and at comparable epicentral distances have been analyzed using consistent procedures. We determined preliminary  $L_g/P$  ratios for different source types using a band-pass filtering procedure during the first phase of this research. These observations showed differences in the  $L_g/P$  ratio measurements as a function of frequency between the different source types, but there were also differences between similar source types in different regions. For the  $L_g/P$  ratio discriminant to be effective, these kinds of differences would need to be resolved.

One way to reduce the variability for common source types might be through refined measurement procedures. As part of the empirical element of this research program, we tested several alternative algorithms for obtaining spectral estimates to use in forming the  $L_g/P$  ratios; and we have settled on a systematic scheme which utilizes fairly narrow Gaussian filters, for which the RMS output amplitudes tend to match Fourier spectral estimates computed for the corresponding regional phase group velocity windows. This band-pass filtering procedure appears to offer some operational

advantages; however, it did not seem to change the measurements of the  $L_g/P$  ratios and would not improve the variability between observations for similar source types in different regions. Although spectral  $L_g/P$  ratios are relatively unaffected by differences in the source magnitudes and the seismic station recording system, they can be strongly affected by propagation characteristics. In these studies, we used a model of regional phase attenuation to analyze the effects of propagation on the  $L_g/P_g$  ratio measurements as a function of frequency and to correct the  $L_g/P_g$  ratio measurements for selected events. These analyses showed that predicted attenuation corrections can have a great effect on  $L_g/P_g$  ratio measurements as a function of frequency. We found that such corrections altered  $L_g/P_g$  ratios, with greatest effects at higher frequencies, and that there appeared to be some tendency for corrections to reduce the scatter between stations for individual events. The results suggested that even more significant reductions in  $L_g/P_g$  scatter may be achievable when the stations are at larger epicentral distances; however, more precise knowledge of  $P_g$  attenuation and its relationship to  $L_g$  attenuation are required before much reliance can be placed on such correction procedures.

To improve physical understanding of the  $L_g/P_g$  measurements as a function of frequency and their dependence on source and propagation effects, we have used the observed behavior of  $L_g/P_g$  ratios to constrain theoretical models. We examined synthetic  $L_g/P_g$  ratios for 1-D layered continental crustal models and sought to answer the question whether the gross features of  $L_g/P_g$  ratios for shallow explosions and deeper (mid-crustal) earthquakes could be explained with layered crustal models and frequency-dependent intrinsic attenuation. We chose a set of models representative of the diverse range of continental crusts (including thick and thin crusts, thick and thin sedimentary layers, and high and low moho velocities). We then examined several Q models for these crusts (including both frequency and depth dependence of intrinsic attenuation,  $Q(f,z)$ ), and we settled on a relationship that satisfies observed gross features of  $L_g/P$  ratios. Green's functions were computed at several distances for each model with shallow and mid-crustal sources; and the dependence of synthetic regional P and  $L_g$  amplitudes as a function of frequency and distance were examined, as well as the corresponding  $L_g/P$  ratios. It is a common paradigm for regional calibration that the observed attenuation of

regional P and  $L_g$  waves from earthquakes can be used to predict similar behavior for explosions. This calibration strategy assumes that the only differences between regional explosion and earthquake signals are imparted by differences in excitation by the sources. These differences can be associated with both the seismic mechanism and the source depth. The synthetic Green's functions contain both the source excitation (including mechanism and depth effects) and the propagation effects of the crustal waveguide. If layered earth synthetics are representative of "average" regional propagation, then these exercises should provide insight into the ability to discriminate earthquakes and explosions using  $L_g/P_g$  ratio measurements in diverse crustal structures.

In a separate study under this contract, we performed a discrimination analysis on an event which occurred in the Kara Sea southeast of the former Russian test site at Novaya Zemlya on August 16, 1997. Although  $L_g/P$  ratios could not be used to investigate this event because of the weak  $L_g$  signals, we did analyze S/P ratios determined from band-pass filter analyses similar to those which we used for  $L_g/P$  ratios. We compared the S/P ratios for several events in the vicinity of Novaya Zemlya observed at common stations and found that the ratio measurements for the 1997 Kara Sea event appeared to be consistent with behavior seen in prior earthquakes and different from that seen in explosions from Novaya Zemlya and elsewhere.

### **1.3 Report Organization**

This report is divided into six sections including these introductory remarks. Section 2 describes the event database which we have been working with. Section 3 discusses the results of the empirical studies including comparisons of the measurement algorithms and corrections of the  $L_g/P_g$  ratio measurements based on prior knowledge of regional attenuation. Section 4 describes the modeling studies which have been performed, focusing on investigations of the physical mechanism and efficiency of generation of  $L_g$  signals by explosion and other types of seismic sources. Section 5 describes the discrimination analysis of the August 16, 1996 Kara Sea event. Section 6 summarizes the results of this research and offers some recommendations for further study.

## **2. Database for Regional Discrimination**

### **2.1 Limitations on Regional Data for Discrimination Studies**

The available seismic data are not well-suited for testing the reliability of regional discrimination techniques for use in CTBT monitoring. In particular, the database is limited geographically because of the locations of past nuclear explosion tests and the pattern of natural seismicity and other source types; it is also incomplete because many modern seismic stations, which are key to treaty monitoring, have a very limited experience history which may or may not include nuclear explosions recordings and probably does not include observations at regional distances from nuclear explosions and earthquakes for most stations. In our prior report under this contract, we reviewed the characteristics of a large database which has been developed over the years for use in testing potential regional seismic discrimination techniques. We believe that this database coupled with improved theoretical understanding of regional phase behavior and its relationship to the source can provide the basis for forming reliable regional discrimination techniques.

The existing empirical database is valuable because it includes regional seismic recordings from underground nuclear explosions in several different source areas as well as other source types (viz. earthquakes, chemical blasts, and induced events) at comparable epicentral distances and similar propagation conditions. We have noted that the data for the U.S. tend to include more events at nearer regional distances (i.e. less than 1000 km) and that the event magnitudes for these U.S. events are often smaller in order to enable a more direct comparison between the explosions and small earthquakes for the region around NTS. In contrast, many of the Eurasian explosions in the database were only recorded at a limited number of more distant, far-regional stations (i.e. beyond 1000 km); the event magnitudes tend to be larger; and the alternative source types used for comparison tend to have locations removed from the explosion test areas. Therefore, we often encounter differences between nuclear explosions and other source types with respect to source size and propagation conditions when attempting to demonstrate the validity of regional discriminant measures and to identify their dependence on source

characteristics. It should be noted that magnitude differences and station response are probably less critical for the  $L_g/P$  ratio discriminant considered here than for some other regional discriminants like regional phase spectral ratios, but propagation differences may be very important.

## 2.2 Data Used for These Studies

The objective in the empirical element of the present study has been to determine specific procedures for use in measuring  $L_g/P$  amplitude ratios as a function of frequency and to determine how those ratios are likely to be affected by propagation path properties. To accomplish this objective we have compared alternative spectral estimation techniques applied to the  $L_g$  and regional  $P$  signals for selected events from the western U.S. and Eurasia. We have also developed and applied propagation path corrections to the  $L_g/P_g$  measurements from several events and analyzed how the corrections affected the  $L_g/P_g$  ratios as a function of frequency.

Figures 1 and 2 show the locations of stations and events in the U.S. and Eurasia respectively for which the records were collected and reviewed for use in evaluating the  $L_g/P$  ratio measurement techniques and determining effects of propagation path on the measurements during this phase of the study. The western U.S. data tend to be dominated by the near-regional observations of NTS explosions and nearby earthquakes recorded by the Lawrence Livermore National Laboratory (LLNL) seismic network, as noted above, although we also supplemented the database with other nuclear explosions, earthquakes, and chemical explosions recorded at additional regional stations in the western U.S., including some at farther regional distances. However, it should be noted that signal-to-noise level at many of the distant stations is reduced particularly at high frequencies; so that such measurements may not always be useful.

The Eurasian data used in these studies (cf. Figure 2) included nuclear explosions from eastern Kazakhstan in the former Soviet Union, Lop Nor in China, and Novaya Zemlya in northern Russia. We also reviewed the observations from earthquakes in Eurasia at comparable regional distances to the nuclear explosions. As noted above, the seismic stations available for Eurasian nuclear explosions were often at far-regional

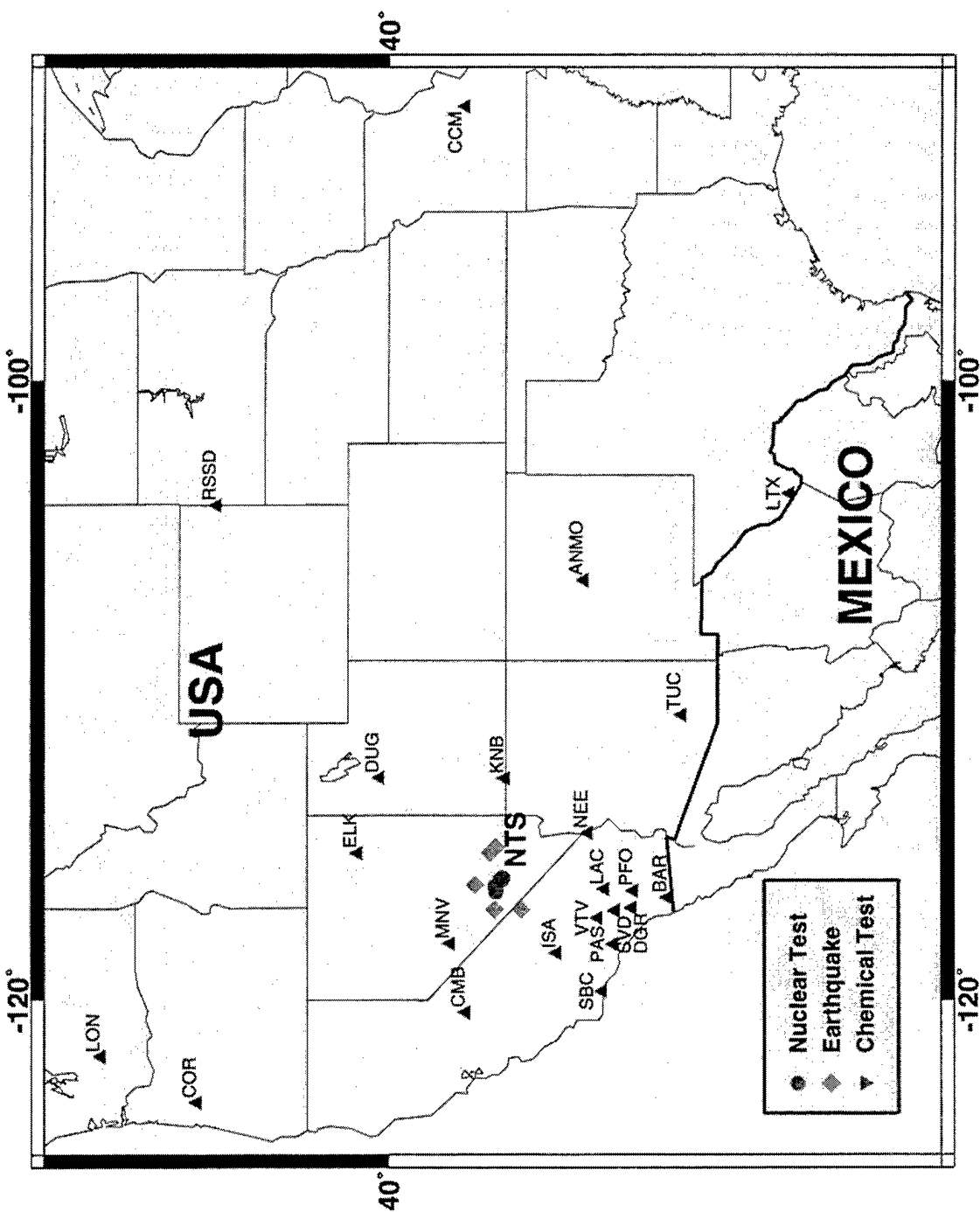


Figure 1. Locations of selected explosions, earthquakes, and stations used in analyzing regional signals from western U. S. events.

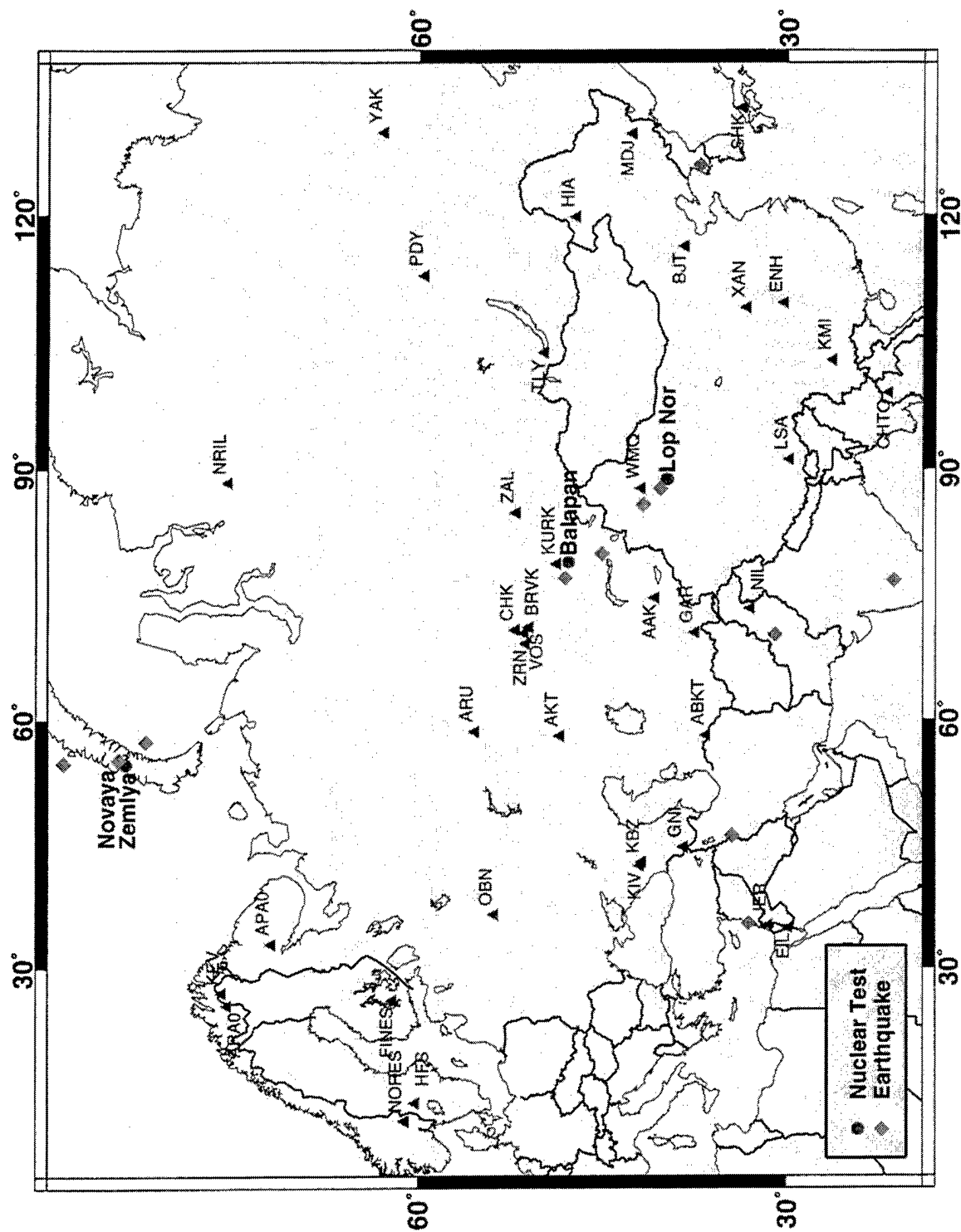


Figure 2. Locations of selected explosions, earthquakes, and stations used in analyzing regional signals from Eurasian events.

distances and beyond; this tends to limit the frequency band over which  $L_g/P$  ratios can be reliably measured. Furthermore, along some paths  $L_g$  signals are totally blocked and cannot be measured at stations which would normally be in the regional distance range. This is in particular true for events in the vicinity of Novaya Zemlya, which provide a challenge to traditional regional discrimination methods, as described in Section 5 below, although seismic stations often record regional S signals from that source area which appear to provide diagnostic capability.

### **3. Analyses of the Observed Behavior of $L_g/P$ Ratios**

#### **3.1 Background**

The  $L_g/P$  ratio has long been regarded as one of the most reliable regional discriminants (cf. Blandford, 1981; Pomeroy et al., 1982). Some of the first observations of the use of  $L_g/P$  ratios for discriminating explosions from earthquakes were made by Willis (1963) and Willis et al. (1963), who found that nearly 80 percent of earthquakes had larger  $L_g/P$  ratios than explosions. However, over the years conflicting evidence has been raised (cf. Pomeroy, 1977; Pomeroy and Nowak, 1979; Murphy and Bennett, 1982) about the reliability of simple  $L_g/P$  ratios derived from time-domain peak amplitude measurements to distinguish between explosions and earthquakes. Taylor et al. (1989) found significant separation in  $L_g/P_g$  ratios for western U.S. earthquakes and NTS nuclear explosions recorded by the LLNL seismic network. Blandford (19981) discovered that adjusting  $L_g/P$  ratio measurements for propagation effects, derived from empirical studies, improved the separation in the discriminant for different source types. Bennett et al. (1989) found that  $L_g/P$  ratios for western U.S. events were effective in certain frequency bands but not in others, which possibly explained some of the conflicting evidence found in some of the prior studies.

Bennett et al. (1989, 1992) found that  $L_g/P$  ratios for Eurasian events, including nuclear explosions in eastern Kazakhstan, at Lop Nor in China, and at Novaya Zemlya in Russia, and earthquakes at similar distance ranges (i.e. mainly far-regional), were frequency dependent. They showed that the ratios for different event types were mixed

at frequencies of 1 Hz and below, but that they tended to separate at higher frequencies; they also found station-dependent variations in the measurements between events which suggested propagation effects. Baumgardt and Young (1990) and Dysart and Pulli (1990) also looked at the  $L_g/P$  ratios from small events in northern Europe recorded at nearer regional stations and found that earthquakes generally produced higher ratios than mineblasts with the differences again being emphasized at higher frequencies.

Based on this experience, regional measurements of  $L_g/P$  ratios appear to offer some potential for discriminating underground nuclear explosion tests from earthquakes and other source types. However, there are a number of outstanding issues which must be addressed before  $L_g/P$  ratios can be considered to provide a reliable discrimination technique. Probably the most important step in establishing the reliability of any regional discriminant is to determine a physical understanding of how the discriminant behaves and what features of the source and propagation path it may be sensitive to. The goal of the current research has been to improve theoretical understanding of the  $L_g/P$  ratio and its dependence on the source. To lay the basis for such theoretical understanding, we have sought to identify the characteristics of  $L_g/P$  ratio behavior and its dependence on frequency using consistent procedures to determine regional phase signal spectra for events in different regions.

### **3.2 Processing Scheme for $L_g/P$ Ratio Measurements**

In a prior report under this contract (cf. Bennett et al., 1997a), we used a common band-pass filter analysis procedure to determine  $L_g/P$  ratios as a function of frequency for samples of nuclear explosions, earthquakes, rockbursts, and mine explosions from a variety of different tectonic regions including the western U.S. and Eurasia. Figures 3a and 3b show the average  $L_g/P$  amplitude ratios for nuclear explosions and earthquakes respectively, as determined by Bennett et al. (1997a). The  $L_g/P$  ratios have their highest values at low frequencies and decline toward higher frequencies. At 1 Hz and below, the  $L_g/P$  ratios are above one for explosions and earthquakes; and the ratios show little distinction with respect to source type. However, above 2 Hz the explosion  $L_g/P$  ratios drop off more rapidly and fall to well below one while the earthquake ratios remain at or

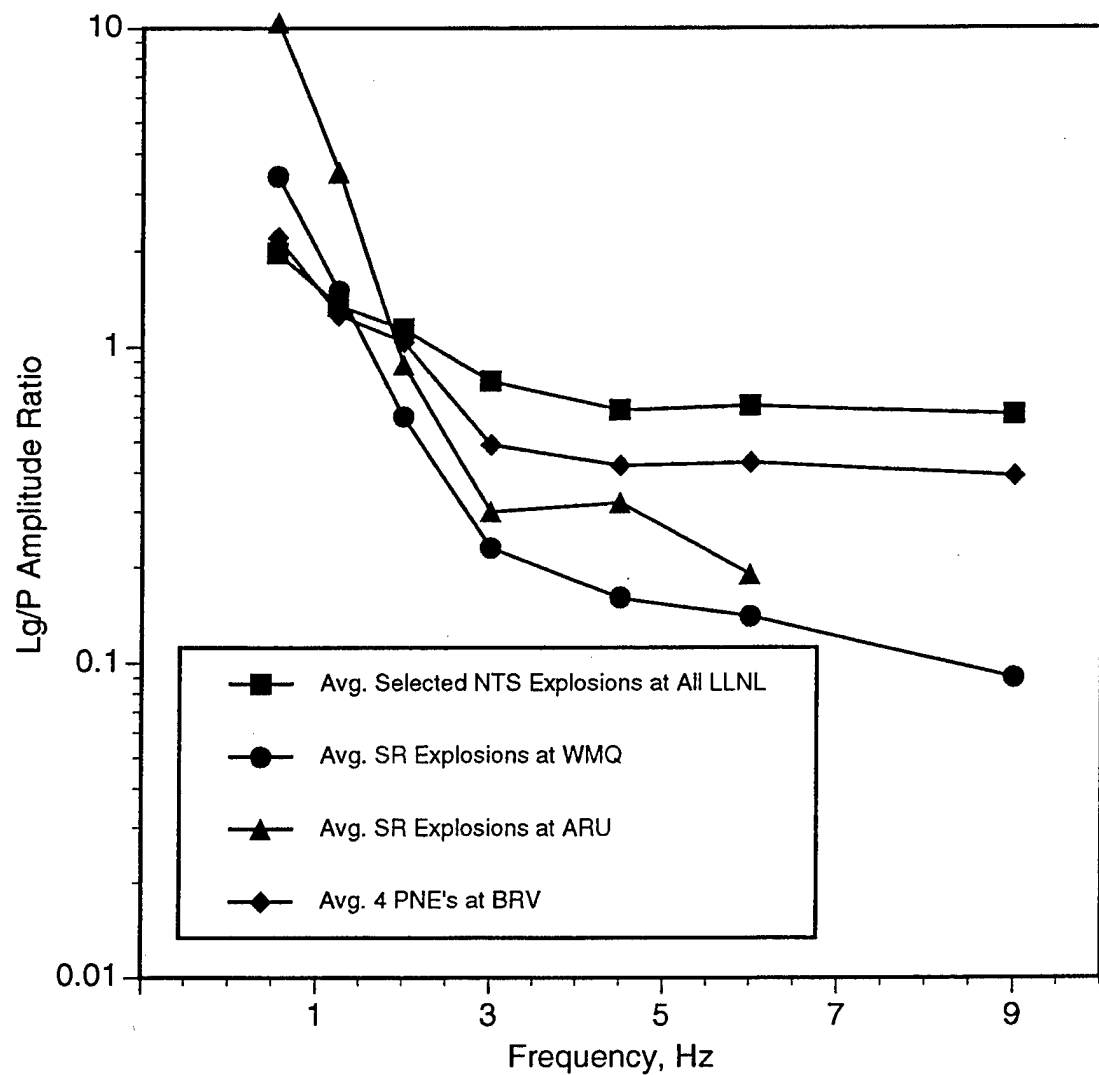


Figure 3a. Average Lg/P ratios as a function of filter center frequency determined from traditional broad band-pass filter analysis for nuclear explosions in the western U.S. and Eurasia (adapted from Bennett et al., 1997).

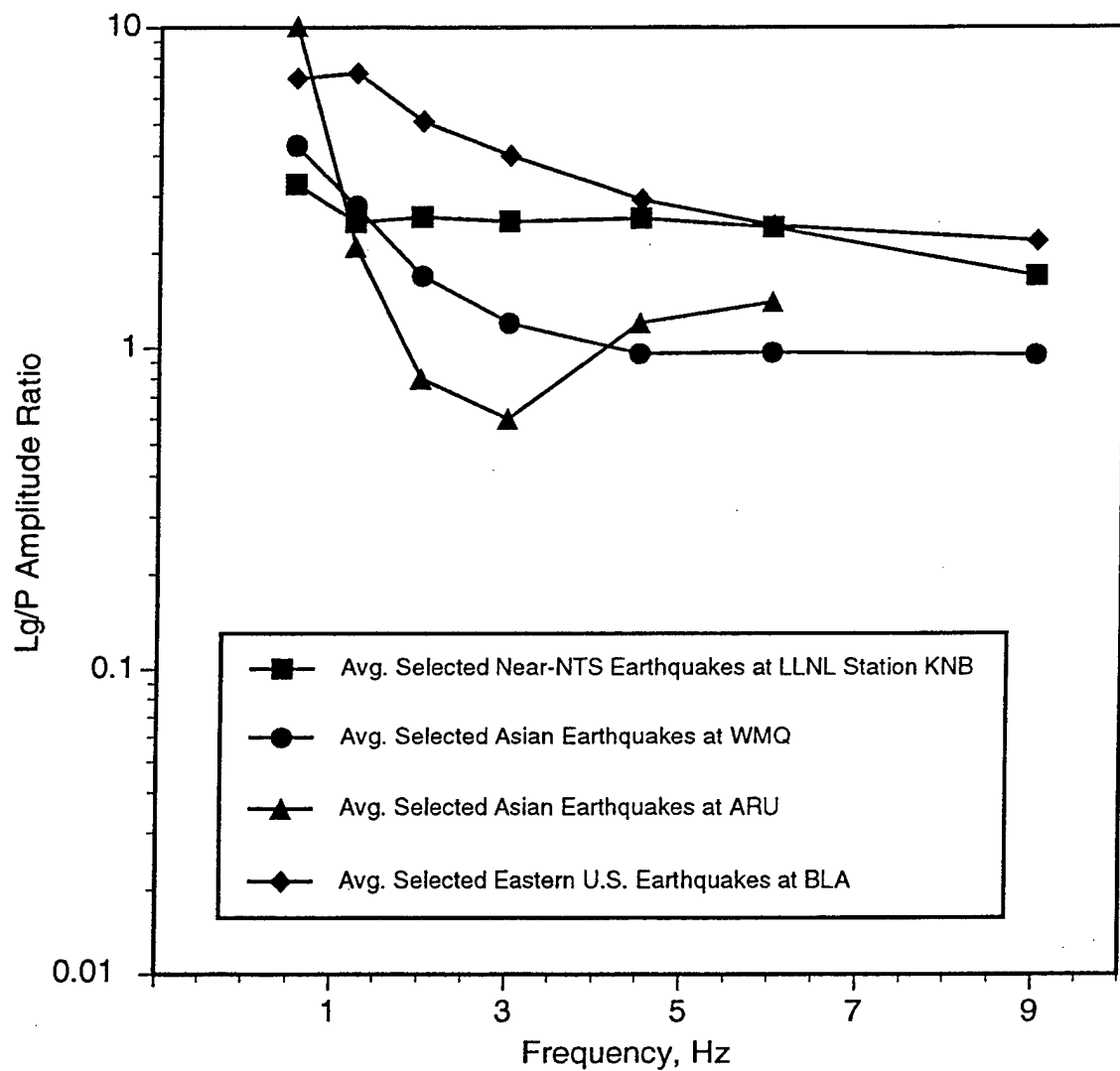


Figure 3b. Average Lg/P ratios as a function of filter center frequency determined from traditional broad band-pass filter analysis for earthquakes in the U.S. and Eurasia (adapted from Bennett et al., 1997).

above one at higher frequencies. As can be seen in Figures 3a and 3b, there remain significant differences in the  $L_g/P$  ratios. Some of the differences are probably related to propagation path effects caused by differences in the source-station distance and in propagation efficiency associated with regional geologic properties in the different regions where the measurements were obtained. In Section 3.3 below, we investigate how regional attenuation is expected to affect frequency-dependent  $L_g/P_g$  amplitude ratios. In this section we focus on a comparison of the processing scheme used to generate the measurements in Figures 3a and 3b with several alternative procedures to obtain the spectral estimations for the  $L_g/P$  ratios.

The band-pass filters used in many of our previous studies (cf. Bennett et al., 1992, 1995) and those used to develop the measurements in Figures 3a and 3b were fairly broad; the high-frequency corner was usually selected to be twice the low-frequency corner at most frequencies, and beyond the corner frequencies the filter response fell off at 60 dB per octave. The filter spacing was selected so that there was considerable overlap in the passbands between adjacent measurements. Since this technique differs from more established techniques of spectral analysis (e.g. Fourier transform), we ran several test cases to compare alternative methods for spectral analyses of regional phase signals and, in particular, their effect on  $L_g/P_g$  ratio measurements. The first two spectral estimation methods involved variations in the amplitude measure for the overlapping broad band-pass filters, as described above. In both of these processes, we used eight filter passbands: 0.5 - 1.0 Hz, 0.75 - 1.5 Hz, 1.0 - 2.0 Hz, 1.5 - 3.0 Hz, 2.0 - 4.0 Hz, 3.0 - 6.0 Hz, 4.5 - 9.0 Hz, and 6.0 - 12.0 Hz. In one case, we followed the approach of prior investigations and simply picked the maximum amplitude of the filter output in the appropriate group velocity window (viz. 3.6 - 3.0 km/sec for  $L_g$  and 6.1 - 5.0 km/sec for  $P_g$ ) to obtain the spectral estimates to form the  $L_g/P_g$  ratios. In the alternative method, we computed a RMS average of the amplitudes over the same group velocity windows for each of the filter outputs and used that to determine the spectral estimates and the  $L_g/P_g$  ratios. Figure 4 shows a comparison of the results of applying these two approaches to obtain the  $L_g/P_g$  ratios as a function of frequency (i.e. filter center frequency) for five NTS nuclear explosions recorded at station KNB ( $R \approx 290$  km). The two procedures are

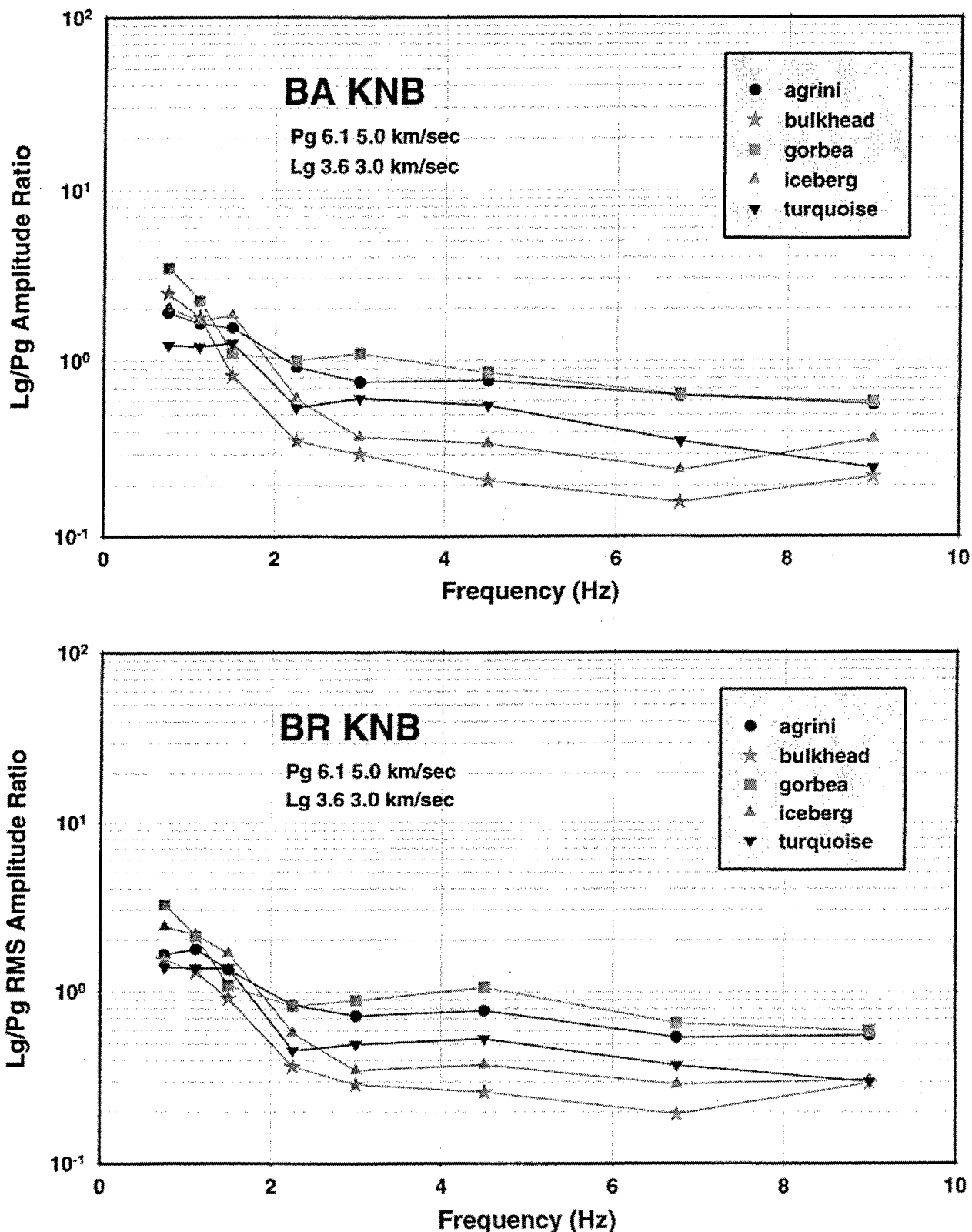


Figure 4. Comparison of  $L_g/P_g$  ratios as a function of frequency from peak amplitude (top) and RMS amplitude (bottom) measurements derived using broad bandpass filters for NTS explosions recorded at LLNL station KNB.

seen to produce very similar results. The  $L_g/P_g$  ratios for the NTS explosions are generally greater than one at frequencies below about 2 Hz, but fall to below one at higher frequencies. Although we see some differences in the spectral measurements between events, these differences are minor. We have found this to be true also for similar measurements for other regional events in the database and for the individual regional phases as well (cf. Bennett et al., 1997b); spectral estimates based on peak amplitude measurements were nearly identical to those based on RMS average amplitudes.

In our prior report on this contract (cf. Bennett et al., 1997a) and in related studies (cf. Murphy et al., 1996), we briefly described a band-pass filtering scheme which used Gaussian filters to determine the spectra from regional phase signals. These Gaussian filters have much narrower passbands than the filters described above; the Gaussian filters used in our studies had quality factors equal to six times the center frequencies for each band. In our processing we used a suite of filters with center frequencies uniformly spread at intervals of 0.25 Hz over the band from 0.25 Hz to 10 Hz. The spectral estimates were obtained from a RMS average of the amplitudes from the filter output over the regional phase window. For  $P_g$  the window covered a group velocity range from 6.1 to 5.0 km/sec and for  $L_g$  from 3.6 to 3.0 km/sec. The top of Figure 5 shows the  $L_g/P_g$  ratios determined from the Gaussian filter analyses for the same NTS explosions recorded at KNB, as in Figure 4. Comparing between Figure 5 (top) and Figure 4, there appears to be little difference in the general trends of the  $L_g/P_g$  ratios determined by the different methods; however, the  $L_g/P_g$  ratios from the Gaussian filters seem to have much more detail while the ratios from the broad filter tend to smooth over the differences. Bennett et al. (1997b) noted that the broad filters used to determine regional phase spectral ratios tended to not only smooth the spectra but also inflate the values at higher frequencies. The latter does not seem to hold for the  $L_g/P_g$  ratios, presumably because  $L_g$  and  $P_g$ , determined from the broad filters, experience similar spectral leaking which is eliminated when the ratios are formed.

For comparison we have plotted at the bottom of Figure 5 the  $L_g/P_g$  ratios determined from the same five NTS explosions using Fourier analyses to compute the

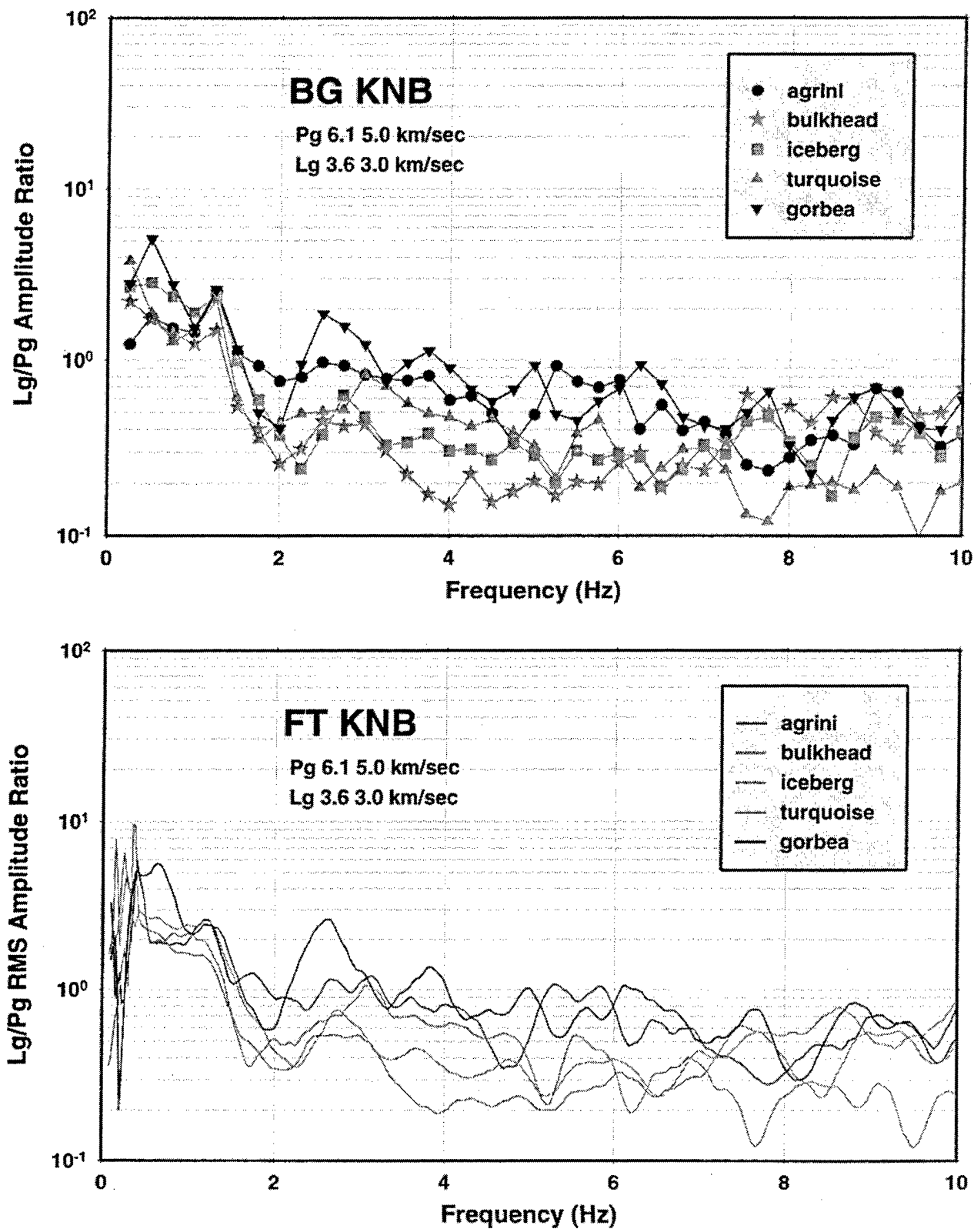


Figure 5. Comparison of  $L_g/P_g$  ratios as a function of frequency using narrow bandpass Gaussian filters (top) and Fourier analyses (bottom) for NTS explosions recorded at LLNL stations KNB.

spectra for the  $P_g$  and  $L_g$  windows before taking the ratios. These Fourier spectra have been smoothed using a running average to achieve approximately the same resolution as for the Gaussian filters. Comparison of the top and bottom plots in Figure 5 indicates that the  $L_g/P_g$  ratios determined using the Gaussian filters closely match the ratios determined from Fourier analyses at all frequencies. We have tested this procedure on several additional record samples from the database and found similar results. The Fourier analyses procedures are generally faster than the Gaussian filters for estimating spectra, but we believe that the Gaussian filters offer some operational advantages for real-time processing, because they do not require prior knowledge to set the window for the regional phase spectral estimates.

We would conclude from the kinds of comparisons shown here in Figures 4 and 5 that the specific method used to estimate the regional phase amplitudes as a function of frequency is not, in general, critical to the  $L_g/P_g$  ratio measurements. The different band-pass filtering methods which we have applied here produced about the same results as Fourier analyses when used to compute  $L_g/P_g$  ratios as a function of frequency. The main differences between the methods appears to be in the frequency resolution, as the broader filters tend to smooth over a range of frequencies. However, for the  $L_g/P_g$  ratios the broader filters produce approximately the same overall trend and level as the narrower filters.

### **3.3 Correction of $L_g/P_g$ Ratios for Path Attenuation**

#### **3.3.1 Model for Attenuation Corrections**

The behavior of the  $L_g/P_g$  discriminant as a function of frequency is critically dependent on properties of the propagation path between the source and the observing seismic station. In particular,  $L_g$  and  $P_g$  signal measurements at regional distances are affected by attenuation and geometrical spreading characteristic of the propagation path. In this section we analyze how these factors affect the regional phase signals and the corresponding  $L_g/P_g$  ratios and describe correction factors, based on prior knowledge of regional attenuation, which may be useful in eliminating path effects from the observations.

The observed regional phase spectrum from a seismic source can be represented as the result of a linear process in which the seismic source spectrum is modified by 1) the site response of the earth's crust in the vicinity of the source, 2) transmission effects along the propagation path between the source and receiver, 3) the site response of the earth's crust in the vicinity of the seismic station, and 4) the response of the recording instrument. In analyzing  $L_g/P_g$  ratios as a function of frequency, the response of the recording instrument can be considered the same for  $L_g$  and  $P_g$  signals; and the recording response factor can be eliminated. Although crustal responses at the source and receiver may affect the  $L_g/P_g$  ratios, we are not considering those factors here but are focusing on the propagation path effects alone. We can thus represent the observed regional phase spectrum  $A(f,r)$  from the seismic source as

$$A(f,r) = S(f) \cdot G(r, r_0) \cdot e^{-\pi f/Q(f)} \quad (1)$$

where  $S(f)$  = the spectrum of the seismic source (and including other site factors noted above)

$f$  = frequency

$r$  = distance

$r_0$  = the reference distance

$t$  = travel time

$G(r, r_0)$  = the geometrical spreading term and

$Q(f)$  = the frequency-dependent quality factor describing attenuation.

The frequency-dependent  $Q(f)$  is represented by

$$Q(f) = Q_0 \cdot f^\eta \quad (2)$$

where  $Q_0$  = attenuation at 1 Hz and

$\eta$  = the frequency dependence of  $Q$ .

The earth is not homogeneous, and it is assumed that  $Q_0$  and  $\eta$  vary with location and depth. However, because the  $L_g$  and  $P_g$  phases are confined to a waveguide, we make the simplifying assumption that the average  $Q_0$  and  $\eta$  of the crustal waveguide for each of these phases are representative of the effective attenuation and ignore the depth dependence. Thus, we assume that the  $Q$  model consists of point samples (i.e. a grid)

representing the distribution of the  $Q_0$  and  $\eta$  over the earth's crust. The gridded models can be used to calculate the effects of attenuation on the  $L_g$  and  $P_g$  signals for specific paths. This is done by tracing the source-to-receiver path through the grid of  $Q$  values and summing the attenuation contributions from each cell. Thus, for an individual phase and frequency the attenuation factor is

$$\Gamma(f) = e^{-\pi f \sum_{i=1}^n t_i^*} \quad (3)$$

where

$$\sum_{i=1}^n t_i^* = \frac{t_1}{Q_1} + \frac{t_2}{Q_2} + \dots + \frac{t_n}{Q_n} \quad (4)$$

The  $t_i$  in Eq. 4 are the travel times spent in the individual grid cells along the path, and the  $Q$  values as a function of frequency are given by Eq. 2 for each cell. For geometrical spreading, we assume spherical spreading for distances less than or equal to the reference distance,  $r_0$ , after which spreading is assumed to be cylindrical (e.g. Sereno et al., 1987):

$$G(r, r_0) = \frac{1}{r} \quad \text{for } r \geq r_0 \quad (5)$$

$$G(r, r_0) = \frac{1}{r_0} \cdot \left( \frac{r_0}{r} \right)^{0.5} \quad \text{for } r < r_0 \quad (6)$$

The  $r_0$  used throughout this study is taken to be roughly twice the average thickness of the crust, or about 100 km. Corrections to the  $L_g/P_g$  ratio as a function of frequency along any path through the attenuation model can be estimated using this procedure.

Routine application of the attenuation path corrections to observed  $L_g/P_g$  ratios from events that might be at any location require a model that includes all continental crustal paths where  $L_g$  and  $P_g$  may propagate. Gridded  $L_g$  coda  $Q$  models have been developed for Africa, Eurasia, and the U.S. by Mitchell and his colleagues (cf. Xie and Mitchell, 1990; Mitchell et al., 1996; Mitchell, 1997) using a back projection algorithm that produces a tomographic image of  $Q(L_g)$  through inversion of  $L_g$  coda amplitude measurements. This model includes attenuation from both intrinsic and scattering mechanisms and, thus, represents an effective  $Q$ . The African and Eurasian models were

represented by 3°-by-3° grid cells of fixed  $Q_0$  and  $\eta$ , while the U.S. model had somewhat smaller grid spacing with 2°-by-2° cells. Figures 6 and 7 show composites of the models for  $Q_0$  and  $\eta$  respectively covering all three regions. It should be noted that the  $\eta$  model for Eurasia has been modified somewhat from that originally produced by Mitchell et al., but the modifications do not greatly affect the corrections. The maps are generally consistent with the observed behavior of  $L_g$  with relatively high  $Q$  in shield and stable platform regions where the attenuation is low and relatively low  $Q$  in more active and structurally complex regions where the attenuation is high. We used these models to calculate the attenuation corrections for the  $L_g$  spectral measurements, as described above.

Corresponding attenuation models for the  $P_g$  phase do not currently exist, and so we decided to estimate the behavior for  $P_g$  based on theoretical considerations and using some simple assumptions for the relationship to  $L_g$  propagation. The  $P_g$  phase has roughly the same path as the  $L_g$  phase, both are assumed to propagate in the same crustal waveguide. So, it is not unreasonable to assume that  $Q(P_g)$  should be related to  $Q(L_g)$ . If the crust were a Poisson solid (i.e. all loss is related to shear), the  $Q(P_g)$  would be equal to 2.25  $Q(L_g)$ . However, synthetic seismograms computed as part of this study, as described in Section 4, suggest that  $Q(P_g)$  approximately equal to  $Q(L_g)$  often seems to provide predictions which are more consistent with observed behavior of the  $L_g/P_g$  ratios. As scattering increases at high frequencies, the ratio of  $Q(P_g)$  to  $Q(L_g)$  would be expected to decrease (cf. Taylor et al., 1986). A reasonable approach then might be to assume a large value of the ratio at low frequencies where scattering is minimal and a lower value of the ratio at high frequencies where more crustal scattering is expected. The final development of such a relationship is beyond the scope of the work presented here. However, we have attempted to explore some of the expected effects of the potential range in the relationship between  $Q(P_g)$  and  $Q(L_g)$  and how that would affect the attenuation corrections to the  $L_g/P_g$  ratios.

If the attenuation model described here is to be proven reliable for correcting  $L_g/P_g$  amplitude ratio measurements on a routine basis, several outstanding issues must be resolved. The  $L_g$  attenuation model needs to be validated with additional observations

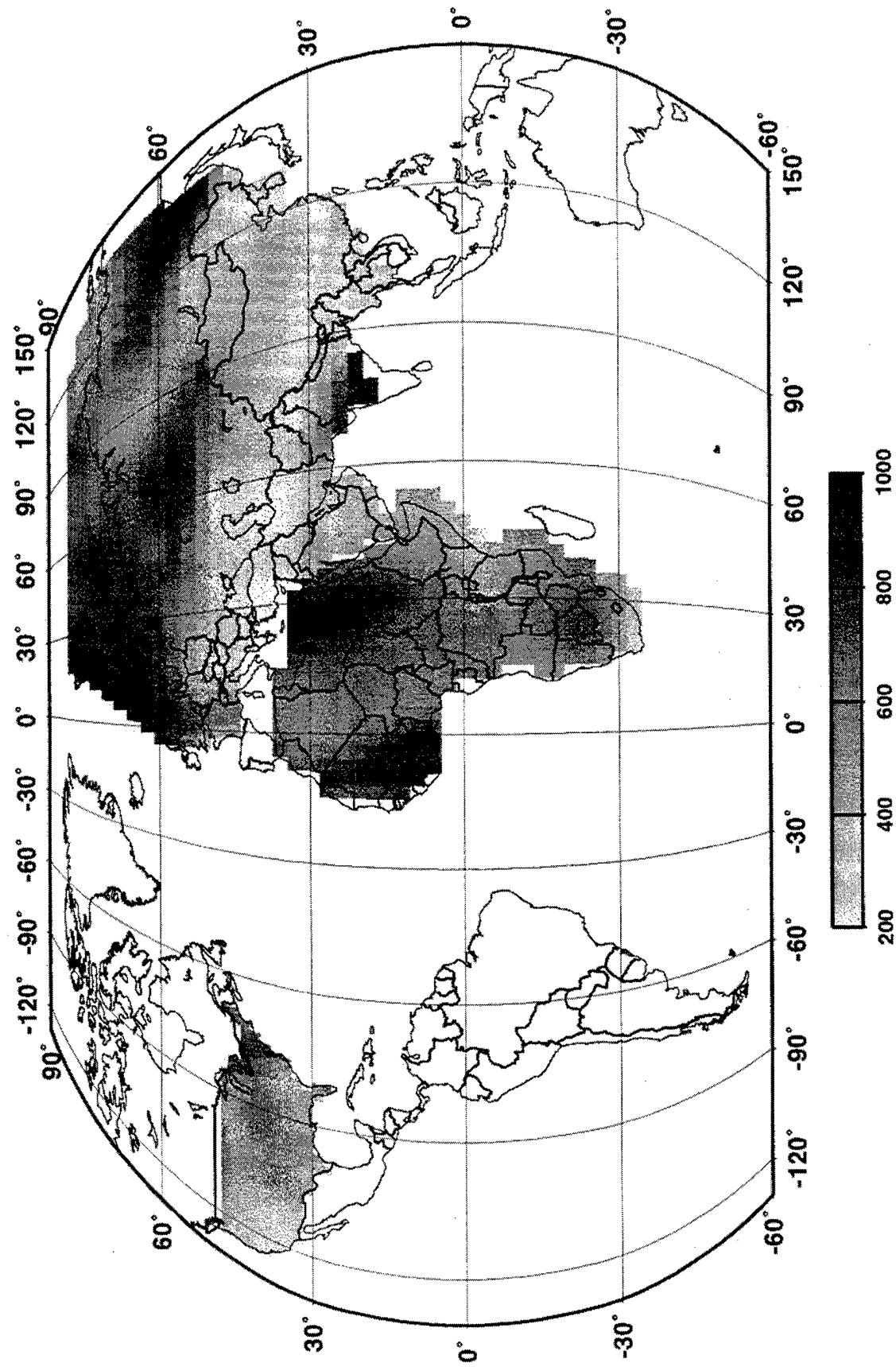


Figure 6. Attenuation at 1 Hz ( $Q_0$ ) from  $Lg$  Coda adapted from coda-Q studies of Mitchell et al. (cf. Xie and Mitchell, 1990, Mitchell et al., 1996)

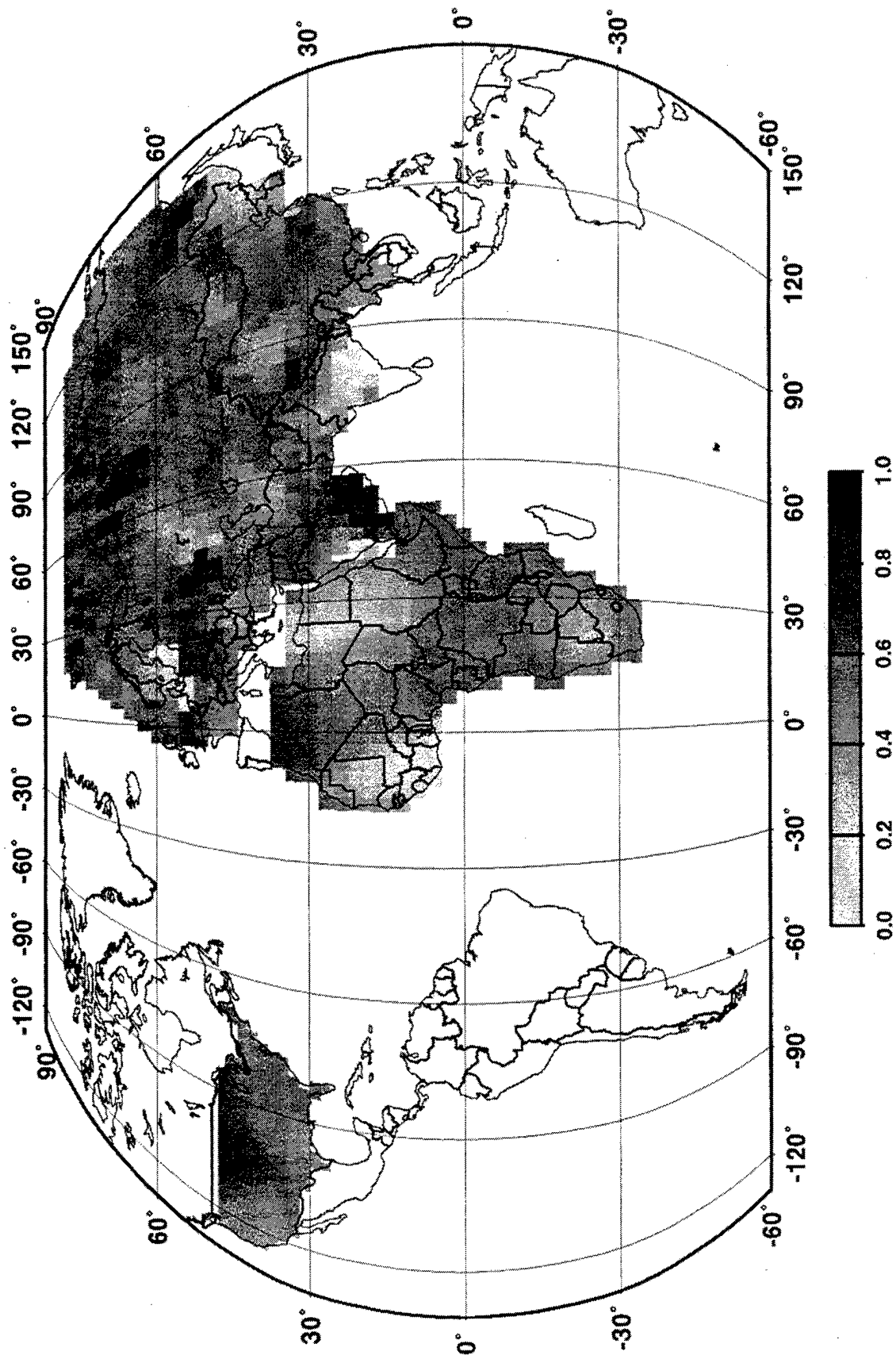


Figure 7. Frequency dependence of attenuation ( $\eta$ ) from  $L_g$  coda adapted from work by Mitchell et al. (cf. Xie and Mitchell, 1990, Mitchell et al., 1996)

from  $L_g$  signals in various areas, and a corresponding model for  $P_g$  attenuation needs to be derived and similarly validated. Rather than undertake this large task in the short time allotted for this study, we have assumed that the attenuation model for  $L_g$  is accurate (it was derived from independent studies as noted above); and then we have explored the range in the corrections to the  $L_g/P_g$  ratios that would be applied under different assumptions about the relationship between the  $L_g$  and  $P_g$  attenuation models.

To obtain a feeling for the relative size and importance of the  $L_g/P_g$  corrections, we can generate maps of the  $L_g/P_g$  attenuation corrections derived from the models described above for selected frequencies. Such maps can be developed either for the region surrounding a regional seismic station or (using the principle of reciprocity) for the region surrounding a source. The station maps would represent the corrections that would be applied to the  $L_g/P_g$  observations at that station for events in the surrounding region; and source maps would give the attenuation corrections to the  $L_g/P_g$  observations from a particular event at stations in the region around that source. For this study we have focused on events located at NTS and Lop Nor as recorded at stations in the surrounding regions, and we show the maps of the corrections for frequencies of 1 Hz, 2 Hz, 4 Hz, and 8 Hz. These maps are shown in Figures 8 and 9 for the regions surrounding NTS and Lop Nor respectively. In generating these maps we assumed that  $Q(P_g)$  was equal to 1.67  $Q(L_g)$ ; this relational value falls roughly in the middle of the range of likely values for the  $Q(P_g)/Q(L_g)$  ratio. Many subtleties of the attenuation corrections are difficult to discern in the gray-scale map presentations shown. The effects of the lateral variations in the  $Q$  models are generally seen much more for the high-frequency plots than for the low-frequency plots. At 1 Hz the plots of the  $L_g/P_g$  attenuation corrections appear nearly radially symmetric; there appears to be only slightly larger correction factors for paths toward southerly azimuths from the vicinity of Log Nor. At 1 Hz the correction factors are all fairly modest, covering a range from  $10^{-1}$  to about  $10^1$  for the region around NTS and a range from  $10^{-1}$  to about  $10^2$  for the region around Lop Nor, with the corrections increasing outward with distance from the source area. At 2 Hz the correction factors show somewhat greater range, between  $10^{-1}$  and  $10^2$  around NTS and between  $10^{-1}$  and  $10^3$  around Lop Nor, but corrections continue to show

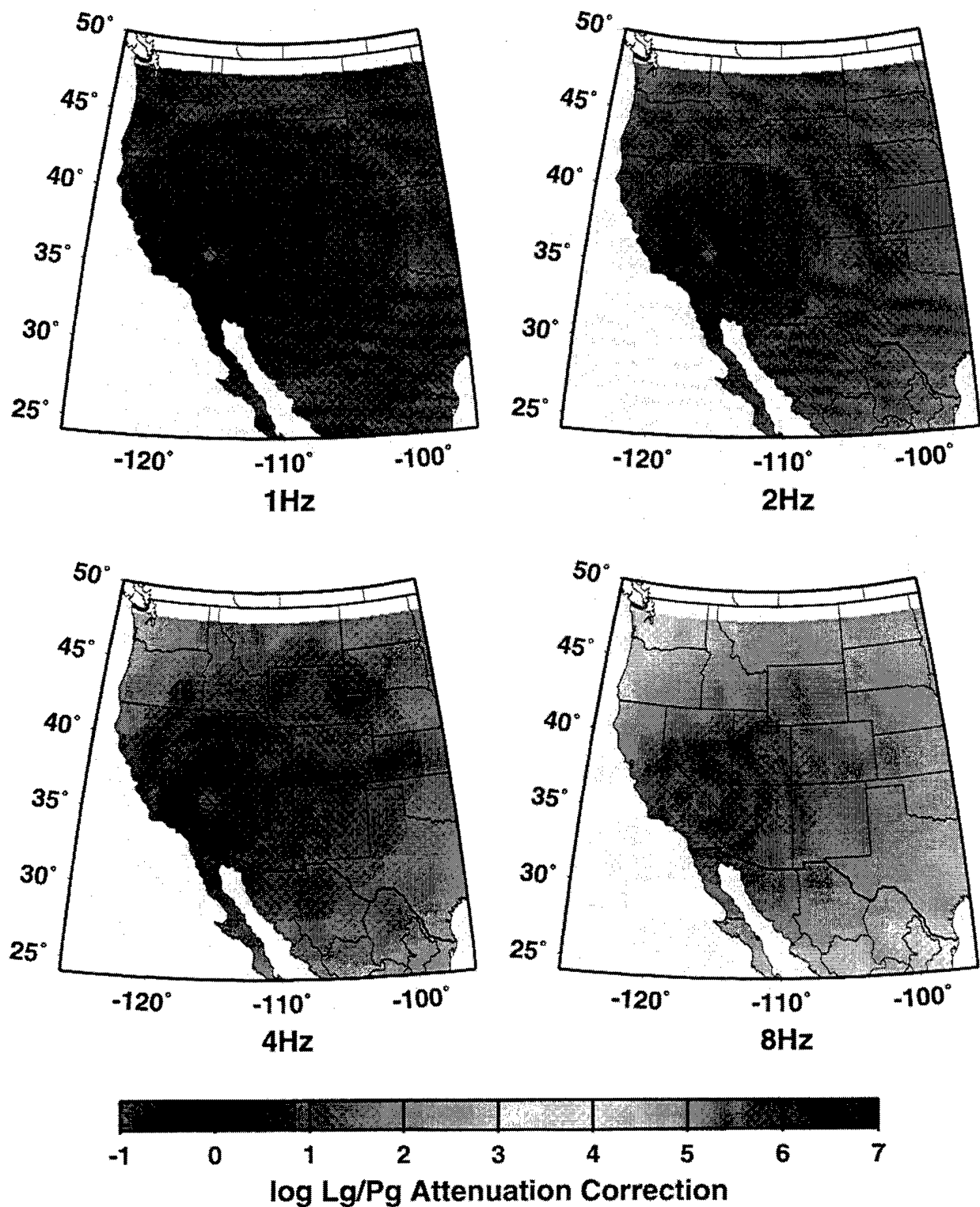


Figure 8. Predicted  $L_g/P_g$  attenuation correction factors in the surrounding region of a source at NTS for four frequencies assuming  $Q_{P_g} = 1.67 Q_{Lg}$ .

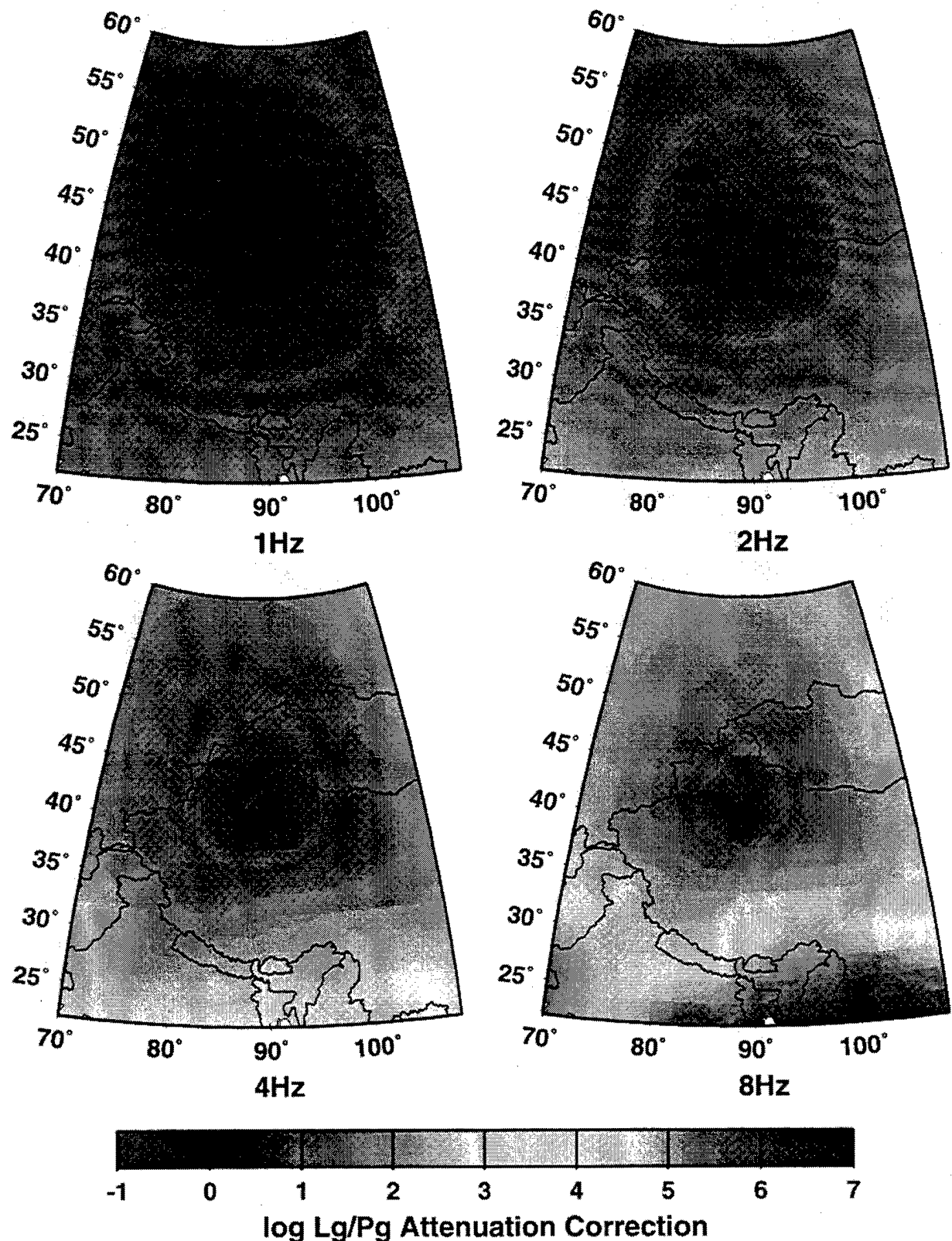


Figure 9. Predicted  $L_g/P_g$  attenuation correction factors in the surrounding region of a source at Lop Nor China for four frequencies assuming  $Q_{P_g} = 1.67 Q_{L_g}$ .

generally a uniform increase outward except for again slightly greater factors at southerly azimuths and at northeasterly azimuths from Lop Nor. The range around NTS at 4 Hz is between  $10^{-1}$  and  $10^{2.5}$  and between  $10^{-1}$  and  $10^{4.5}$  around Lop Nor. At 4 Hz the corrections are somewhat greater at southeasterly and northwesterly azimuths from NTS, and they are greater at southerly and northeasterly azimuths from Lop Nor. Finally, at 8 Hz the  $L_g/P_g$  correction factors range from about  $10^{-1}$  to  $10^4$  around NTS and from  $10^{-1}$  to nearly  $10^7$  around Lop Nor; the correction factors increase more rapidly along southeasterly and northwesterly azimuths from NTS and along southeasterly and northeasterly azimuths from Lop Nor. To the southwest of Lop Nor there appears to be a tongue of less-rapid attenuation followed by a rapid increase in the attenuation factor.

Our studies have also found that the attenuation factors for the  $L_g/P_g$  ratios can be fairly sensitive to the relation between  $Q(P_g)$  and  $Q(L_g)$ , which has been assumed to be a constant multiplicative factor

$$Q(P_g) = B \cdot Q(L_g) \quad (7)$$

With this assumption the ratio of the  $L_g/P_g$  attenuation terms from Eq. (1) above simplifies to

$$\frac{L_g}{P_g} \text{ Ratio} = e^{\left( -\pi f \frac{d}{v_{L_g} Q(f)} + \pi f \frac{d}{v_{P_g} B Q(f)} \right)} \quad (8)$$

where  $d$  is the source-station distance and  $v_{L_g}$  and  $v_{P_g}$  are group velocities corresponding to those regional phases. As  $B$  increases so does the attenuation correction factor (which is simply the inverse of Eq. (8)) for the  $L_g/P_g$  amplitude ratios; the effect should be larger at large distances and at higher frequencies.

The effect of the parameter  $B$  on the  $L_g/P_g$  amplitude ratio correction can be seen by looking at the ratio of the correction terms for two different assumed values of  $B$ :  $B = 2.25$  (Poisson solid) and  $B = 1.0$  (high degree of scattering). We mapped the differences in the  $L_g/P_g$  attenuation correction factors for the regions surrounding NTS and Lop Nor at the same set of frequencies (viz. 1 Hz, 2 Hz, 4 Hz, and 8 Hz). These are shown in Figures 10 and 11 respectively. For the region surrounding NTS, the difference in the attenuation correction factors is between  $10^{-1}$  and  $10^1$  at 1 Hz, between  $10^{-1}$  and  $10^2$  at 2

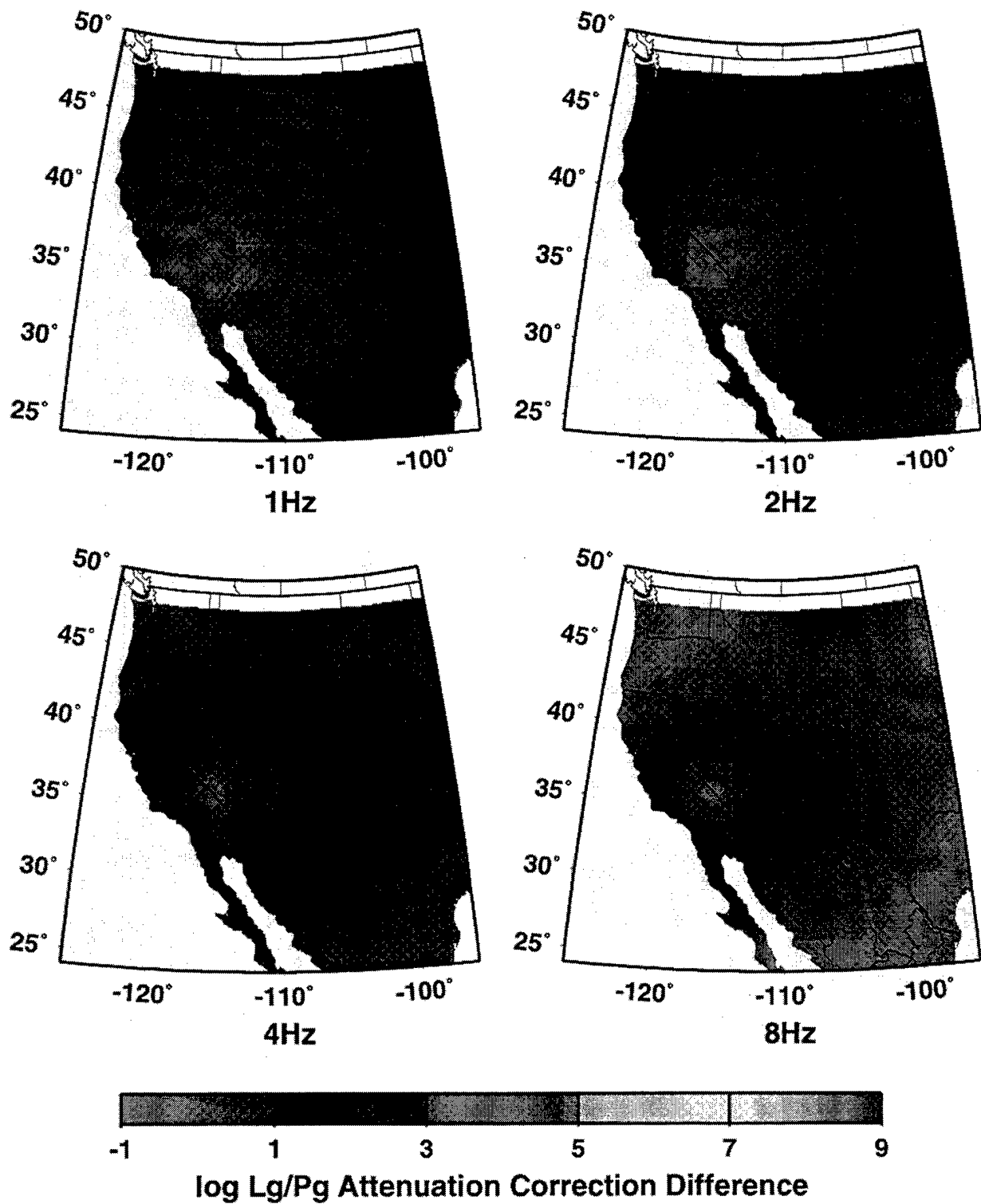


Figure 10. Predicted differences in  $L_g/P_g$  attenuation correction factors in the surrounding region of a source at NTS for four frequencies based on assumptions of  $Q_{Pg}=2.25Q_{Lg}$  and of  $Q_{Pg}=1.0Q_{Lg}$ .

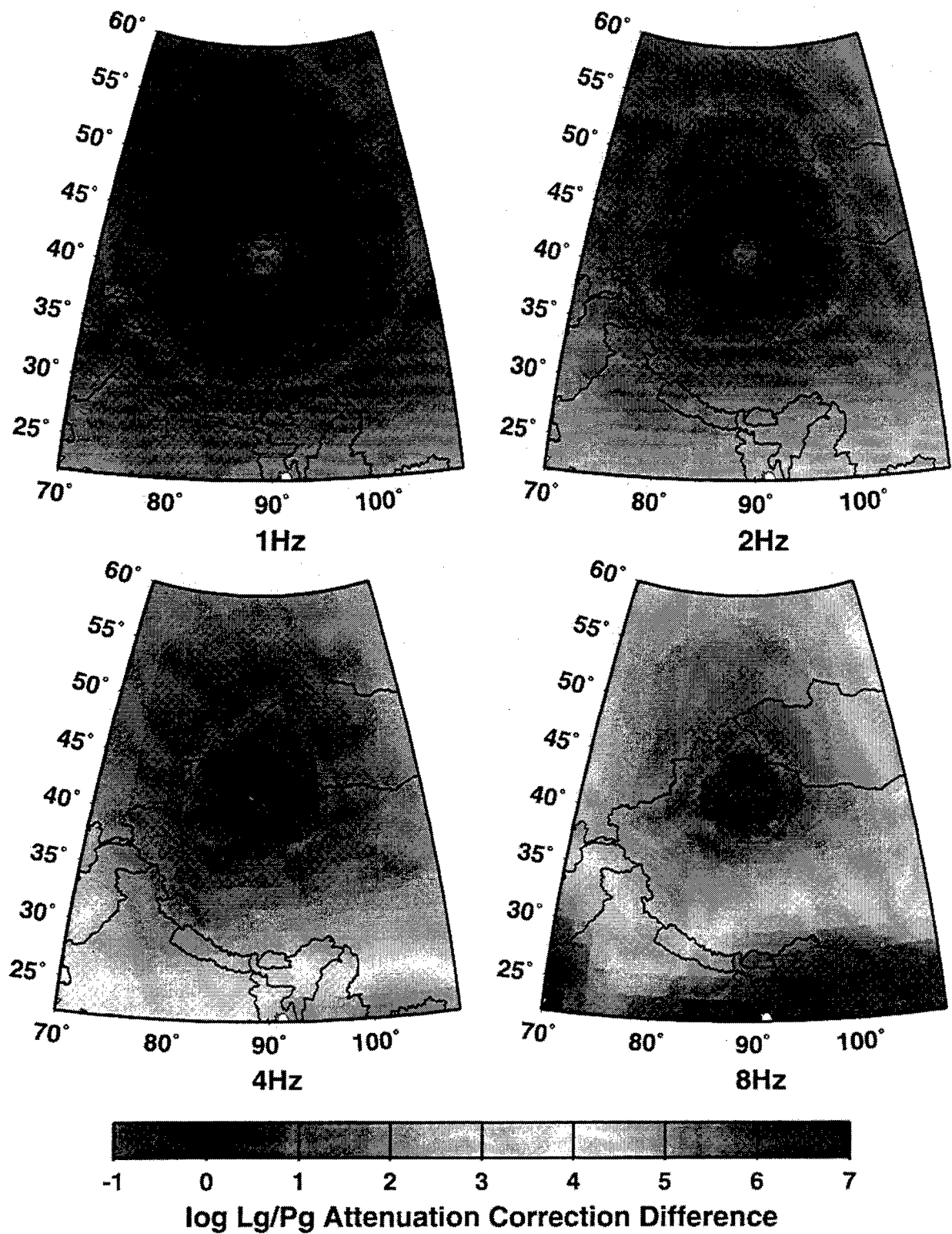


Figure 11. Predicted differences in  $L_g/P_g$  attenuation correction factors in the surrounding region of a source at Lop Nor China for four frequencies based on assumptions of  $Q_{P_g}=2.25Q_{L_g}$  and of  $Q_{P_g}=1.0Q_{L_g}$ .

Hz, between  $10^{-1}$  and  $10^3$  at 4 Hz, and between  $10^{-1}$  and  $10^4$  at 8 Hz. Again, the correction differences are seen to follow a generally radial pattern of increasing values with increasing distance; although there again appears to be a slight tendency for more rapid increase to the northwest and southeast away from the NTS source region, which is only really apparent at the highest frequencies. For the region surrounding Lop Nor in Figure 11, the difference in the  $L_g/P_g$  attenuation correction factors is between  $10^{-1}$  and  $10^{2.5}$  at 1 Hz, between  $10^{-1}$  and  $10^{3.5}$  at 2 Hz, between  $10^{-1}$  and  $10^{5.5}$  at 4 Hz, and between  $10^{-1}$  and  $10^{7.5}$  at 8 Hz. For the Lop Nor region the correction differences again appear to increase more rapidly toward southerly azimuths. Therefore, it seems clear that the range in the  $L_g/P_g$  attenuation correction will depend fairly strongly on the correct choice of the B parameter. It is anticipated that with some calibration efforts (particularly for  $P_g$  attenuation) it should be possible to more closely resolve  $L_g/P_g$  path corrections. Until then, it would appear to be expedient to place the most reliance on comparisons at comparable epicentral distances and at similar frequencies. In particular, these studies suggest that observations at closer regional distances and at lower frequencies should be less prone to variations introduced by propagation effects.

### 3.3.2 Effects of Attenuation Corrections on Observed $L_g/P_g$ Ratios

Given the uncertainties of  $P_g$  propagation characteristics and lacking a firm relationship between  $L_g$  and  $P_g$  attenuation, it would be premature to apply propagation corrections to large samples of  $L_g/P_g$  ratio observations. However, we did apply a nominal attenuation correction, based on the procedures described in the preceding section, to the  $L_g/P_g$  ratio measurements from a small sample of selected events to see what effects such adjustments might have on the discriminants. For the selected database, we used the regional signals at LLNL station KNB for five NTS nuclear explosions, all at distances of about 270 km, and for five earthquakes in the vicinity of NTS, at ranges from 200 km to 380 km. The same Gaussian band-pass filtering process, as described in Section 3.2 above, was used to determine the  $L_g/P_g$  ratios as a function of frequency. For  $P_g$  attenuation we assumed  $Q(P_g) = 1.67 Q(L_g)$  and derived the corrections to the  $L_g/P_g$  ratios following the method developed in Section 3.3.

Figure 12 shows the  $L_g/P_g$  ratios as a function of frequency for the five NTS explosions after corrections for attenuation. By comparing Figure 12 with Figure 5 above, we can see the effect of the corrections. The  $L_g/P_g$  ratios before the corrections showed an overall trend decreasing by about a factor of ten (from a ratio of about 2.5 to a ratio of about 0.3) between 0.5 Hz and 10 Hz. After the corrections, the  $L_g/P_g$  ratios over the same frequency range show a trend which is nearly flat with frequency, with the ratio values averaging about two. The corrections clearly have little effect on the scatter in the measurements between the different events; but this is to be expected since all five explosions have nearly the same path to KNB, and the signals would, therefore, experience approximately the same attenuation. We can conclude from this that the kind of variability (about a factor of five) seen in the  $L_g/P_g$  ratio measurements in Figure 12 is inherent in the observations and may be associated with source or random measurement differences. Figure 13 shows similar attenuation-corrected  $L_g/P_g$  ratios as a function of frequency for five earthquakes recorded at KNB. The overall trend of the  $L_g/P_g$  ratios in this case shows an increase of about a factor of three to four over the frequency range from 0.5 Hz to 10 Hz. So, after the attenuation corrections there still appears to be differences in the  $L_g/P_g$  ratios between earthquakes and explosions, with the earthquakes showing significantly higher ratios with the biggest differences at higher frequencies. Somewhat surprisingly the scatter in the earthquake observations isn't any greater than that of the explosions, and at some frequencies it may actually be less.

Figure 14 shows a comparison of the  $L_g/P_g$  ratio measurements and their associated standard deviations for the explosions and earthquakes in the small event sample before (top) and after (bottom) the attenuation corrections. The measurements for both the corrected and uncorrected  $L_g/P_g$  ratios are generally intermingled at frequencies below about 2 Hz, but above 2 Hz we see nearly complete separation at the mean  $\pm 1 \sigma$  level for both the corrected and uncorrected ratios. After the attenuation corrections have been applied, the average  $L_g/P_g$  ratios for the explosions are nearly level at a value of about two over the frequency from 3 Hz to 10 Hz. Over the same band the corrected earthquake  $L_g/P_g$  ratios show a slight increase with frequency and an average value of about ten. In fact, the factor of five difference in the ratios between the

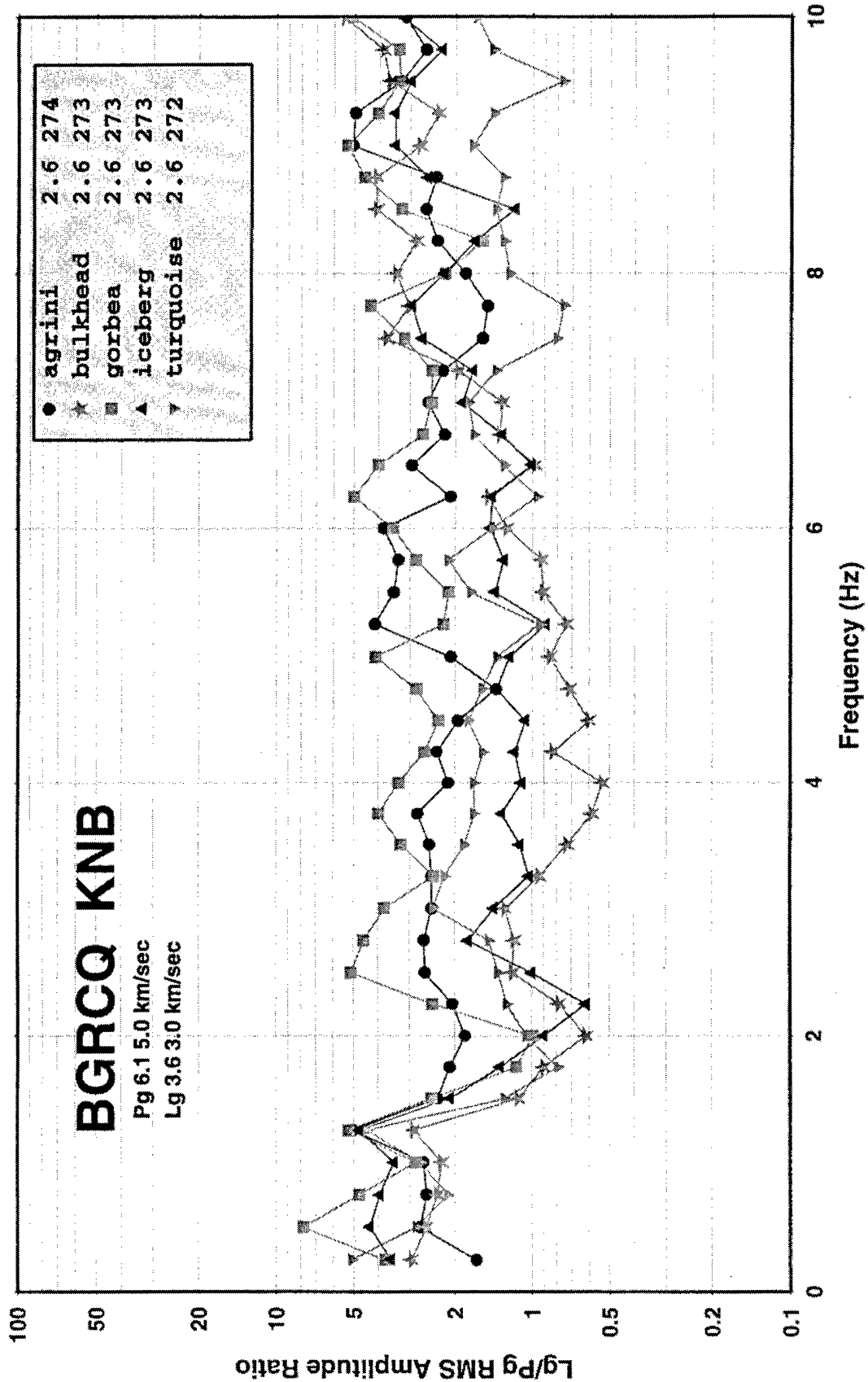


Figure 12.  $L_g/P_g$  ratios as a function of frequency at station KNB for 5 NTS explosions after corrections for attenuation.

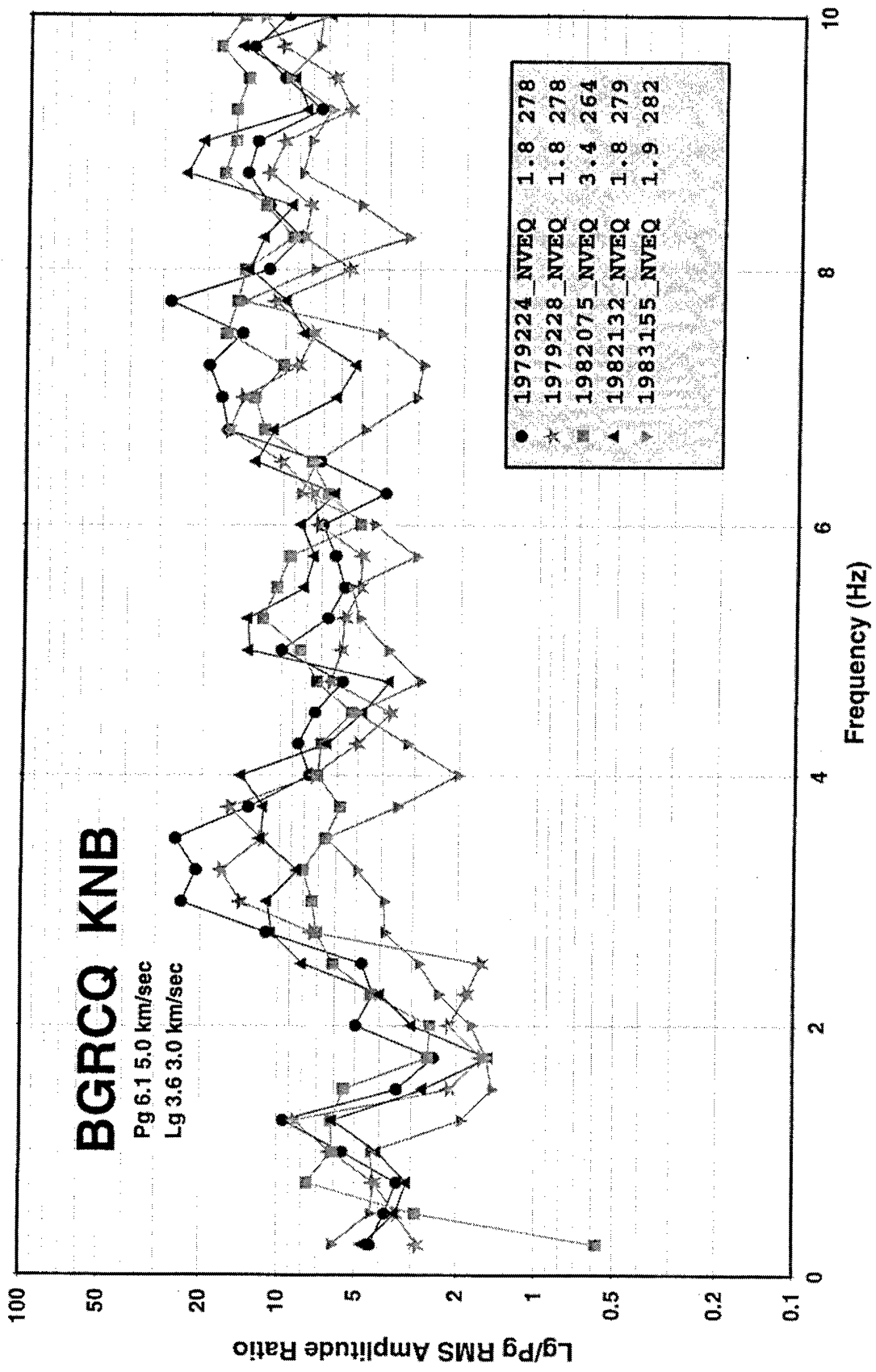


Figure 13.  $L_g/P_g$  ratios as a function of frequency at station KNB for 5 earthquakes near NTS after corrections for attenuation.

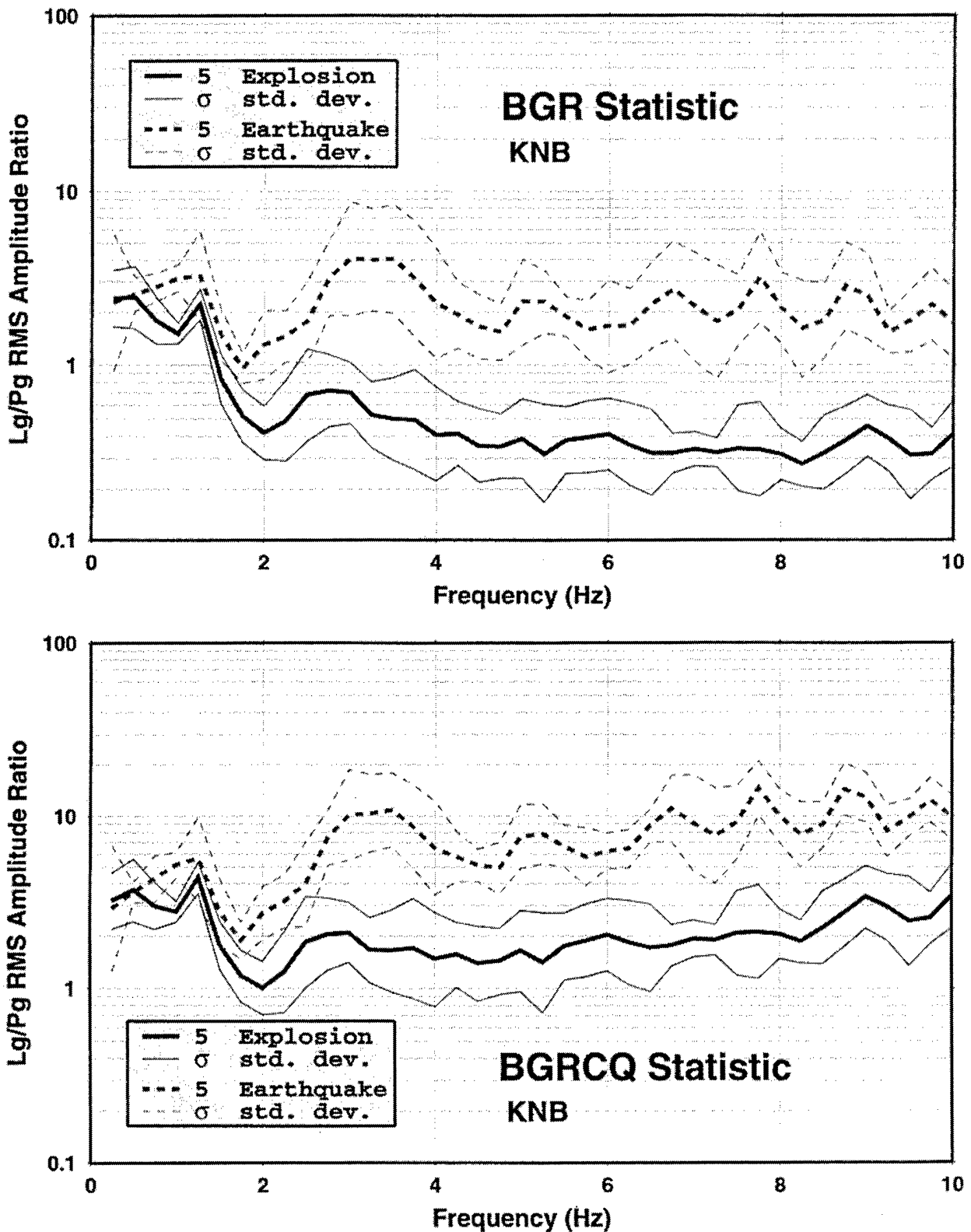


Figure 14. Comparison of mean and standard deviations for  $L_g/P_g$  ratios as a function of frequency for NTS explosions and nearby earthquakes recorded at LLNL station KNB before (top) and after (bottom) corrections for attenuation.

earthquakes and explosions does not seem to be affected much by the attenuation corrections. However, there does appear to be a slight improvement in the scatter for the measurements after the corrections have been applied. We notice the reduction in the scatter mainly for the earthquakes, because the source-station path for the explosions does not change much between events so that the path corrections there cannot do much to improve the scatter, as noted above.

## 4. Theoretical Modeling of $L_g/P_g$ Ratio Behavior

### 4.1 Constraints on $Q(L_g)$ -vs- $Q(P_g)$ From $L_g/P_g$ Ratio Observations

Many researchers have adopted a simple empirical attenuation model for regional phases. The model pre-supposes that regional phases are waves propagating in the crustal and upper mantle waveguides. They assume that the problem may be broken into source, path and receiver sections. The source type determines the initial spectral composition of the regional phase, the path consists of geometrical and anelastic attenuation, and receiver effects account for local site effects at each station. If we take the simple "empirical"  $L_g$  and  $P_g$  amplitude-frequency-distance model on face value then we would predict  $\text{Log}_{10}(L_g/P_g)$  values as a function of frequency,  $f$ , and distance,  $\Delta$ , of the form:

$$\text{Log}_{10}\left(\frac{L_g}{P_g}\right) = \text{Log}_{10}\left[\frac{A_{L_g}(f)}{A_{P_g}(f)}\right] \cdot (\pi \text{Log}_{10}(e) \cdot \Delta) \cdot \left[ \frac{f(1-\eta_{L_g})}{Q_0(L_g)U_{L_g}} - \frac{f(1-\eta_{P_g})}{Q_0(P_g)U_{P_g}} \right] + \varepsilon$$

where  $\text{Log}_{10}[A_{L_g}(f)/A_{P_g}(f)]$  is the initial relative excitation of  $L_g$  and  $P_g$  as a function of frequency for the specific source at distance. The  $Q_0$  and  $\eta$  describe the attenuation at 1 Hz and frequency dependence for the regional phases  $L_g$  and  $P_g$  which are propagating with group velocities of  $U_{L_g}$  and  $U_{P_g}$ . It is commonly assumed that this "source term" is the reason for differences between earthquake and explosion  $L_g/P_g$  spectral ratios and the physical basis for  $L_g/P_g$  discrimination.

It is also commonly assumed that intrinsic attenuation is dominated by shear attenuation. If the P-waves and S-waves pass through the same material, then we might

expect that the ratio of attenuation of the two wave types is given by the familiar 9/4's rule for a Poisson solid,  $Q(P_g)/Q(L_g) = 2.25$ . Assuming  $U_{Lg} = 3.5$  and  $U_{Pg} = 6.5$ , we plot predicted  $L_g/P_g$  spectral ratios in Figure 15 for some representative Q values assuming the initial  $L_g/P_g$  excitation ratio is flat with respect to frequency. If we compare the shapes of these plots with observed  $L_g$  to  $P_g$  plots from Bennett et al. (1997a) in Figures 3a and 3b above, we see that non-zero values of  $\eta$  are favored by observations.  $L_g/P_g$  spectral ratios fall off too quickly as a function of increasing frequency if Q does not increase with increasing frequency. There may also be some tradeoff between  $\eta$  and the  $Q(P_g)/Q(L_g)$  ratio. If  $\eta$  is not as large as 0.5 then observed  $L_g/P_g$  ratios may be consistent with  $Q(P_g)/Q(L_g)$  ratios less than 2.25.

#### 4.2 Synthetic Amplitudes from a World-Wide Collection of Crustal Models

We started with a collection of representative crustal models assembled by Mooney et al. (1997). Based on an extensive literature search, Mooney et al. have assigned a representative model for each 5 degree by 5 degree region upon the Earth. From their continental crustal models, listed in Table 1, we have constructed layered models suitable for computation of synthetic seismograms by placing each model on top of a PREM upper mantle model. Stevens and McLaughlin (1997) used these layered earth models as starting models in a world-wide surface wave inversion using 50- to 20-second group and phase velocity data to refine the S-wave velocities of these models. In this work we used the refined continental models of Stevens and McLaughlin to compute suites of synthetic seismograms at selected distances. We then measured  $P_g$  and  $L_g$  amplitudes from these synthetic seismograms using selected band-pass filters.

A map of the 5 by 5 degree regionalization of the Earth is shown in Figure 16. The continental models span a wide range of crustal types; they range from thin tectonic crusts to thick cratonic shields and from thin sediment cover to thick sediment cover. We have not used the oceanic crustal models in this study. In order to compute regional seismograms, we re-layered the models into maximum 1 km thick layers, applied an Earth flattening approximation, and assigned  $Q(f)$  as a function of depth and frequency. We describe in the next section our choice of  $Q(f)$  model.

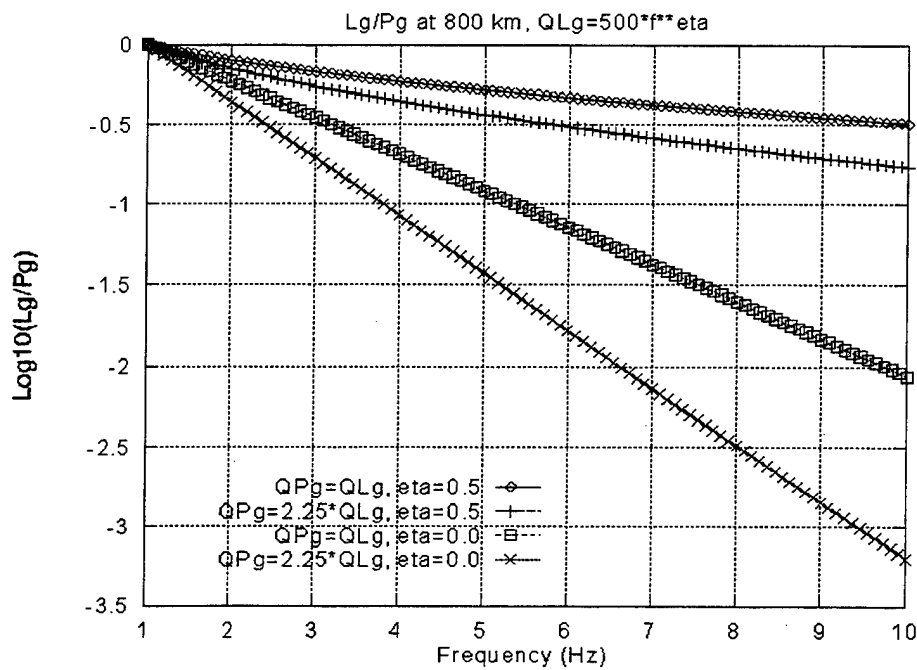


Figure 15. Predicted  $L_g/P_g$  spectral ratios normalized to 1 at 1 Hz for  $Q(L_g) = 500 * f^{\eta}$ , for two ratios of  $Q(L_g)/Q(P_g)$  and two values of  $\eta$ .  $L_g/P_g$  ratios fall off too quickly as a function of increasing frequency if  $Q$  is independent of frequency, i.e.  $\eta = 0$ .

Table 1. Listing of Mooney et al. (1997) CRUST 5.1 representative models with “two letter” designations used in the current work.

Model Code - Description
D2 Platform 10 km sediments. Stable Continent
D3 Platform 38 km, 5 km sediments Stable Continental
D4 Platform 46 km, 5 km sediments Stable Continental
D5 Thick Platform 2 km sediments Stable Continental
D6 Platform 2 km sediments Stable Continental
D7 Platform 4 km sediments Stable Continental
D8 Thick Platform 3 km sediments Stable Continental
D9 Platform 1 km sediments Stable Continental
DA Platform 6 km sediments Stable Continental
DB Platform 3 km sediments Stable Continental
DC Platform 0.5 km sediments Stable Continental
DD Platform 5.0 km sediments Stable Continental
DE Thick Platform 1 km sediments Stable Continental
G0 Archean 1 km sediments, Hudson Platform Stable Continental
G1 Archean, no sediments Stable Continental
G2 Archean 0.5 km ice, no sediments Stable Continental
G3 Archean 1 km ice, no sediments Stable Continental
G4 Archean 1.5 km ice, no sediments Stable Continental
G5 Archean 2.0 km ice, no sediments Stable Continental
G6 Archean 2.5 km ice, no sediments Stable Continental
G7 Archean 3.0 km ice, no sediments Stable Continental
G8 Archean 3.5 km ice, no sediments Stable Continental
G9 Archean 4.0 km ice, no sediments Stable Continental
GA Archean 0.5 km sediments Stable Continental
GB Archean 2.0 km sediments Stable Continental
GC Archean 3.5 km sediments Stable Continental

GD	Archean 6.5 km sediments Stable Continental
GE	Archean, no sediments Stable Continental
T1	Margin/shield transition, East Siberia, 2 km sediments Stable Continental
T2	Margin/shield 0.5 km ice, 2 km sediments Stable Continental
T3	Margin/shield 1 km ice, 2 km sediments Stable Continental
T4	Margin/shield 1.5 km ice, 2 km sediments Stable Continental
T5	Margin/shield transition, 5 km sediments Stable Continental
T6	Margin/shield transition, 1 km sediments Stable Continental
T7	Margin/shield transition, 3.5 km sediments Stable Continental
T8	Margin/shield transition, 8.0 km sediments Stable Continental
H0	early/mid Proterozoic., Finland thick, no sediments Stable Continental
H1	early/mid Proterozoic., no sediments Stable Continental
H2	early/mid Proterozoic shield, Finland, no sediments Stable Continental
H3	early/mid Proterozoic shield, Finland, 0.5 km sediments Stable Continental
H4	early/mid Proterozoic shield, Africa, 1.5 km sediments Stable Continental
H5	early/mid Proterozoic shield, Africa, 3 km sediments Stable Continental
I1	late Proterozoic thin sediments, no sediments Stable Continental
I2	late Proterozoic thicker sediments, 1 km sediments Stable Continental
I4	late Proterozoic thicker sediments, 2 km sediments Stable Continental
I5	late Proterozoic thicker sediments, 5 km sediments Stable Continental
I6	late Proterozoic thicker sediments, 3 km sediments Stable Continental
I7	late Proterozoic thicker sediments, 1 km sediments Stable Continental
I8	late Proterozoic thicker sediments, 7 km sediments Stable Continental
K1	forearc, New Zealand, California, 2 km sediments tectonic Continental
K2	forearc, New Zealand, California, 1 km sediments tectonic Continental
K3	forearc, New Zealand, California, 3 km sediments tectonic Continental
L1	continental arc, Kamchatka, Cascades, 2 km sediments tectonic Continental
L2	thin continental arc, Mexico, 2 km sediments tectonic Continental
L3	continental arc, Southern Andes, 1.0 km sediments tectonic Continental

L4	thin continental arc, Central America, 3.5 km sediments tectonic Continental
L5	thick continental arc, Southern Andes, 2.0 km sediments tectonic Continental
N1	extended crust, 3 km sediments tectonic Continental
N2	extended crust, 2 km sediments tectonic Continental
N3	extended crust, 1.5 km sediments tectonic Continental
N4	extended crust, 3 km sediments tectonic Continental
O1	highly extend crust, no ice tectonic Continental
O2	highly extended crust, 0.5 km ice tectonic Continental
O3	highly extended crust, 1 km ice tectonic Continental
O4	highly extended crust, 1.5 km ice tectonic Continental
O5	highly extended crust, 2 km ice tectonic Continental
O6	highly extended crust, 2.5 km ice tectonic Continental
O7	highly extended crust, 3 km ice tectonic Continental
X1	Rift, Rio Grande, Baikal tectonic Continental
P1	orogen/46km, Urals, Tethian Orogen, 2 km sediments tectonic Continental
P2	orogen/38km, Alps and Foreland, 2 km sediments tectonic Continental
P3	orogen/50km, Urals, Tethian Orogen, 6 km sediments tectonic Continental
P4	orogen/50km, Urals, Tethian Orogen, 1 km sediments tectonic Continental
Q0	orogen/46km no ice, Rockies, Tarim Basin, 4 km sediments tectonic Continental
Q1	orogen/40km no ice, Appalachians, North Andes Stable/tectonic Continental
Q2	orogen/40 km 0.5 km ice tectonic Continental
Q3	orogen/40 km 1 km ice tectonic Continental
Q4	orogen/40 km 1.5 ice tectonic Continental
Q5	orogen/40 km 2 km ice tectonic Continental
Q6	orogen/40 km 2.5 ice tectonic Continental
Q7	orogen/40 km 3 km ice tectonic Continental
Q9	orogen/40km no ice, Appalachians, North Andes, 1 km sediments Stable/tectonic Continental
QA	orogen/46km no ice, Appalachians, 3 km sediments Stable/tectonic Continental
R0	orogen/60km Tibet Transition, 1 km sediments tectonic Continental

R1 orogen/70km Tibet, 1 km sediments tectonic Continental
R2 orogen/65km Bolivia, 3 km sediments tectonic Continental
R3 orogen/70km Chile, 1 km sediments tectonic Continental
Z1 Phanerozoic, 1 km sediments Stable Continental
Z2 Phanerozoic, 0.5 km sediments Stable Continental
Z3 Phanerozoic, 2 km sediments Stable Continental
Z4 Phanerozoic, 4 km sediments Stable Continental
A0 normal oceanic, 0.15 km sediments Stable Oceanic
A1 normal oceanic 0.5 km sediments Stable Oceanic
A2 normal oceanic 1 km sediments Stable Oceanic
A3 normal oceanic 2 km sediments Stable Oceanic
A4 normal oceanic 3 km sediments Stable Oceanic
A5 normal oceanic 4 km sediments Stable Oceanic
A6 normal oceanic 5 km sediments Stable Oceanic
A7 normal oceanic 6 km sediments Stable Oceanic
A8 normal oceanic 7 km sediments Stable Oceanic
A9 normal oceanic 9 km sediments Stable Oceanic
AA normal oceanic 10 km sediments Stable Oceanic
B0 melt affected o.c. and oceanic plateaus, 0.20 km sediments Tectonic Oceanic
B1 melt affected o.c. and oceanic plateaus, 0.5 km sediments Tectonic Oceanic
B2 melt affected o.c. and oceanic plateaus, 1 km sediments Tectonic Oceanic
B3 melt affected o.c. and oceanic plateaus, 2 km sediments Tectonic Oceanic
B4 melt affected o.c. and oceanic plateaus, 3.5 km sediments Tectonic Oceanic
B5 thick melt affected o.c., no sediments Tectonic Oceanic
B6 thick melt affected o.c., 0.5 km sediments Tectonic Oceanic
B7 thick melt affected o.c., 1 km sediments Tectonic Oceanic
B8 melt affected o.c. and oceanic plateaus, 4.5 km sediments Tectonic Oceanic
C0 continental shelf, 0.25 km sediments Stable Continental
C1 continental shelf, 0.5 km sediments Stable Continental

C2 continental shelf, 1 km sediments Stable Continental
C3 continental shelf, 2 km sediments Stable Continental
C4 continental shelf, 3.5 km sediments Stable Continental
C5 continental shelf, 5.5 km sediments Stable Continental
C6 continental shelf, 7.5 km sediments Stable Continental
C7 continental shelf, 6.5 km sediments Stable Continental
C8 continental shelf, 10 km sediments Stable Continental
J1 island arc, Japan, Antarctic, 1 km sediments tectonic Continental
J2 island arc, 3.5 km sediments tectonic Oceanic
J3 island arc, 2.5 km sediments tectonic Oceanic
J4 island arc, 5.0 km sediments tectonic Oceanic
Y1 thinned cont. crust, Red Sea tectonic Oceanic
Y2 intermediate. Continental./Oceanic. crust, Black Sea tectonic Oceanic
Y3 inactive ridge 2 km sediments, Alpha Ridge tectonic Oceanic
Y4 oceanic plateau with Continental. crust, 0.25 km sediments Stable Oceanic
Y5 oceanic plateau with Continental. crust, 1 km sediments Stable Oceanic
Y6 oceanic plateau with Continental. crust, 2 km sediments Stable Oceanic
Y7 Caspian depression, 12 km sediments tectonic Oceanic
Y8 oceanic plateau with Continental. crust, 4 km sediments Stable Oceanic
S1 continental slope, margin, transition 1 km sediments Stable/tectonic Oceanic
S2 continental slope, margin, transition 2 km sediments Stable/tectonic Oceanic
S3 continental slope, margin, transition 3.5 km sediments Stable/tectonic Oceanic
S4 continental slope, margin, transition 5.5 km sediments Stable Oceanic
S5 continental slope, margin, transition 8 km sediments Stable Oceanic
S6 continental slope, margin, transition 4.5 km sediments Stable Oceanic
S7 continental slope, margin, transition 7 km sediments Stable Oceanic

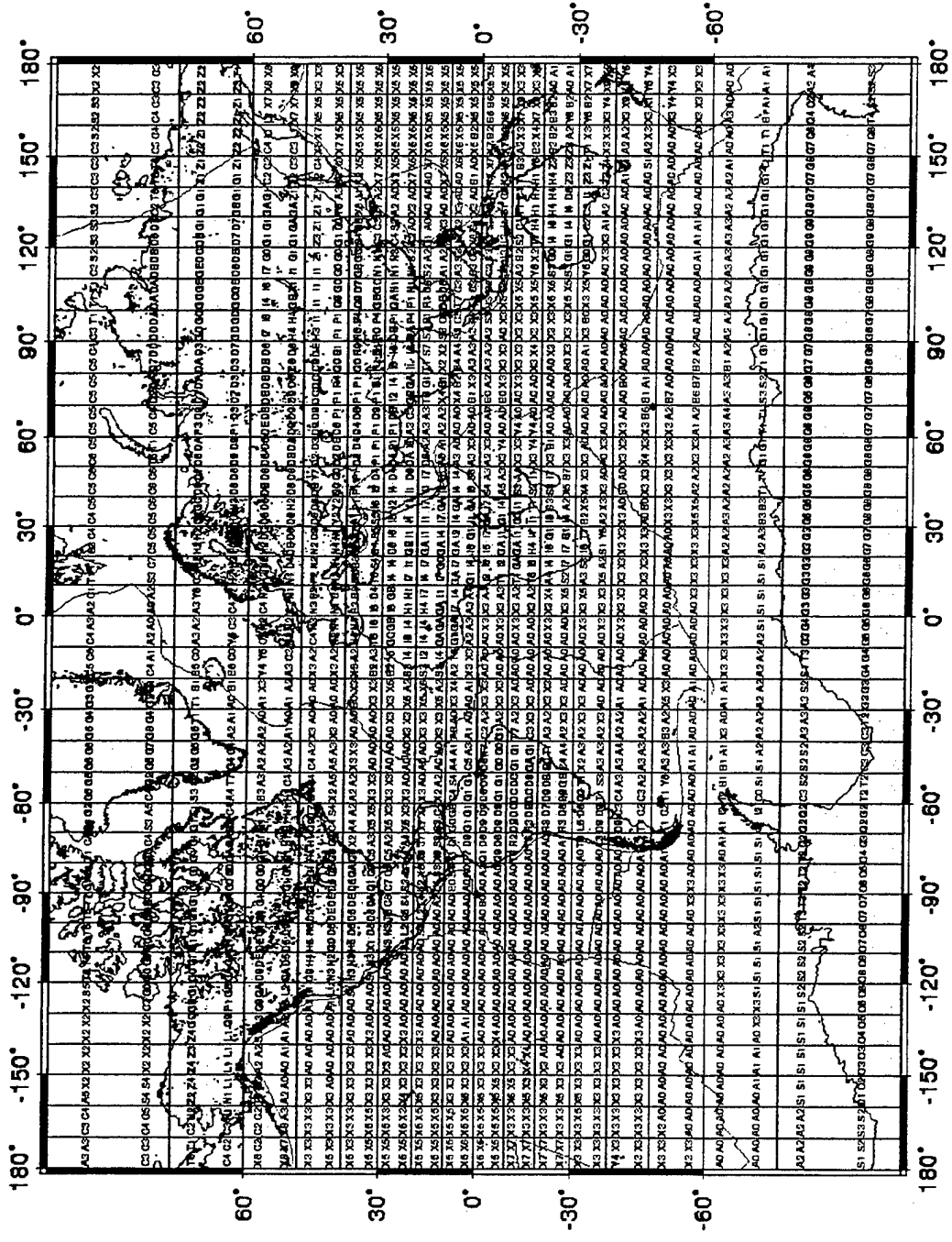


Figure 16. Map showing the Mooney et al. (1997) world-wide regionalization for the two letter code representative models listed in Table 1. Only the continental models were used to construct regional synthetics for  $L_g/P_g$  analysis.

#### 4.3 Random Layering and Choice of a $Q(f, z)$ Model

Attenuation in each layer is specified by bulk,  $Q_k(f)$ , and shear,  $Q_\mu(f)$ . The bulk  $Q_k(f)$  was assumed to be infinite. Recall that for the compressional wave,  $Q_p = 1/(x/Q_\mu + (1-x)/Q_s)$  where  $x = 4/3(\beta/\alpha)^2$  while for the shear wave,  $Q_s = Q_\mu$ . For a Poisson solid this leads to  $Q_p/Q_s = 2.25$ . Frequency dependence of  $Q$  was parameterized by  $Q(f) = Q_0 * f^\eta$ , where  $Q_0$  is the value at 1 Hz. Calculations were done for  $\eta = 0$  (frequency independent) and  $\eta = 0.5$ . Except at the shallowest depths, we assumed  $Q_0$  equal to  $\beta/5$  ( $\beta$  in m/s) at depths less than 100 km. The uppermost 1 km layer was assigned a shear  $Q_0$  of 25 and the next two 1 km thick layers were assigned  $Q_0$  values of 75 and 150 respectively. The low  $Q$  layers near the surface served to attenuate short-period  $R_g$  from shallow sources. For comparison, a set of calculations were done with  $Q_0$  equal  $\beta/10$  and  $\eta = 0$  (frequency independent  $Q$ ) in all layers (high  $Q$  surface layers).

It has been suggested that introduction of random velocity variations into a layered crustal model produces more realistic looking regional phases (Harvey, 1992). Therefore, a 5% RMS random velocity variation was introduced into both P and S wave velocities through-out each model (cf. Figure 17). Figures 18 and 19 show comparisons of synthetic seismograms for one of the crustal models with and without the 5% random variation. The dependence of  $L_g$  and  $P_g$  upon this form of random layering is described in more detail in McLaughlin et al. (1997). We find that random layering of 5 to 10% has some desirable but secondary effects upon the  $L_g$  and  $P_g$  waveforms. The  $L_g/P_g$  spectral ratios as a function of frequency are largely unaffected with 0, 2.5%, 5.0%, 7.5% and 10% RMS random velocity layers (cf. Figure 20 and Figure 21). A wavenumber integration synthetic seismogram program (Apsel and Luco, 1983; McLaughlin, 1996) was used to compute Green's functions for sources at 1 km and 15 km at ranges of 200, 400, 600, and 800 km from 0 to 5 Hz. The individual Green's functions were then used to construct synthetic seismograms for isotropic explosion sources,  $G_i$ , horizontally oriented tension crack,  $G_{tc}$ , a vertically oriented CLVD,  $G_{clvd}$ , and strike-slip,  $G_{ss}$ , thrust,  $G_{th}$ , and dip-slip,  $G_{ds}$ , double couples.

Figure 22 and Figure 23 compare synthetics computed for the D2 crustal model with three different  $Q$  models:

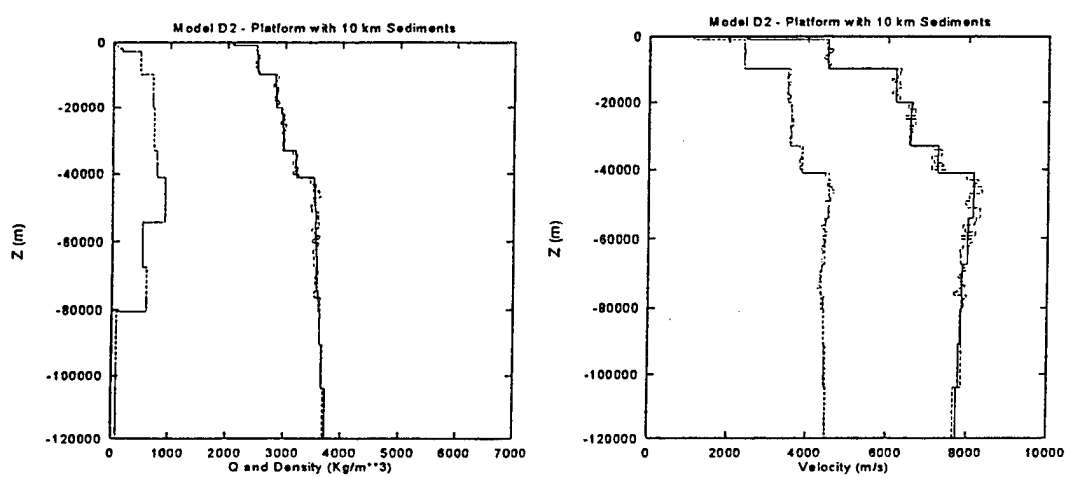


Figure 17. The D2 crustal model with and without a 5% RMS random velocity variation used to construct regional synthetics. Shear Q at 1 Hz and density are shown on the left while shear and compressional velocities are shown on the right.

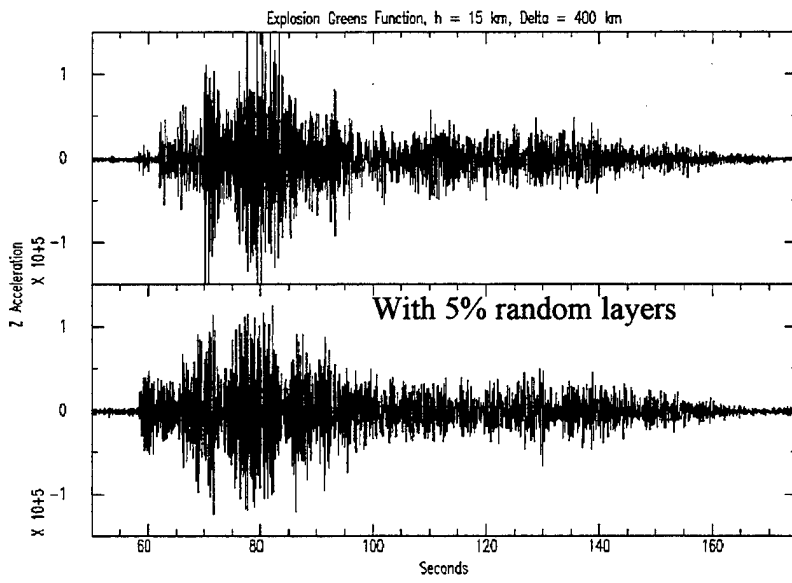


Figure 18. Comparison of synthetic seismograms with and without the 5% random velocity variation in the layered model shown in Figure 17. Note the more developed  $P_n$  signals and the reduced "spikes" in the  $P_g$  from the randomized structure.

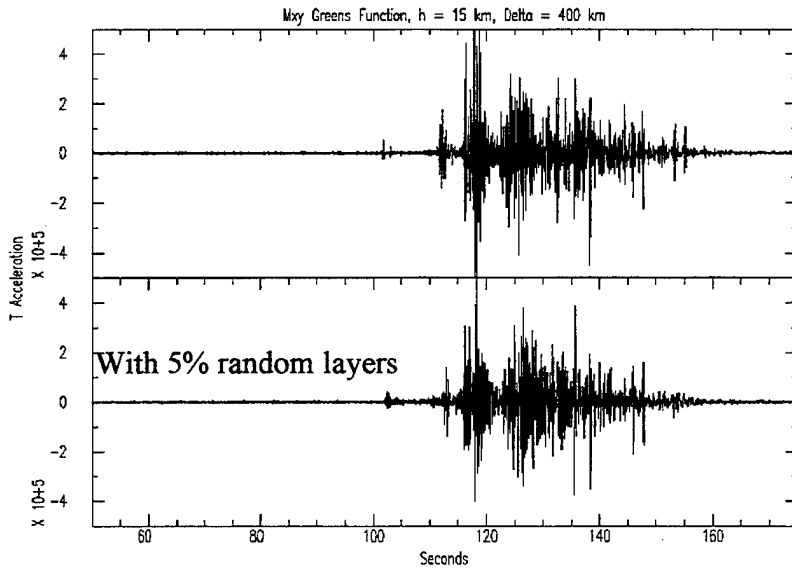


Figure 19. Comparison of synthetic seismograms with and without the 5% random velocity variation in the layered model shown in Figure 17. Note that the more developed  $S_n$  arrival from the random layered structure and that the isolated "spikes" in the  $L_g$  signal are reduced.

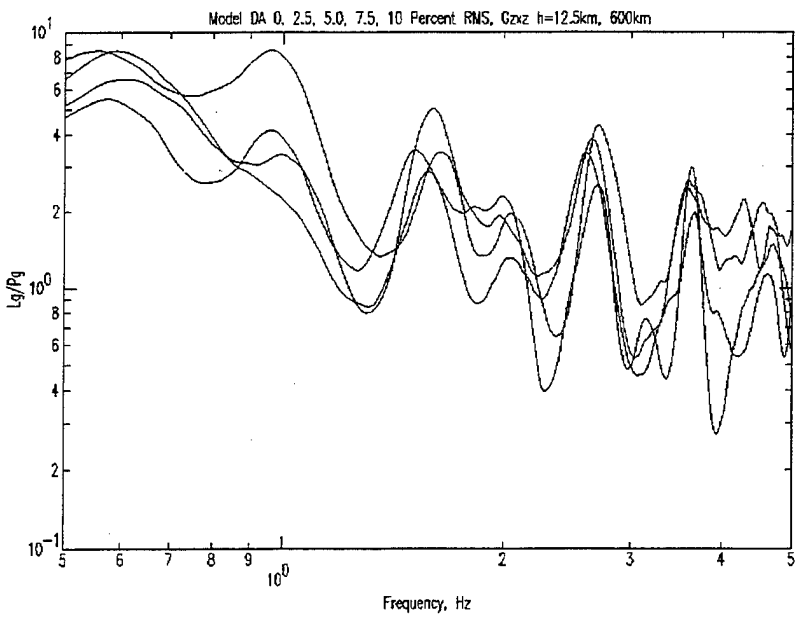


Figure 20.  $L_g/P_g$  earthquake spectral ratios at 600 km for crustal model DA with 0, 2.5, 5.0, 7.5, and 10% RMS random layering. General character of the  $L_g/P_g$  spectral ratio is unaffected by the random layering.

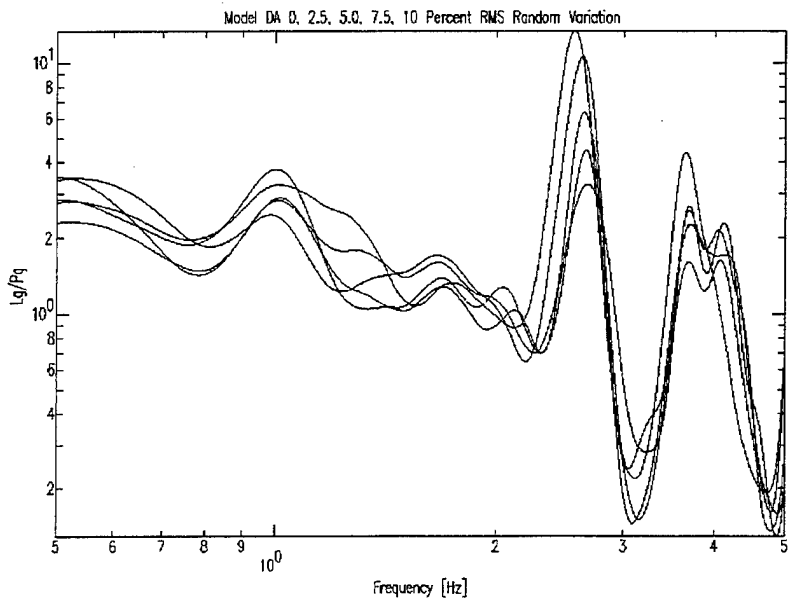


Figure 21.  $L_g/P_g$  explosion spectral ratios at 400 km for crustal model DA with 0, 2.5, 5.0, 7.5, and 10% RMS random layering. Shallow sediments in this model exhibit a rather large resonance for an explosion source at 1 km depth.

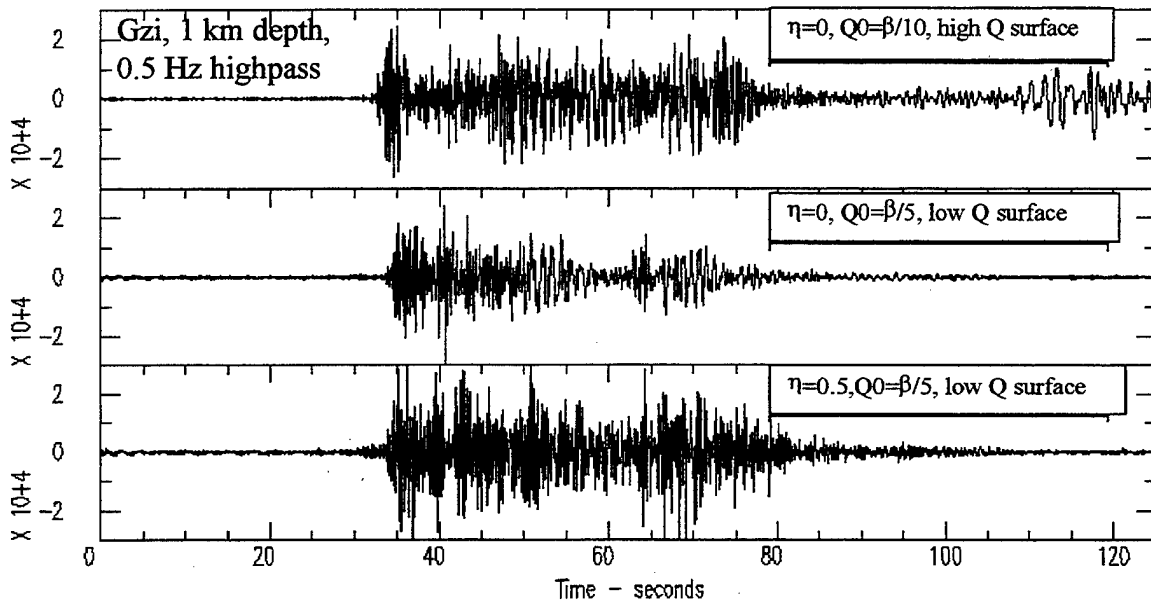
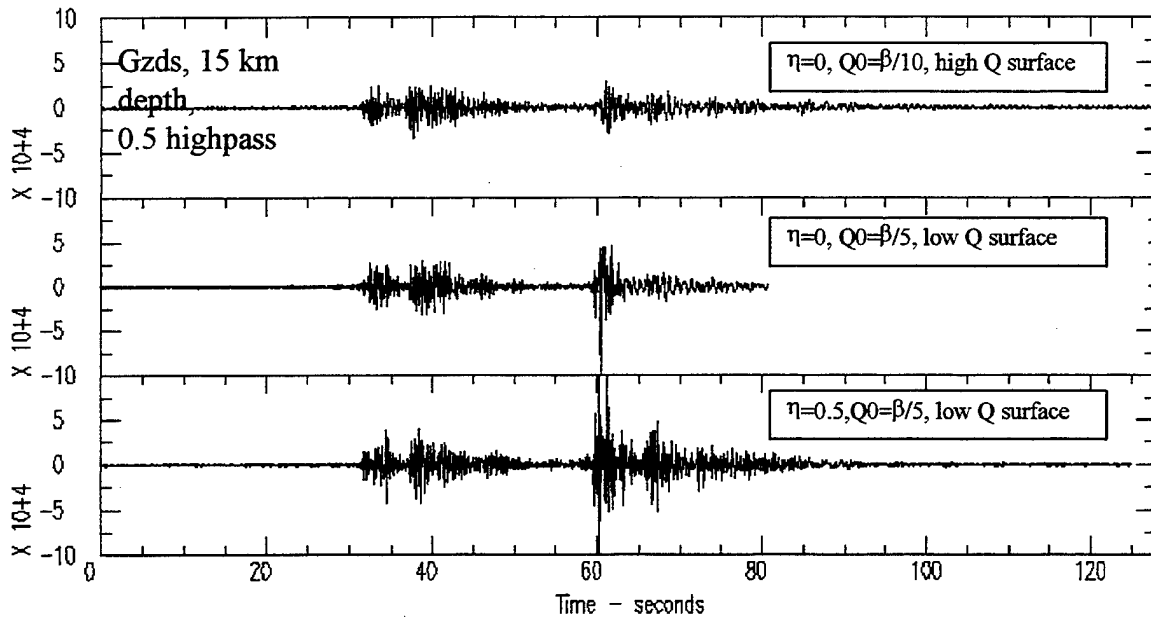


Figure 22. Comparison of vertical component synthetics (high pass at 0.5 Hz) at 200 km for three  $Q(f)$  models and the randomized crustal velocity model D2 shown in Figure 17. A dip-slip double-couple source (Gzds) at 15 km depth is shown above and an explosive source (Gzi) at 1 km depth is shown below. The earthquake  $L_g$  amplitude is significantly increased relative to the  $Pg$  amplitude for the  $\eta=0.5$ ,  $Q_0=\beta/5$ ,  $Q$  model. The high  $Q$  surface layer model does not sufficiently attenuate the late arriving fundamental surface waves excited by the shallow explosive source. Also, it is clear that the  $\eta=0$ ,  $Q_0=\beta/10$ , high  $Q$  surface layer model contains much shallow propagating energy in the  $L_g$  window that is absent in the low  $Q$  surface layer models.

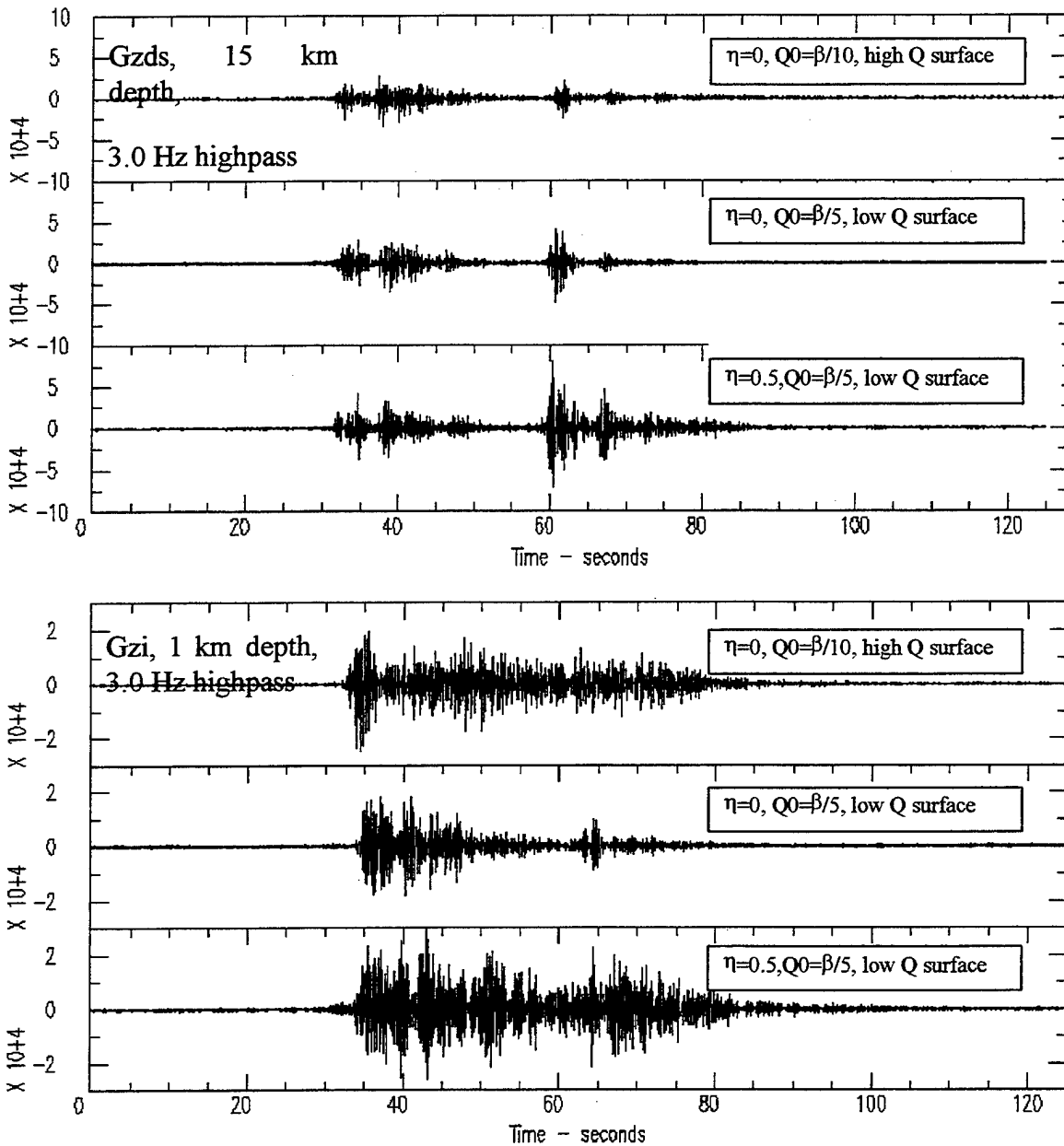


Figure 23. Comparison of vertical component synthetics (high pass at 3.0 Hz) at 200 km for three  $Q(f)$  models and the randomized crustal velocity model D2 shown in Figure 17. A dip-slip double-couple source (Gzds) at 15 km depth is shown above and an explosive source (Gzi) at 1 km depth is shown below. Earthquake  $L_g/P_g$  ratios greater than 1 at frequencies above 3 Hz favor either the  $\eta=0.5$ ,  $Q_0=\beta/5$  or  $\eta=0.0$ ,  $Q_0=\beta/5$  models over the  $\eta=0.0$ ,  $Q_0=\beta/10$  model. Even at frequencies above 3 Hz, the shallow explosion Green's function for the high Q surface layer model contains shallow propagating energy in the  $L_g$  window not apparent in the low Q surface layer models.

- Q1.)  $\eta = 0$ ,  $Q_{0\mu} = \beta / 10$  for  $z > 0$  m, high Q surface layers,
- Q2.)  $\eta = 0$ ,  $Q_{0\mu} = \beta / 5.0$  for  $z > 2000$  m, low Q surface layers and
- Q3.)  $\eta = 0.5$ ,  $Q_{0\mu} = \beta / 5.0$  for  $z > 2000$  m, low Q surface layers.

It is clear from the synthetics in Figure 22 and Figure 23 that model Q3 is better than either model Q1 or Q2. First, low Q surface layers are required to attenuate unwanted higher modes and  $R_g$ . Second, average Q values in the crust must generally produce  $L_g/P_g$  ratios greater than unity near 1 Hz for earthquake mechanisms. Third, the  $L_g/P_g$  ratio as a function of frequency must be relatively flat. Figures 3a and 3b above, based on a compilation of  $L_g/P_g$  ratios from Bennett et al. (1997a), show that earthquake  $L_g/P_g$  ratios slowly decrease with increasing frequency. Synthetics from the bulk of the crustal models suggested that, in order to produce earthquake-like  $L_g/P_g$  ratios greater than unity near 1 Hz, the higher  $Q_0$  values of models 2 and 3 are preferred to those of model 1. Also, to keep  $L_g/P_g$  ratios relatively flat as a function of frequency, an increase in  $Q_\mu$  as a function of frequency ( $\eta > 0$ ) is needed. The  $L_g/P_g$  ratios above 1 Hz for models 1 and 2 were too small and do not agree with observations.  $L_g$  Q increasing with increasing frequency is commonly observed (Nuttli, 1981, Mitchell 1981, Campillo et al., 1985, Goncz et al, 1986, Gupta and McLaughlin, 1987;) with  $\eta$  between 0 and 1. It should be noted that numerous researchers have found a negative correlation between  $Q_0$  and  $\eta$ ; the higher Q is at 1 Hz the slower it increases with increasing frequency. Therefore, it may be possible to reproduce many of the observed results by assuming higher  $Q_0$  values with somewhat smaller values of  $\eta < 0.5$ . Since we found that Q models 1 and 2 did not even begin to reproduce observed  $L_g/P_g$  ratios, we will not discuss these models further and concentrate on synthetics generated using Q model 3.

#### 4.4 “Empirical” Models of Excitation and Attenuation Based on Synthetic $L_g$ and $P_g$

There is utility in having simple empirical models for the excitation and attenuation of  $P_g$  and  $L_g$  as a function of mechanism, distance and frequency. These simple models have application in network simulations, automatic association, magnitude determination, and event characterization. Synthetic seismograms at 200, 400, 600 and

800 km range were band-pass filtered in eight bands (0.5-1.0, 0.75-1.5, 1.0-2.0, 1.5-3.0, 2.0-4.0, 3.0-6.0, 4.0-8.0, 6.0-8.0 Hz) and the maximum of the envelope in each of several group velocity windows was recorded. Five group velocity windows (100-20, 10-6.8, 6.8-4.6, 4.6-3.8, 3.8-2.5 km/sec) were used to capture numerical noise,  $P_n$ ,  $P_g$ ,  $S_n$ , and  $L_g$  respectively. The synthetic amplitudes from 80 models, 4 distances, 8 bandpasses, 5 group velocity windows, and 6 combinations of depth and mechanism were saved to a small database ( $80*4*8*5*6 = 76,800$  values). This database forms the basis for much of our analysis. The database of band-pass filtered amplitudes is available upon request ([scatter@maxwell.com](mailto:scatter@maxwell.com)).

The  $P_g$  and  $L_g$  time-domain amplitudes,  $A(f, \Delta)$ , as a function of frequency and range were then fit to “empirical” models for each crustal structure and moment tensor source where

$$\text{Log}_{10}(A(f, \Delta)) = A_0 - n \text{ Log}_{10}(\Delta/100) - \pi \text{ Log}_{10}(e) \Delta f^{(1-\eta)} / Q_0/U + \varepsilon.$$

The RMS values of the error term,  $\varepsilon$ , were generally between 0.3 and 0.6  $\text{Log}_{10}$  units for most crustal models. Note that  $A_0$  is independent of frequency in this model for both  $P_g$  and  $L_g$  excited by the earthquake source. A geometric spreading of  $n=5/6$  was used and group velocities of  $U = 6.5$  and  $3.5$  km/sec were used for  $P_g$  and  $L_g$  respectively. Examples of the log-likelihood functions for the fit of  $Q_0$  and  $\eta$  for  $P_g$  and  $L_g$  are shown in Figure 24 for crustal model D2 and a dip-slip double-couple source at 10 km depth. The log-likelihood function in this case is simply minus the L2 norm (RMS residual) normalized to its optimum value. The distinctive tradeoff between  $Q_0$  and  $\eta$  is clearly seen in the elongate contours of likelihood. Synthetics were generated with an  $\eta = 0.5$  and the inversion nearly recovers this value but favors a slightly higher value. The average model shear  $Q_{\mu 0}$  in the crust was about 500-600 while the inversion favors a higher value. There is an apparent bias between the “empirical model”  $Q(f)$  and the layered crustal model  $Q(f)$  used to generate the synthetics. The amplitude versus frequency and distance methodology tends to favor bias in the estimation of both  $Q_0$  and  $\eta$ . Different exponents of geometrical spreading,  $n = 0.5$  and  $n = 1$ , were tried but resulted in even larger biases between crustal model  $Q$  values and the empirical model  $Q$ .

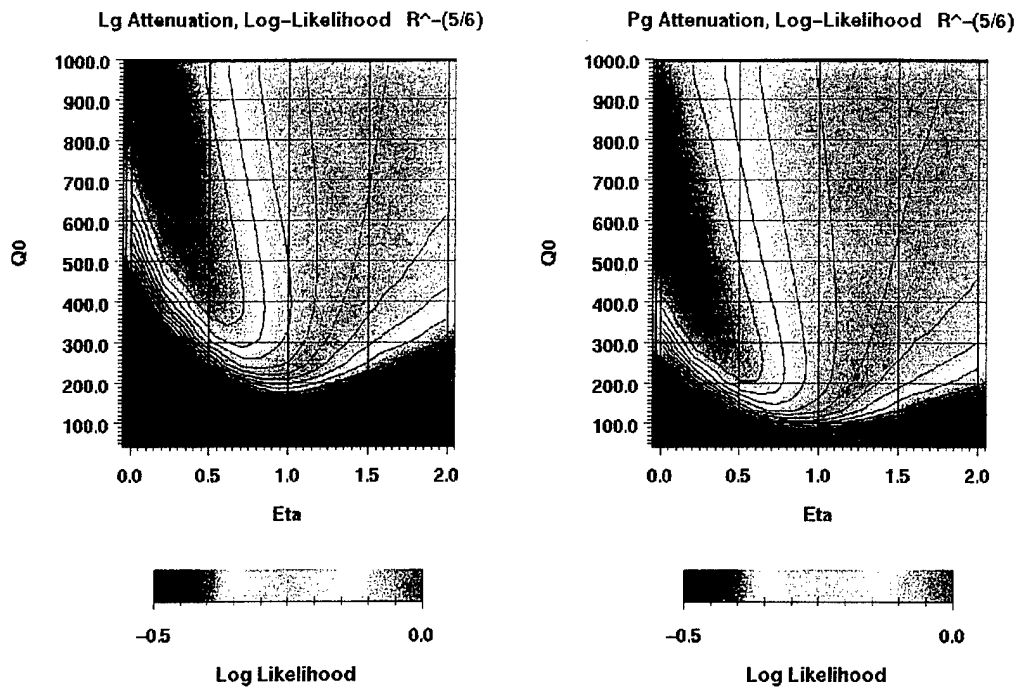


Figure 24. Log-likelihood as a function of the model parameters,  $Q_0$  and  $\eta$ , for empirical  $L_g$  and  $P_g$  Q models,  $Q(f) = Q_0 \cdot f^n$ , based on fits to synthetic  $L_g$  and  $P_g$  amplitude versus frequency and distance time-domain measurements for a dip-slip double-couple at a depth of 15 km in the crustal model D2. The inversion assumed  $n=5/6$ . Note the elongate contours and trade-off between  $Q_0$  and  $\eta$ .

values. The data could be fit with a variety of geometrical spreading exponents, but none were closer to the known crustal  $Q(f)$  of the model.

The results of these  $L_g$  and  $P_g$   $Q(f)$  fits for mechanism and crustal model are summarized in Figures 25 through 32 in which we plot estimated “empirical” values of  $Q(L_g)$  vs  $Q(P_g)$  at 1 Hz and  $\eta_{Lg}$  vs  $\eta_{Pg}$  for all of the crustal models and six source mechanisms. The scatter from this population of models is surprising and enlightening. This synthetic data does not have the problems of site effects, focusing-defocusing, or scattering, yet we see that even the synthetic data exhibits trade-offs and systematic biases. Several results for the synthetic  $Q$  models are clear from examination of Figures 25 through 32:

- $Q(P_g)$  does not equal 2.25 times  $Q(L_g)$  regardless of the source mechanism. The apparent earthquake  $Q(P_g)$  values are usually smaller than the  $Q(L_g)$  values. The earthquake mechanisms scatter about a trend with  $Q_0(L_g) = Q_0(P_g) + 100$ . The explosion  $Q_0(P_g)$  values are distributed almost independent of the  $Q_0(L_g)$  values.
- There is little difference between the population of  $Q$  models for the three shallow axi-symmetric sources. The explosion, tension crack and CLVD sources appear to excite  $P_g$  and  $L_g$  waves that propagate in a similar manner.
- There are systematic differences between the  $Q$  models fit to the different earthquake sources at depth. Dip-slip mechanisms exhibit lower  $Q_0$  values for  $P_g$  and  $L_g$  and higher  $\eta$  than the other double-couple mechanisms. For many of the crustal models, the strike-slip and thrust mechanisms exhibit systematically higher  $Q_0$  values and lower  $\eta$ .
- There is a strong trade-off tendency between  $Q_0$  and  $\eta$ . The explosion models scatter about  $\eta = 0.5$  which was used for the calculations, while values from 0.1 to 0.8 will often fit the data with a corresponding trade-off in  $Q_0$ .
- Most crustal models were computed with an average  $Q_0$  between 500 and 600. There is a central tendency for the results to scatter about this region. However, earthquake strike-slip and thrust mechanism  $Q_0$  values are generally greater than 600 with  $\eta$  values less than 0.3.

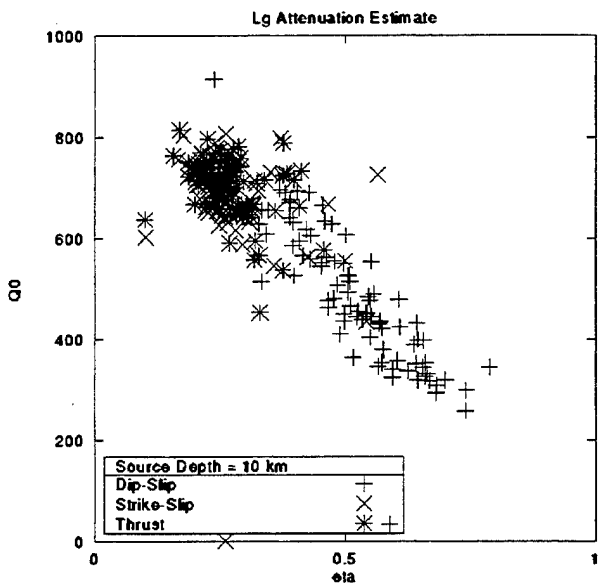


Figure 25.  $L_g$   $Q_0$  and  $\eta$  model estimates for all crustal models. Three kinds of double-couple earthquake sources are shown with depth of 10 km and dip-slip, strike-slip, and 45 degree thrust/reverse orientations. The dip-slip orientations show a systematically lower  $Q_0$  and higher  $\eta$ .

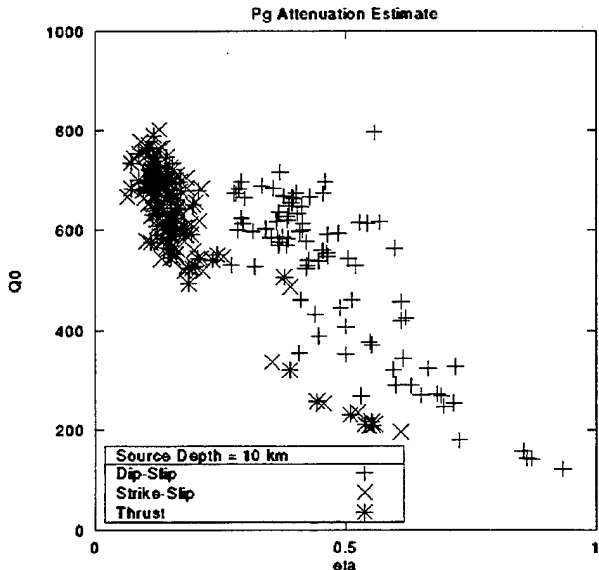


Figure 26.  $P_g$   $Q_0$  and  $\eta$  model estimates for all crustal models. Three kinds of double-couple earthquake sources are shown with depth of 10 km and dip-slip, strike-slip, and 45 degree thrust/reverse orientations. The dip-slip orientations show a systematically lower  $Q_0$  and higher  $\eta$ .

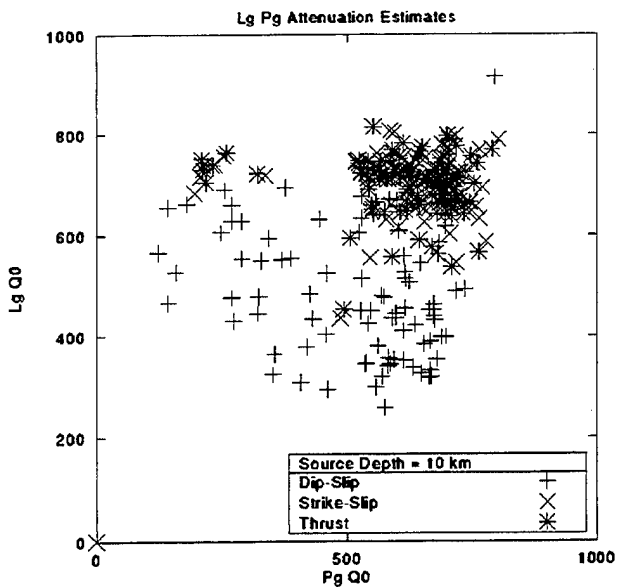


Figure 27.  $L_g Q_0$  versus  $P_g Q_0$  model estimates for all crustal models. Three kinds of double-couple earthquake sources are shown with depth of 10 km and dip-slip, strike-slip, and 45 degree thrust/reverse orientations. The dip-slip mechanisms have the largest scatter of the three mechanisms.

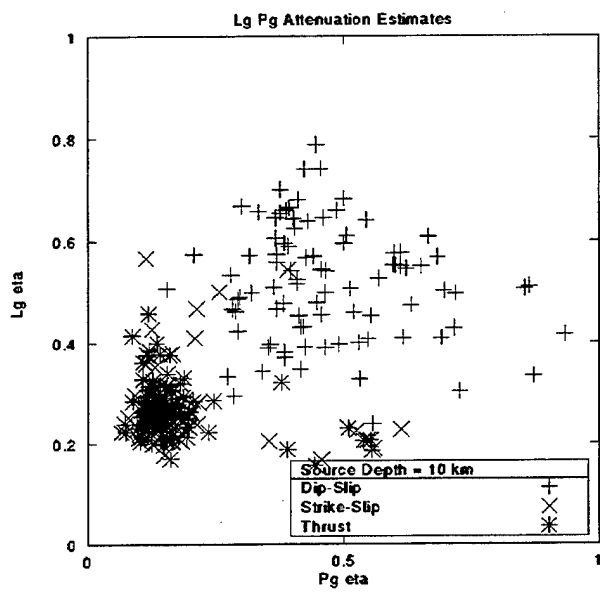


Figure 28.  $L_g \eta$  versus  $P_g \eta$  model estimates for all crustal models. Three kinds of double-couple earthquake sources are shown with depth of 10 km and dip-slip, strike-slip, and 45 degree thrust/reverse orientations.

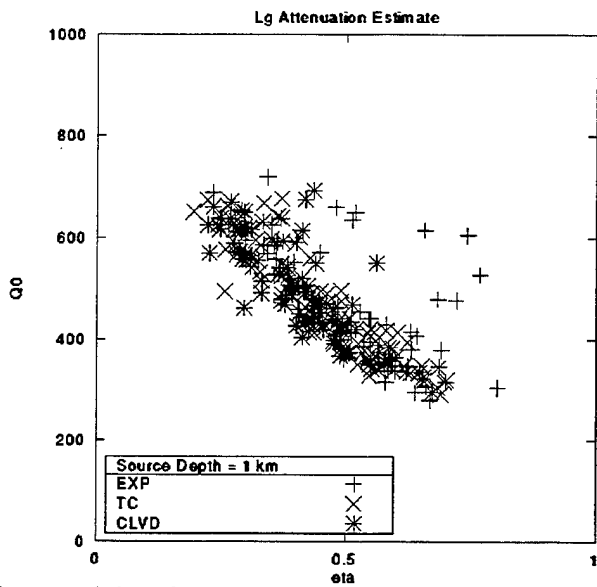


Figure 29.  $L_g$   $Q_0$  and  $\eta$  model estimates for all crustal models. Three kinds of shallow axi-symmetric source are shown with depth of 1 km, explosion (EXP), horizontal tension crack (TC), and compensated linear vector dipole (CLVD). There does not appear to be any systematic differences in the attenuation as a function of mechanism. There is however strong trade-off between  $Q_0$  and  $\eta$ .

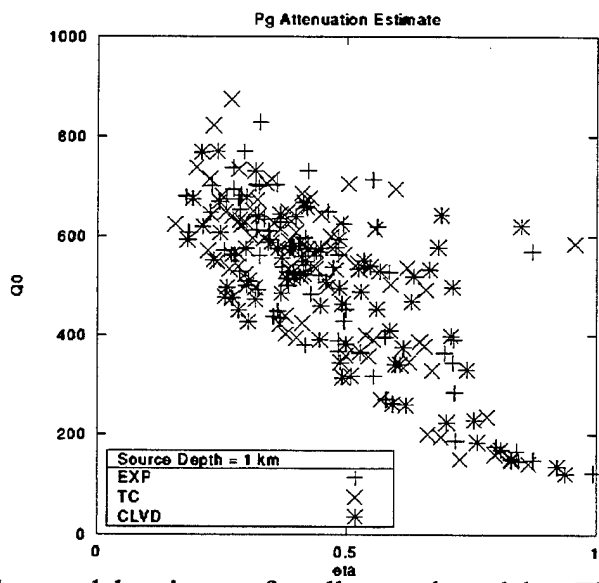


Figure 30.  $P_g$   $Q_0$  and  $\eta$  model estimates for all crustal models. Three kinds of shallow axi-symmetric source are shown with depth of 1 km, explosion (EXP), horizontal tension crack (TC), and compensated linear vector dipole (CLVD). There does not appear to be any systematic differences in the attenuation as a function of mechanism. There is however a strong trade-off between  $Q_0$  and  $\eta$ . The results are somewhat more scattered than the  $L_g$   $Q_0$  and  $\eta$  estimates.

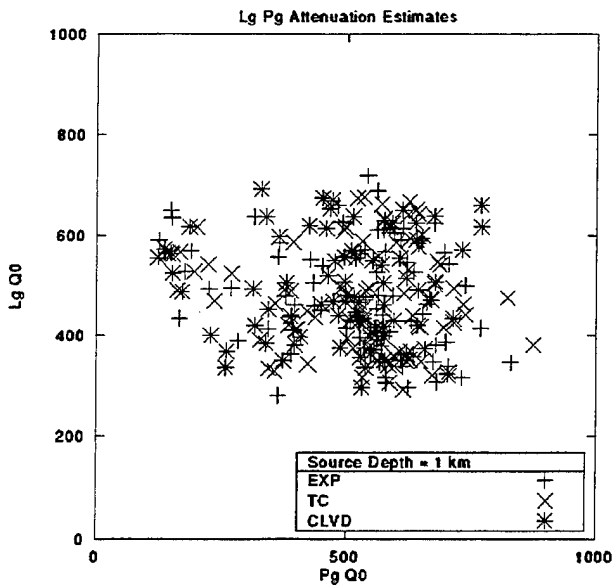


Figure 31.  $L_g Q_0$  versus  $P_g Q_0$  model estimates for all crustal models. Three kinds of shallow axi-symmetric source are shown with depth of 1 km, explosion (EXP), horizontal tension crack (TC), and compensated linear vector dipole (CLVD). There does not appear to be any systematic differences in the attenuation as a function of mechanism. The  $P_g Q_0$  values are somewhat more scattered than the  $L_g Q_0$  values.

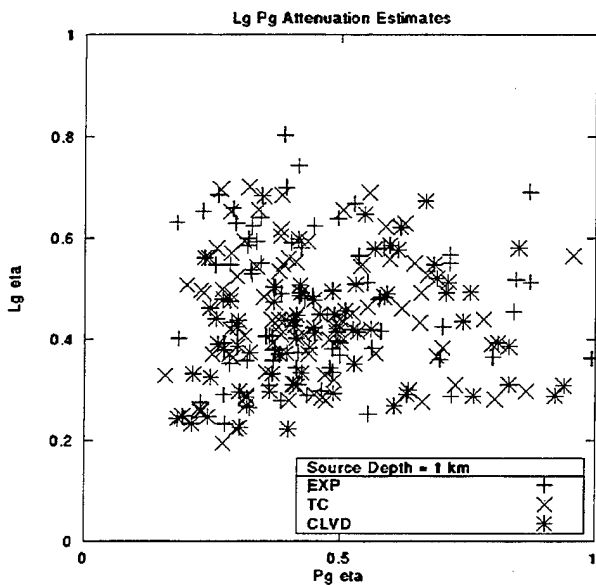


Figure 32.  $L_g \eta$  versus  $P_g \eta$  model estimates for all crustal models. Three kinds of shallow axi-symmetric source are shown with depth of 1 km, explosion (EXP), horizontal tension crack (TC), and compensated linear vector dipole (CLVD). There does not appear to be any systematic differences in the attenuation as a function of mechanism. The  $P_g \eta$  values are somewhat more scattered than the  $L_g \eta$  values.

#### 4.5 Clustering Based on Explosion-Earthquake $L_g/P_g$ Ratios

We extracted from each crustal model the  $L_g/P_g$  synthetic amplitude ratios at a distance of 400 km for an explosion at 1 km depth and the dip-slip double-couple source for the three passbands of 1.0-2.0, 2.0-4.0 and 4.0-8.0 Hz. We then used these 6 data points per crustal model to cluster the models. A cluster diagram is shown in Figure 33. The models fell into three natural clusters or groups. The models for each of the groupings are plotted in Figures 34 - 36. The largest group, Group #1 corresponds to all models with sedimentary layers thicker than 2 km. The explosion source at 1 km, therefore, lies within the sediments of each of these models. The second largest group, Group #2, is comprised of models with thin sediment layers on the order of 1 km thick or less. The explosion source lies near the bottom of the sediment layer in each of these models. The third group consists of models, H1, I1, G1, GE, H0, and H2 which have high velocity layers directly at the surface. The  $L_g/P_g$  ratios at 400 km for the two source types/depths are shown in Figures 37 -39. Most models exhibit earthquake  $L_g/P_g$  ratios greater than explosion  $L_g/P_g$  ratios as we expect, and the dispersion of earthquake  $L_g/P_g$  ratios tends to be smaller than the scatter of explosion  $L_g/P_g$  ratios. The biggest differences between the models are the explosion source excitations. Models with little or no low-velocity sediments in the upper 2 km have small  $L_g/P_g$  explosion source terms. The models with lower near-surface velocities have higher  $L_g/P_g$  explosion source terms and are harder to discriminate. Figure 40 shows the distribution of three model groups based upon the Mooney et al. (1997) regionalization.

#### 4.6 Discussion of Theoretical Modeling Results

We have presented analyses of layered Earth Green's functions for models representative of large regions of the Earth. We have computed Green's function for several distances, with a common Q model and analyzed the apparent attenuation of  $P_g$  and  $L_g$  as a function of source type and model. Simple "empirical" attenuation models based on the synthetic data exhibit large variance in the estimated  $Q_0$  and  $\eta$ . Strong trade-off tendencies are observed in the population of crustal models. Some systematic tendencies can be observed for some mechanisms. Q values for  $P_g$  are not related to Q

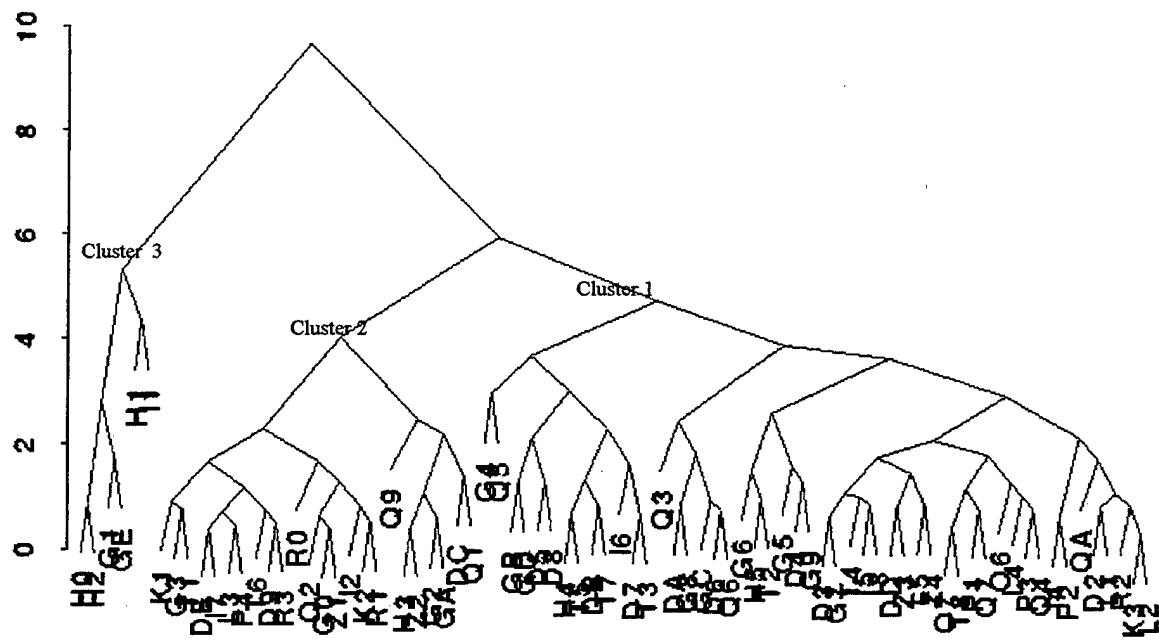


Figure 33. A cluster diagram for the data set of  $L_g/P_g$  ratios at 400 km at 1-2, 2-4 and 4-6 Hz passbands. The  $L_g/P_g$  ratios fall into three natural clusters.

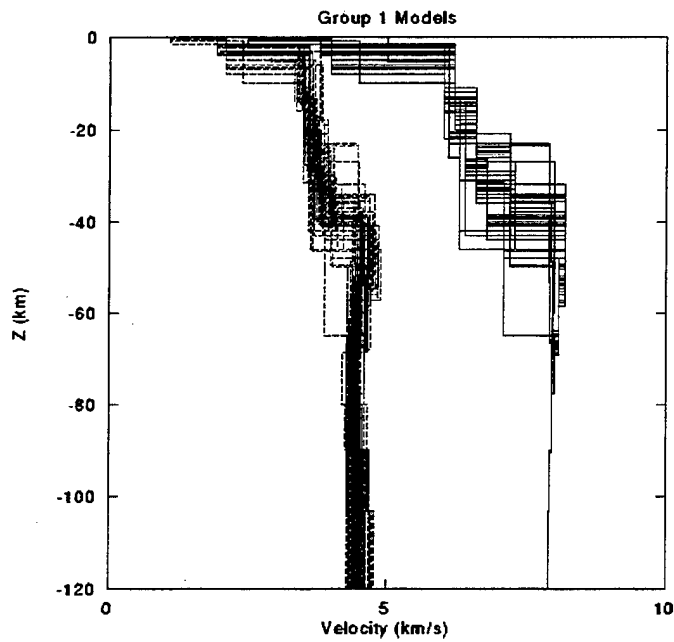


Figure 34. Group 1 consists of majority of models with surface sedimentary layers thicker than 1 km.

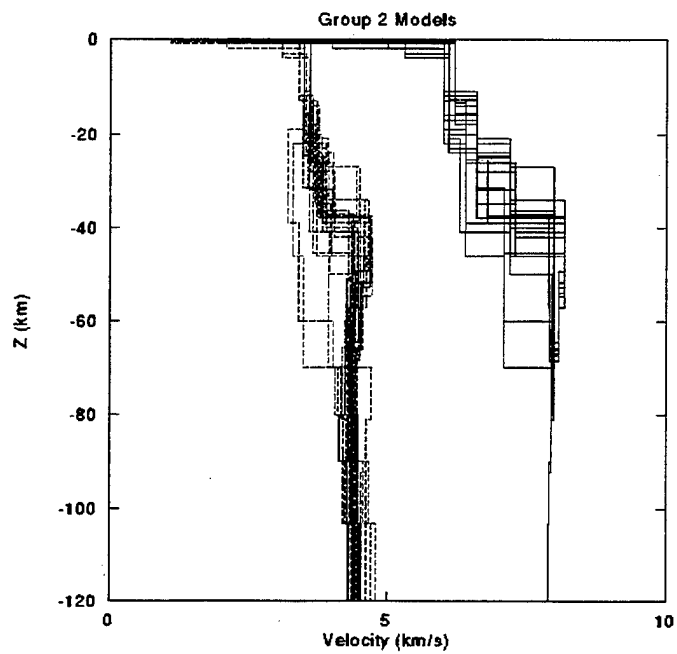


Figure 35. Group 2 consists of models with thin sedimentary layers at the surface underlain by high velocities.

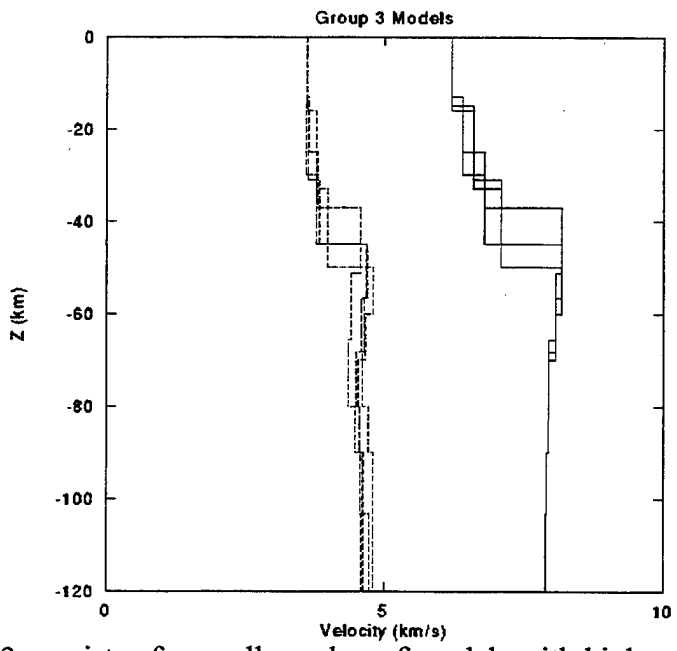


Figure 36. Group 3 consists of a small number of models with high velocities at the free surface.

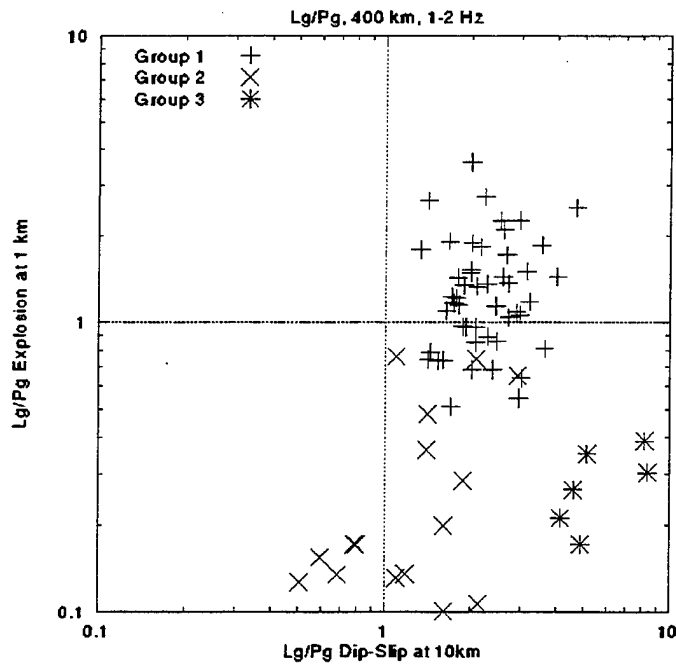


Figure 37. Plot of Explosion  $L_g/P_g$  ratio versus dip-slip  $L_g/P_g$  ratios in the 1-2 Hz passband for all models. All but a small number of Group #2 models have earthquake  $L_g/P_g$  ratios greater than unity in this bandpass. Many of the models in Group #1 have explosion  $L_g/P_g$  ratios greater than unity.

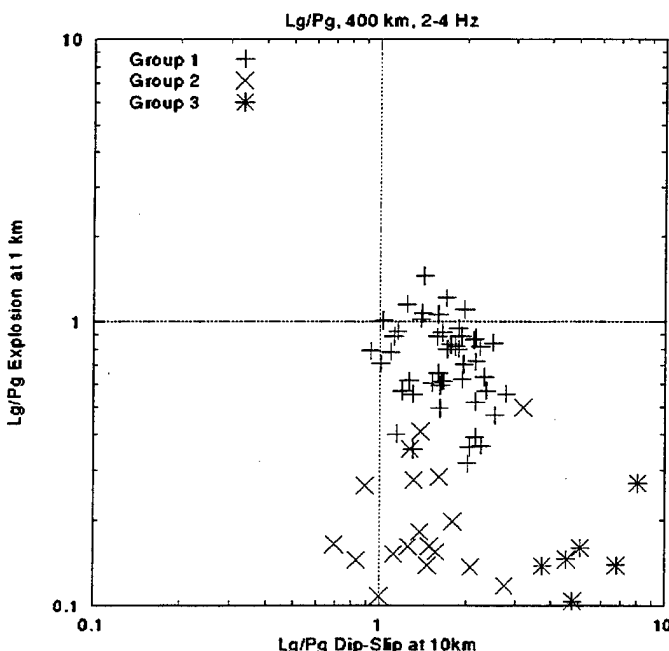


Figure 38. Plot of Explosion  $L_g/P_g$  ratio versus dip-slip  $L_g/P_g$  ratios in the 2-4 Hz passband for all models. All but a small number of Group #1 and #2 models have earthquake  $L_g/P_g$  ratios greater than unity in this passband. Only a few of the models in Group #1 have explosion  $L_g/P_g$  ratios greater than unity.

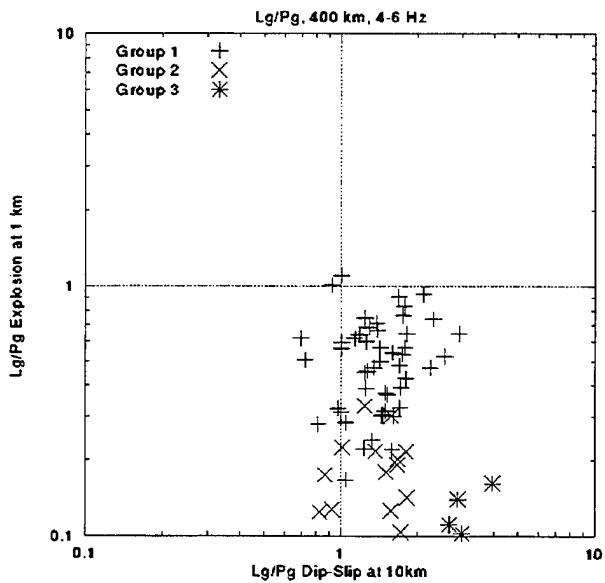


Figure 39. Plot of Explosion  $L_g/P_g$  ratio versus dip-slip  $L_g/P_g$  ratios in the 4-6 Hz passband for all models. All models have earthquake  $L_g/P_g$  ratios greater than 0.7. Only two in Group #1 have similar explosion and earthquake  $L_g/P_g$  ratios near unity.

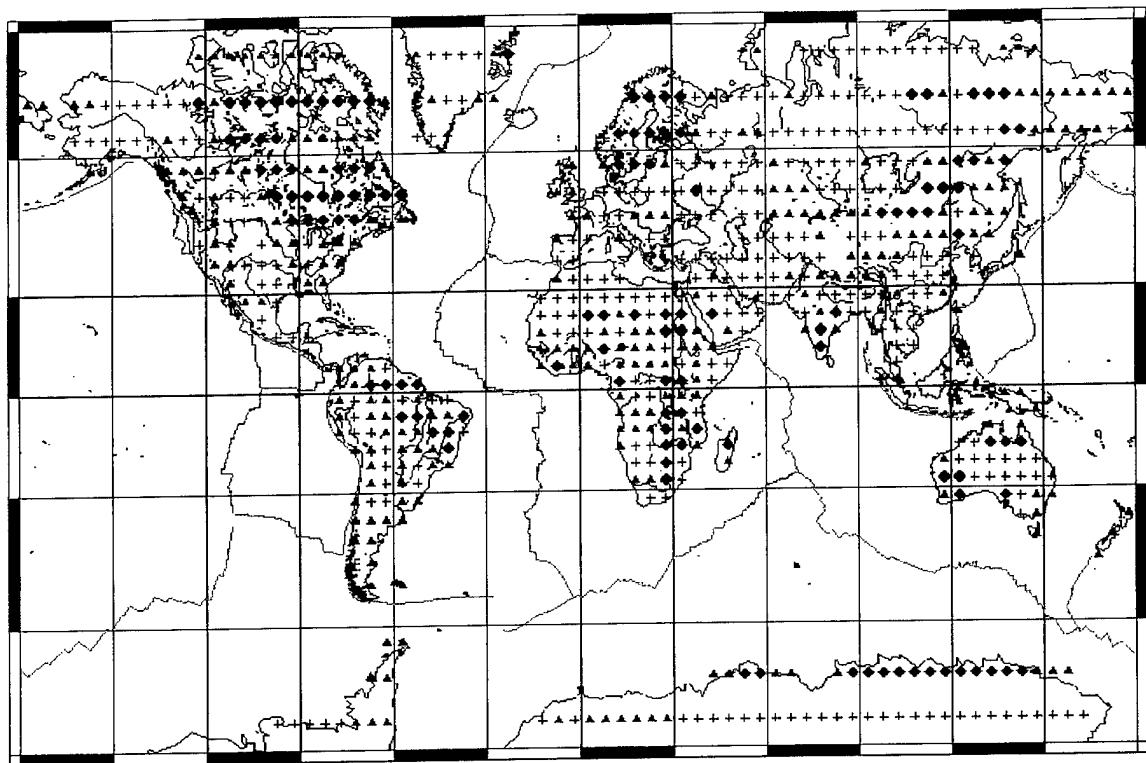


Figure 40. Distribution of the three groupings of models, Cross = Group #1, Solid Triangle = Group #2, and Solid Diamond = Group #3. Grouping/clustering is based upon  $L_g/P_g$  ratios of explosion and earthquake sources in three bandwidths.

values for  $L_g$  by the 9/4's law.  $Q$  values for synthetic  $P_g$  are often smaller than  $Q$  values for synthetic  $L_g$ , depending upon source type and crustal structure. Since  $P_g$  is composed of leaky P-SV modes, it appears to be controlled by the average shear-wave  $Q$  of the crust and not the corresponding compressional wave  $Q$ .

We find that the models fall into three general categories or groups based on explosion and earthquake  $L_g/P_g$  ratios. The three model groups correspond to regions with 1) thick, 2) thin, and 3) no sediments. The crustal thickness and upper mantle velocities were secondary to the thickness of the sediments in their effects on the model calculations.

## 5. Discrimination Analysis of the August 16, 1997 Kara Sea Event

### 5.1 General Characteristics of Regional Waveform Data

We have investigated the regional seismic signals from the  $3.9 m_b$  event near Novaya Zemlya ( $72.6^\circ N$   $57.4^\circ E$ ) on 1997/08/16. In our studies we made no attempt to review the location or origin time of the event but relied on the origin provided by the IDC at CMR. We concentrated on the signals recorded by the individual station elements and not the array-enhanced data in our processing. The waveform data were collected from eight stations at ranges from 1070 km to 2335 km. The stations were Apatity on the Kola peninsula in Russia ( $R = 1070$  km), Kevo in Finland ( $R = 1125$  km), Norilsk in the central Siberia area of Russia ( $R = 1180$  km), Spitzbergen off the northern coast of Norway ( $R = 1280$  km), the FINESSA regional array station in Finland ( $R = 1815$  km), the Arti station in the Russian Ural mountains ( $R = 1815$  km), the Hagfors station in Sweden ( $R = 2315$  km), and the NORESS regional array station in Norway ( $R = 2335$  km).

We performed band-pass filter analyses on the signals that were available and compared the results to prior experience with small regional tectonic events in this same area (e.g. 1992/12/31  $m_b = 2.8$  and 1995/06/13  $m_b = 3.8$  events), with NZ nuclear explosions (e.g. 1990/10/24  $m_b = 5.7$  nuclear test), and with experience elsewhere for a

variety of different source types. The map in Figure 41 shows the locations of events in the vicinity of NZ used in these comparisons. The best regional signals (highest signal-to-noise levels) for the 1997/08/16 NZ event were obtained at the nearer regional stations: Apatity, Kevo, Spitzbergen, and Norilsk. All four of these stations showed strong regional S-wave arrivals on the vertical-component records. Some of these stations also showed strong regional S waves on two horizontal components, which may be another diagnostic that this event was not an explosion. At the more distant stations (viz. FINESSA, Hagfors, Arti, and NORESS), the regional signals were weaker. P waves dominated the records at FINESSA, Hagfors, and NORESS; these were fairly broadband at NORESS and Hagfors but only rose above noise in a limited frequency range at FINESSA. At Arti only the S signal appeared above the background noise and was relatively weak.

## 5.2 Comparison of Band-Pass Filter Results

Figures 42 and 43 compare the results of band-pass filter analyses of the vertical-component signals at station Kevo for the 1997/08/16 NZ event and the 1990/10/24 NZ nuclear test. The top trace in each figure is the original broadband record, and the next traces are for filter passbands 4 - 8 Hz, 3 - 6 Hz, 2 - 4 Hz, 1 - 3 Hz, and 0.5 - 1.5 Hz respectively. We see from these analyses that for the 1997/08/16 event S/P ratios are near 1.0 for all passbands except for the lowest frequencies. In contrast, S/P ratios for the 1990/10/24 NZ nuclear explosion are above 1.0 on the broadband records and for the passbands at lower frequencies but are well below 1.0 (0.5 or less) for the higher frequency passbands (viz. 4 - 8 Hz, 3 - 6 Hz, and 2 - 4 Hz). We regard this behavior as diagnostic that the 1997/08/16 NZ event is different from NZ nuclear explosions. These kinds of differences are typical of the behavior previously seen from NZ events (cf. Bennett et al., 1993; Ringdal, 1997) as well as for comparisons of regional signals from nuclear explosions and other source types from other tectonic regions.

We performed similar band-pass filter analyses for one of the more distant stations, NORESS, using the same set of filters. The regional S signals for the 1997/08/16 NZ event were found to be very weak and apparently were masked by the

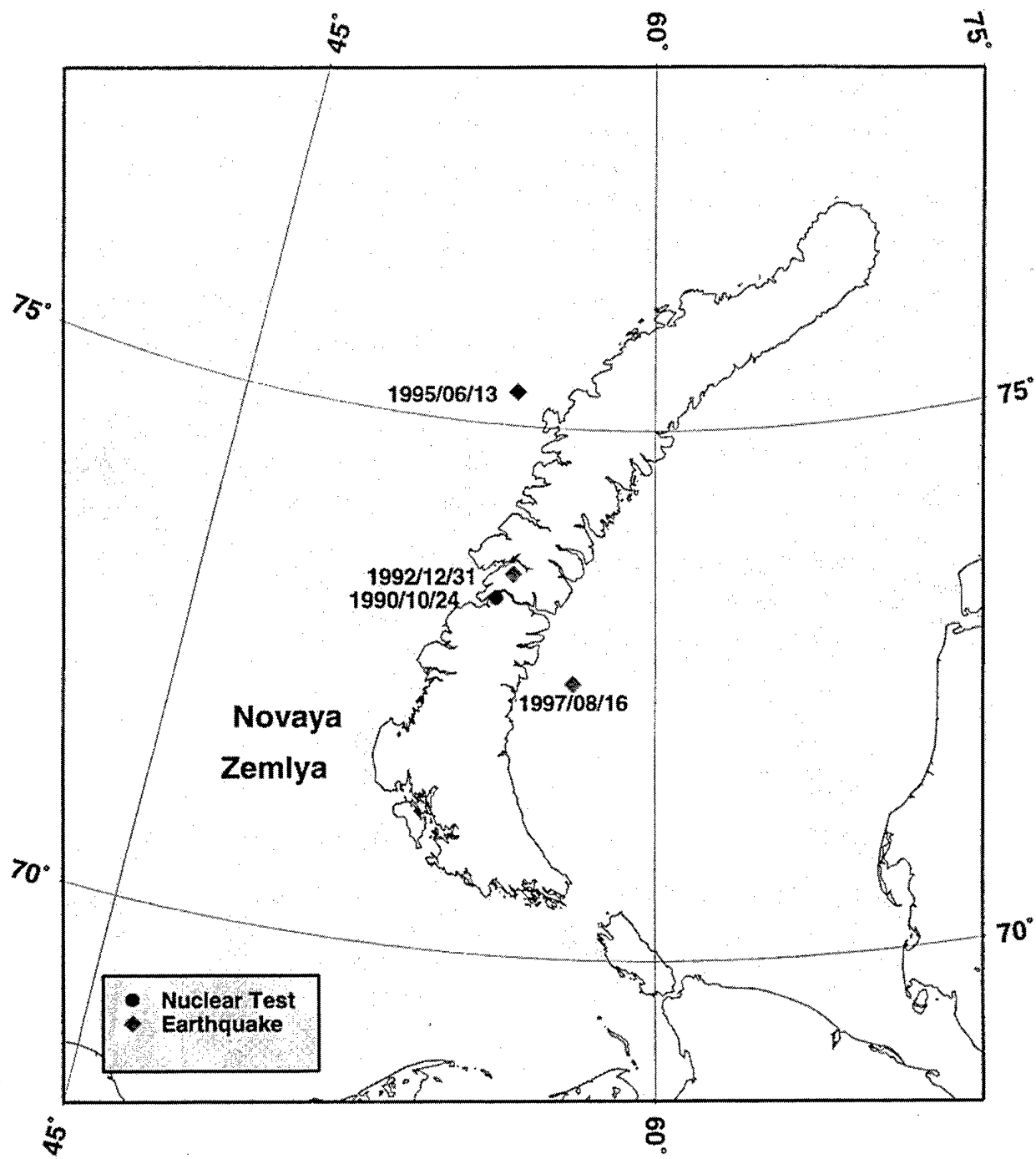


Figure 41. Events used in regional signal comparisons for the Kara Sea event of 1997/08/16.

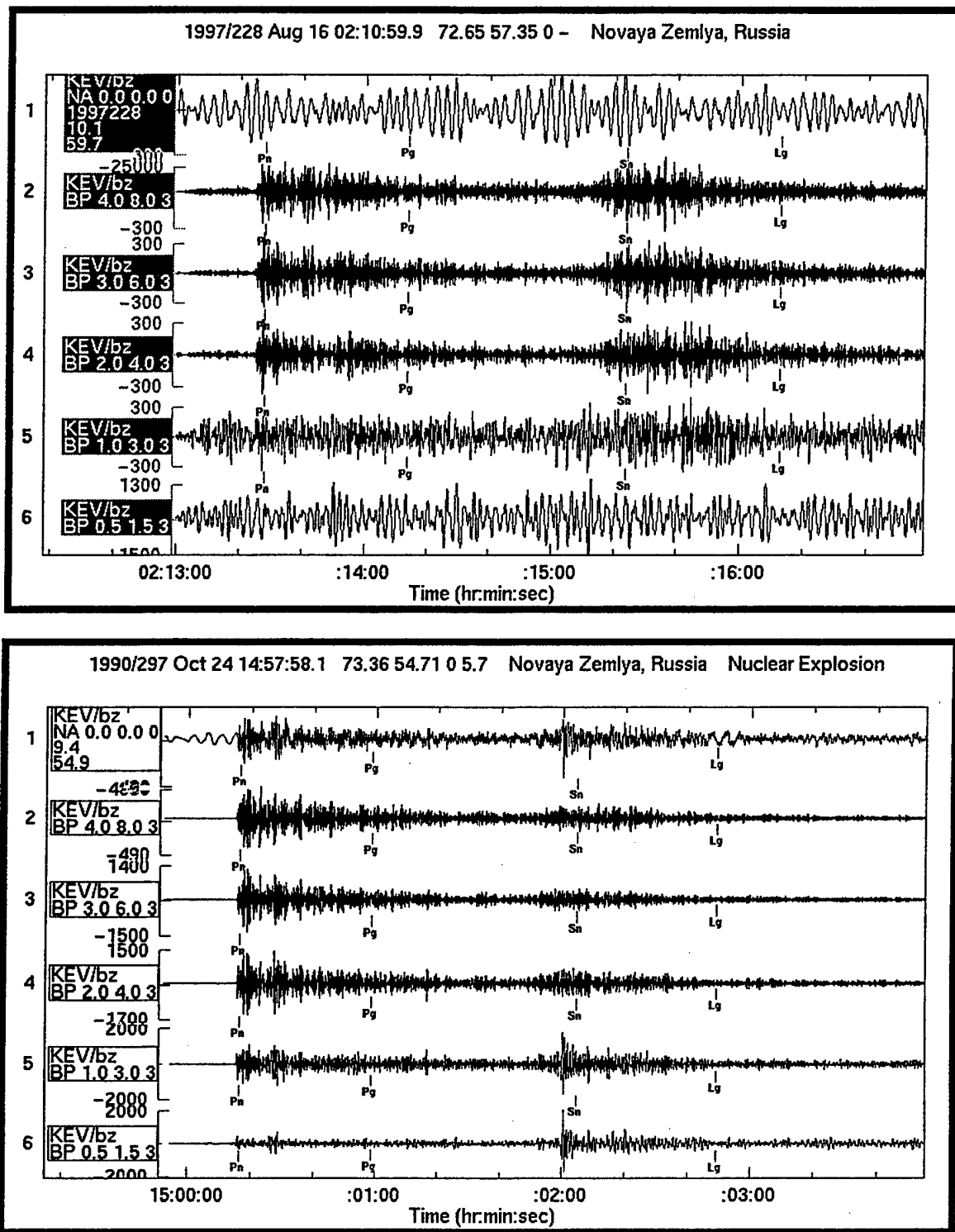


Figure 42. Comparison of band-pass filter analyses of the signals at station KEV for the 1997/08/16 Kara Sea event (top) and the 1990/10/24 NZ nuclear test (bottom)..

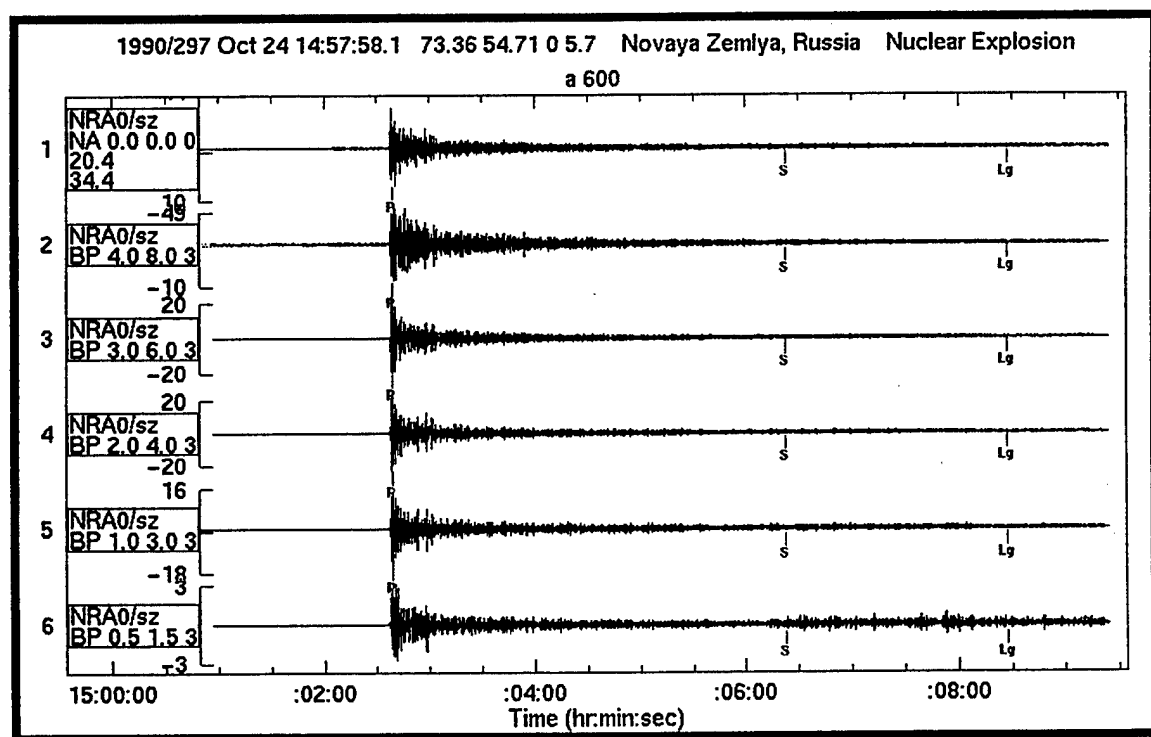
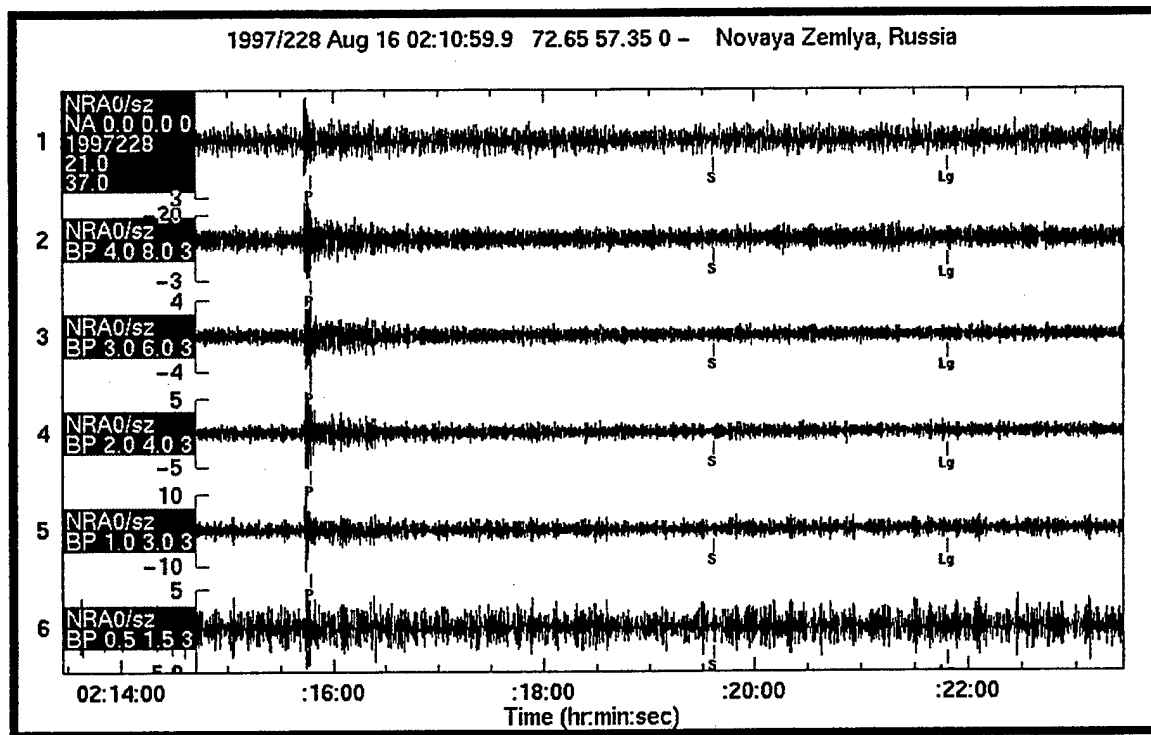


Figure 43. Comparison of band-pass filter analyses of the signals at station KEV for the 1997/08/16 Kara Sea event (top) and the 1990/10/24 NZ nuclear test (bottom)..

noise. The S/P ratio at the same station for the 1990/10/24 NZ nuclear was also very small. We found this to be true as well when we used theoretical yield-scaling relations to scale the record for the 1990/10/24 NZ explosion down to a yield equivalent to the 3.9  $m_b$  for the 1997/08/16 event; the scaling produced only minor effects on the S/P ratios in the individual passbands, although it could affect the broadband ratios more significantly. Because the regional S signal was masked by the noise for the 1997/08/16 event, the comparisons for NORESS could not be conclusive. However, it should be noted that the small S/P ratios seen at NORESS for the 1997/08/16 event was not like the behavior in the 1992/12/31 NZ event, where similar band-pass filter analyses showed that the signals in the regional S window were much stronger than P in the higher frequency passbands. So, at NORESS the behavior for the 1997/08/16 event appeared to be more explosion-like than for the 1992/12/31 event; but the S-to-P behavior at any single station could be affected by source radiation patterns or, in the case of the 1992 event, possibly by local noise. S/P ratios in similar passbands were generally found to be larger for the 1997/08/16 event at the nearer regional stations, although we do not have data available for direct comparisons with NZ nuclear explosions. Thus, the S/P ratios at Spitzbergen were about 0.5, at Norilsk about 1.0, and at Apatity the ratios were more than 2.0. This kind of variability in the S/P ratios between stations is not considered unusual since a tectonic source would be expected to have a radiation pattern which should produce variations in the S/P ratios at different azimuths.

### 5.3 S/P Ratios

Figures 44 - 47 compare S/P ratios as a function of frequency for the available regional stations from the four events near NZ shown on the map in Figure 41. The ratio measurements shown come from a band-pass filtering procedure which closely approximates Fourier spectral estimates for the regional phase group velocity windows. We show the ratios for all stations, although it is recognized that signal-to-noise conditions may degrade reliability of the measurements at some of the more-distant stations for the smaller events, as noted above. For the stations where direct comparisons are available between events, S/P ratios at higher frequencies (above about 2 Hz) are

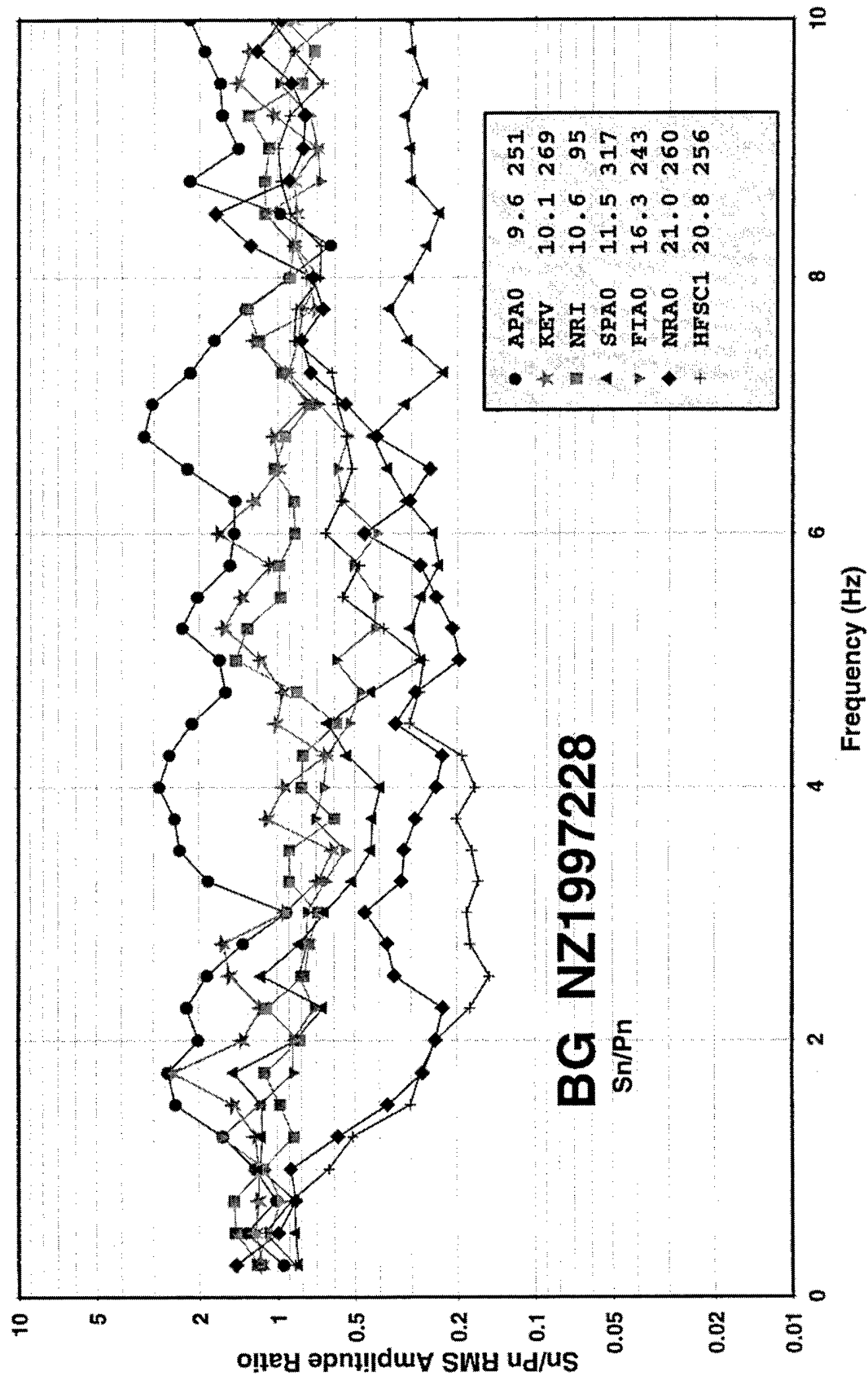


Figure 44. S/P ratios as a function of frequency observed at 7 regional stations from the 1997/08/16 Kara Sea event.

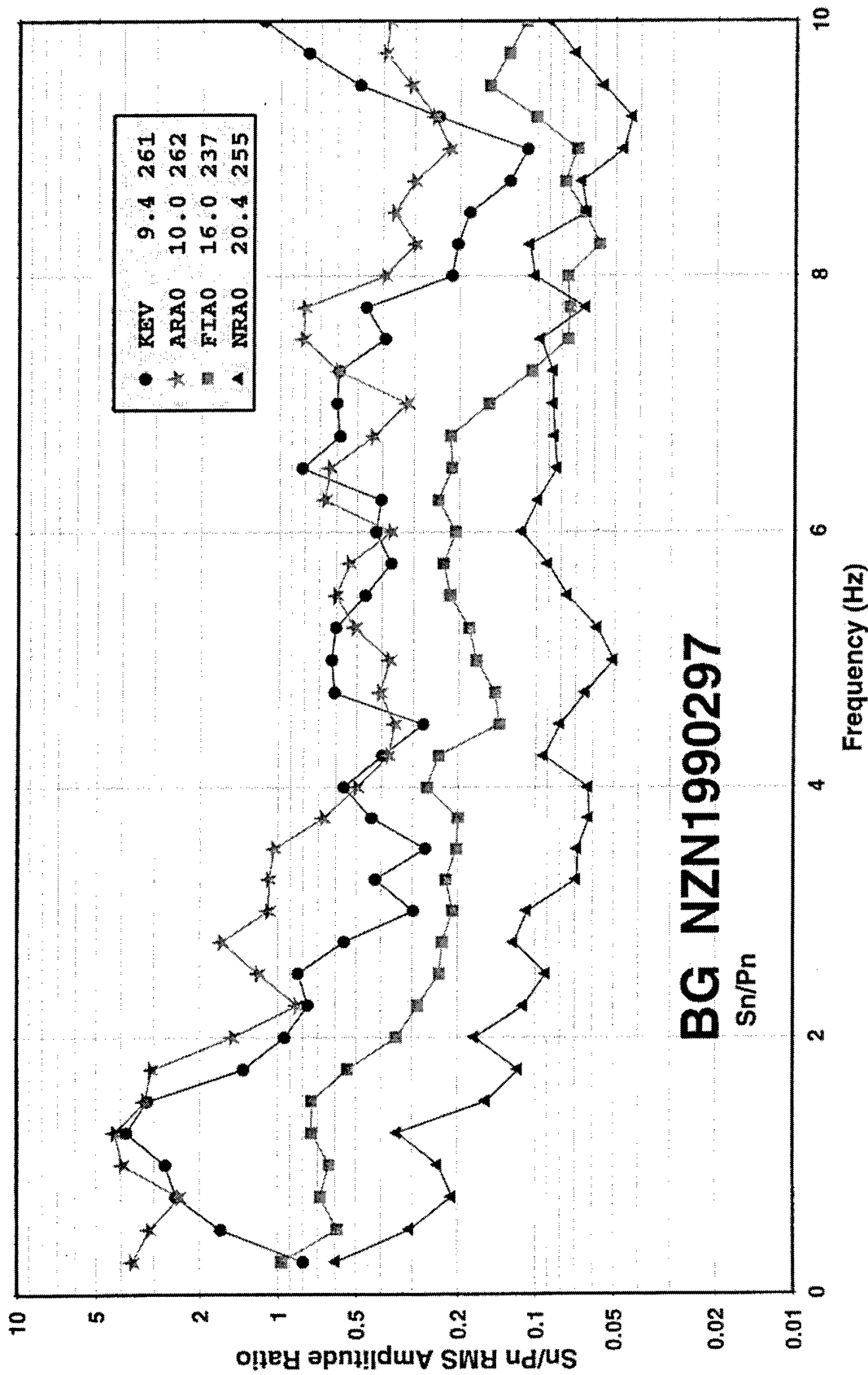


Figure 45. S/P ratios as a function of frequency observed at 4 regional stations from the 1990/10/24 NZ nuclear test.

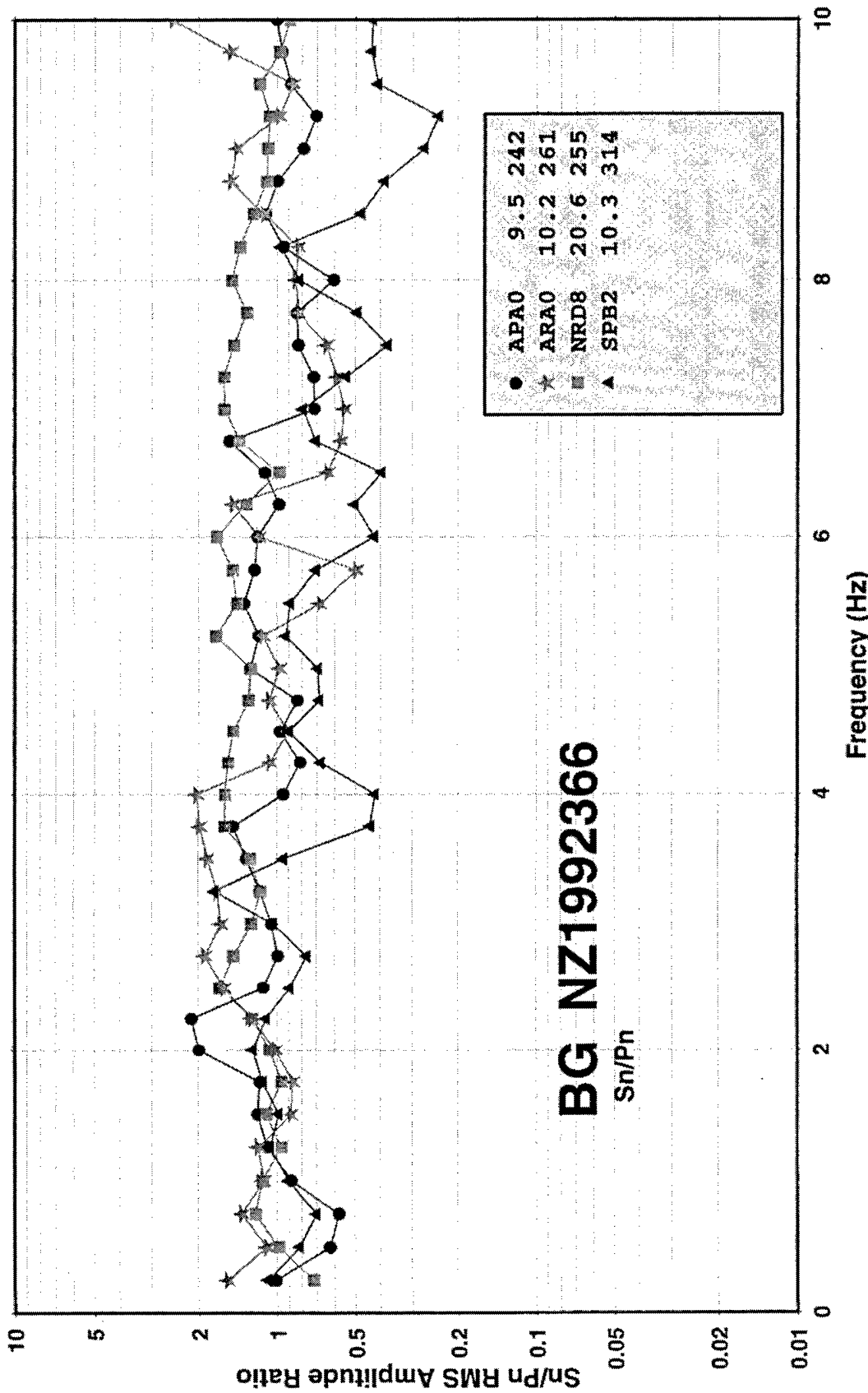


Figure 46. S/P ratios as a function of frequency observed at 4 regional stations from the 1992/12/31 event near NZ.

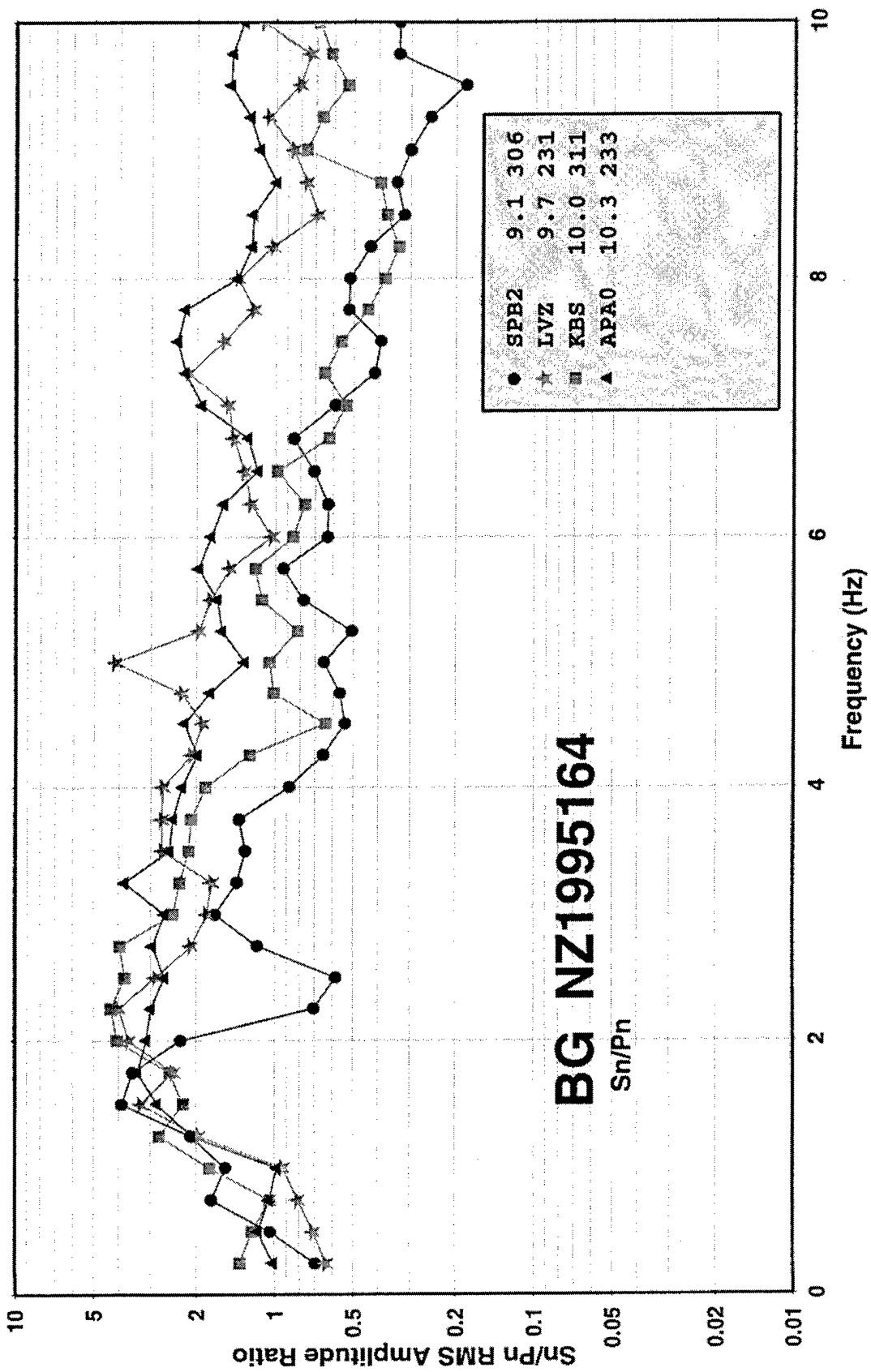


Figure 47. S/P ratios as a function of frequency observed at 4 regional stations from the 1995/06/13 event near NZ.

consistently larger for the 1997/08/16 NZ event than for the 1990/10/24 NZ nuclear explosion. This is consistent with our observation at station Kevo as discussed above in Figures 42 and 43. Similar direct comparisons of S/P ratios between the 1997/08/16 event and the 1992/12/31 and 1995/06/13 NZ events do not show consistent differences. Although S/P ratios at higher frequencies for the 1997/08/16 NZ event are lower (i.e. more explosion-like) than for the 1992/12/31 and 1995/06/13 events at some stations (e.g. Spitzbergen and NORESS), the S/P ratios are larger for the 1997/08/16 event at other stations (viz. Apatity). As noted above, this kind of variability in the S/P ratios may be explained by differences in the radiation patterns from these events which are all thought to be of tectonic origin.

#### **5.4 Horizontal Shear-Wave Observations**

Finally, we show in Figure 48 a comparison of the horizontal-component signals at four nearer regional stations for the 1997/08/16 NZ event. The N-S and E-W components for a filter passband 4 - 8 Hz are plotted one-above-the-other for each station. The strong regional S waves on the two horizontal components at three of the four stations (viz. Kevo, Norilsk, and Spitzbergen) may be another diagnostic that this event was not an explosion. Strong horizontal shear waves are generally not expected from a pure explosion source, although some horizontal shear motion is typically observed from many actual explosions. We have not systematically looked at horizontal-component regional S phases from underground nuclear explosion tests in the NZ area to verify whether the large horizontal shear waves from this 1997/08/16 event are significantly different from those seen for NZ explosions.

#### **5.5 Results of Discrimination Analysis**

In summary, we would conclude that the evidence presented strongly indicates that the 1997/08/16 event near NZ was not a nuclear explosion. We base this conclusion on the large regional S/P ratios and the strong regional S signals seen on two horizontal components at several stations. The behavior of the regional signals coupled with the offshore location of the event suggest that it was probably of tectonic origin.

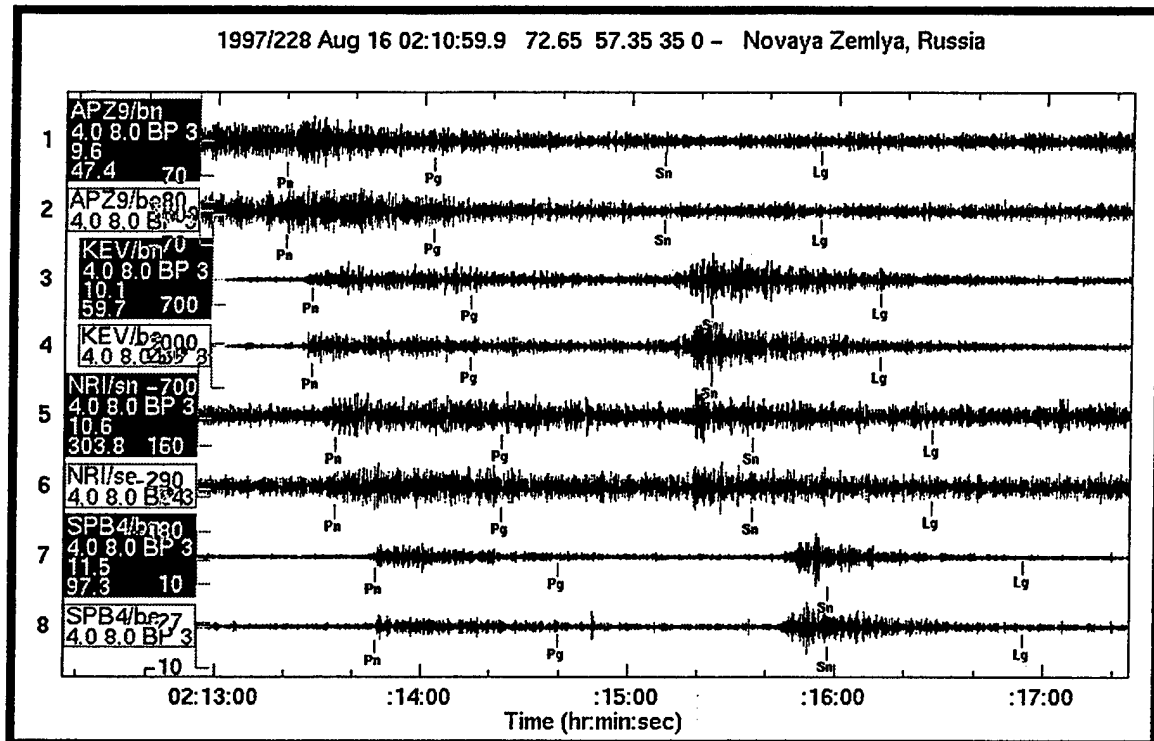


Figure 48. Horizontal-Component Records (4-8Hz Passband) at the 4 best regional stations for the 1997/08/16 Kara Sea event.

## 6. Summary and Recommendations

### 6.1 Summary of Main Findings

This research program included an empirical element and a theoretical element. In the empirical element we collected and analyzed the regional phase signals from representative samples of underground nuclear explosions, earthquakes, and other source types from a variety of source regions. We developed systematic procedures for measuring  $L_g/P$  ratios as a function of frequency; and we determined how  $L_g/P_g$  ratio measurements would likely be affected by regional attenuation and defined corrections which could be applied to specific source-station paths where the propagation effects were known.

After testing several algorithms for estimating the spectral content of regional phases, we settled on a Gaussian band-pass filtering procedure to measure the frequency-dependent  $L_g/P$  ratios. This method produces spectral estimates of regional phase amplitudes which essentially match those of Fourier methods. Although the method is slower than Fourier transforms, it offers some operational advantages. When we compared the different algorithms, we found that they seemed to make little difference in the overall behavior of the  $L_g/P$  ratio measurements; broader filters essentially produced smoothed versions of the Gaussian band-pass filter results.

Our preliminary analyses of  $L_g/P$  ratios as a function of frequency indicated that there were differences between the measurements for different source types, consistent with past experience which formed the basis for this discriminant. However, we also found that there were significant differences between the  $L_g/P$  ratios for similar source types in different regions and at different station distances. In these studies we have attempted to resolve whether these kinds of differences could be explained by propagation effects. We used a model for the known  $L_g$  attenuation and an assumed relationship between  $P_g$  and  $L_g$  attenuation to predict the effects of propagation on the  $L_g/P_g$  ratios. The predictions indicate that these propagation effects can be quite large, with the greatest effects occurring at high frequencies and large epicentral distances. When corrections based on the model were applied to a small sample of measurements,

we found some indications of a reduction in the scatter of the  $L_g/P_g$  ratios between similar events recorded at a common station. Considering the importance of this effect on  $L_g/P$  ratios, it seems likely that similar corrections could reduce the scatter in the observations, particularly when there are significant differences in the source-station distances or in the attenuation characteristics of the propagation paths.

In Section 4, we presented theoretical studies in which we developed synthetic seismograms and measured the corresponding  $L_g/P_g$  ratios for a range of crustal models representative of the diverse range of continental crust. The models included thick and thin crust, thick and thin sedimentary layers, and high and low moho velocities. We examined several Q models for these crustal models and determined the Green's functions corresponding to these models for sources at shallow and mid-crustal source depths. We used the synthetic seismograms resulting from these calculations to investigate the influence of source mechanism and propagation parameters on the  $L_g/P_g$  ratios.

We have found that simple attenuation models based on synthetic data exhibit large variance in the  $Q_0$  and  $\eta$ . Strong trade-off tendencies are observed in the population of crustal models and there are some systematic tendencies for some mechanisms. Our results suggest that Q's for  $P_g$  are not related to Q's for  $L_g$  by the simple 9/4's law and that the Q's for  $P_g$  may even be smaller than Q's for  $L_g$ , with some dependence upon source type being indicated. The results appear to indicate that, because  $P_g$  is composed of leaky P-SV modes, it may be controlled by the average shear-wave Q of the crust and not by the corresponding compressional wave Q.

It is possible to reproduce many of the gross features of  $L_g/P_g$  ratios as a function of frequency and range for explosions and earthquakes with layered crustal models. No great significances were found in the excitation by shallow CLVD, tension crack, or explosion sources at the same depth, although the different mechanisms do introduce variability into the ratios. Likewise, the synthetic ratios were not found to vary systematically for the three double-couple mechanisms, representing earthquake sources at mid-crustal depth. Much of the variability in the effectiveness of  $L_g/P_g$  ratio discriminants near 1 Hz can be explained by crustal structure variability. The most

significant structural factor affecting the synthetic  $L_g/P_g$  ratios was found to be the thickness of the sedimentary layers.

In order to generate realistic synthetic  $L_g/P_g$  amplitude ratios as a function of distance and frequency which agree with observations, we found that it was necessary to use a frequency dependent intrinsic Q. However, there could be significant biases between the observed frequency dependence of apparent  $L_g$  attenuation and the true intrinsic attenuation of the crust. The large scatter and biases between intrinsic attenuation of the crustal models and apparent attenuation is somewhat surprising and problematic from the standpoint of calibrating regional phase behavior and predicting discriminant performance.

As part of this research effort, we also performed a discrimination analysis on a seismic event which occurred on August 16, 1997 in the Kara Sea southeast of the former Soviet test site on Novaya Zemlya. This event could not be analyzed using  $L_g/P$  ratios because the  $L_g$  signals recorded at the available far-regional stations are too weak due to regional propagation conditions. We did apply similar band-pass filter analyses to the signals at common regional stations for this event and others from the same general area. We found that the S/P ratios above about 2 Hz were consistently larger for the 1997 Kara Sea event than for Novaya Zemlya nuclear explosions. This behavior was similar to that seen from past tectonic events from the same general area. The event also generated significant regional S on horizontal-components which suggested a tectonic source rather than an explosion.

## 6.2 Recommendations

These studies have revealed some of the strengths and weaknesses of  $L_g/P$  ratio measurements for use in event identification. Several issues have been raised where additional investigations should produce improved discrimination capability using these kinds of discriminants. First, the empirical studies suggest that  $L_g/P_g$  ratios as a function of frequency should be analyzed more fully to discern what frequency bands are likely to be most useful for effective discrimination. Although  $L_g/P$  ratios at high frequencies appear to provide the greatest distinction between source types, they are difficult to

observe, particularly at many of the farther regional stations which will be critical to CTBT monitoring. Furthermore, the higher frequency measurements are likely to be more sensitive to propagation effects. We need to develop greater understanding of noise limitations on high-frequency regional phase monitoring for all regions and stations of interest and to determine whether propagation uncertainties might also limit the frequencies at which  $L_g/P$  ratios can be effective. It seems likely that such limitations could diminish the value of the more distant stations for use in event discrimination.

The applicability of propagation corrections to spectral  $L_g/P$  ratios is currently severely limited by lack of knowledge of attenuation of regional P (including  $P_g$  and  $P_n$ ). We need to develop additional information on attenuation of  $P_g$  and  $P_n$ , comparable to that which is currently available for  $L_g$ , for the various source and propagation regions of interest in CTBT monitoring.

Once reliable regional P attenuation models have been developed and their relationship to  $L_g$  attenuation in the region has been determined, the models should be used to predict corrections to  $L_g/P$  ratio measurements as a function of frequency for the various regions. However, as discussed in connection with the theoretical modeling studies, development of these final corrections to the  $L_g/P$  measurements for propagation effects may also need to account for source mechanism and depth effects.

The theoretical modeling results have pointed out the need for several additional investigations to provide a firmer physical basis for the use of  $L_g/P_g$  ratios as discriminants and for understanding their performance in uncalibrated regions. Modeling implications from the Crust 5.1 regionalized model of Mooney et al. (1997) can and should be compared with additional data that are becoming available through the routine measurement of crustal phases at the preliminary International Data Center. The "crustal type" regionalization should be merged with attenuation models to produce and test more  $L_g/P_g$  ratios which have been collected in an automated manner.

Differences between the apparent attenuation of synthetic  $P_g$  and  $L_g$  from shallow explosion and mid-crustal double-couple mechanisms indicate that caution needs to be exercised in simply applying earthquake  $L_g$  Q to represent attenuation from both explosion and earthquake sources in all regions. The differential excitation of different

modes of  $P_g$  and  $L_g$  from shallow versus deep sources in some structures could lead to incorrect conclusions regarding the portability of  $L_g/P_g$  discriminants to regions where shallow events (e.g. depths  $< 1$  km) have not been calibrated.

The biases between apparent synthetic  $L_g$  Q and the intrinsic Q used to generate synthetic signal amplitudes indicate that our understanding of the crustal waveguide is still naïve. We should be cautious in applying observed  $L_g$  and coda Q for a region to compute synthetic seismograms. While these Q's can serve as excellent starting values, efforts to use synthetics to transport  $L_g/P_g$  discriminants require additional calibration against multiple source types, diverse attenuation levels, and multiple crustal structures.

## 7. References

Apsel, R. J. and J. E. Luco (1983). "On the Green's Functions for a Layered Half-Space. Part II," Bull. Seism. Soc. Am., 73, pp. 931 - 952.

Baumgardt, D. R., and G. B. Young (1990). "Regional Seismic Waveform Discriminants and Case-Based Event Identification Using Regional Arrays," Bull. Seism. Soc. Am., 80, pp. 1874 - 1892.

Bennett, T. J., B. W. Barker, K. L. McLaughlin, and J. R. Murphy (1989). "Regional Discrimination of Quarry Blasts, Earthquakes and Underground Nuclear Explosions," GL-TR-89-0114, ADA223148.

Bennett, T. J., A. K. Campanella, J. F. Scheimer, and J. R. Murphy (1992). "Demonstration of Regional Discrimination of Eurasian Seismic Events Using Observations at Soviet IRIS and CDSN Stations," PL-TR-92-2090, ADA253275.

Bennett, T. J., J. R. Murphy, M. E. Marshall, and B. W. Barker (1993). "A Preliminary Regional Seismic Discrimination Analysis of the Novaya Zemlya Event of December 31, 1992," in The Novaya Zemlya Event of 31 December 1992 and Seismic Identification Issues, edited by Alan Ryall, ARPA Report, 15<sup>th</sup> Seismic Research Symposium, 8-10 Sep 1993, Vail, Colorado, PL-TR-93-2160, ADA271458.

Bennett, T. J., B. W. Barker, M. E. Marshall, and J. R. Murphy (1995). "Detection and Identification of Small Regional Seismic Events," PL-TR-95-2125, ADA305536.

Bennett, T. J., K. L. McLaughlin, M. E. Marshall, J. L. Stevens (1997a). "The Physical Basis for the L<sub>g</sub>/P Discriminant: General Properties and Preliminary Modeling," Maxwell Report MFD-FR-97-15727, PL-TR-97-2044. ADA344175

Bennett, T. J., R. W. Cook, and J. A. Carter (1997b). "Seismic Discrimination with Regional Phase Spectral Ratios: Investigation of Transportability," Maxwell Report MFD-FR-97-15919, PL-TR-97-2140. ADA341313

Blandford, R. (1981). "Seismic Discrimination Problems at Regional Distances," in Identification of Seismic Source - Earthquake or Underground Explosion, D. Reidel Publishing Co., pp. 695-740.

Campillo, M., J. Plantet, M. Bouchon (1985). "Frequency Dependent Attenuation in the Crust Beneath Central France from L<sub>g</sub> Waves: Data Analysis and Numerical Modeling," Bull. Seism. Soc. Am., 75, pp. 1395 - 1411.

Dysart, P. S., and J. J. Pulli (1990). "Regional Seismic Event Classification at the NORESS Array: Seismological Measurements and the Use of Trained Neural Networks," Bull. Seism. Soc. Am., 80, pp. 1910 - 1933.

Goncz, J. H., W. C. Dean, Z. A. Der, A. C. Lees, K. L. McLaughlin, T. W. McElfresh, and M. E. Marshall (1985). "Propagation and Excitation of  $L_g$ ,  $S_n$ , and P- $P_n$  Waves from Eastern United States Earthquakes by Regression Analysis of RSTN Data," TGAL-86-7, Teledyne Geotech, Alexandria, VA.

Gupta, I. N., and K. L. McLaughlin (1987). "Attenuation of Ground Motion in the Eastern United States," Bull. Seism. Soc. Am., 77, pp. 366 - 383.

Harvey, D. J. (1992). "A Systematic Study of the Effects of Crust and Upper Mantle Structure on Regional Seismograms," PL-TR-92-2138, ADA260231.

McLaughlin, K. L., and B. Shkoller (1996). "Wavenumber Integration Synthetic Seismogram Calculations Using A Parallel Virtual Machine," PL-TR-96-2284, SSS-DTR-96-15561, ADA323186.

McLaughlin, K. L., B. Shkoller, D. E. Wilkins, and T. G. Barker (1997). "Advances in Numerical Analysis," Maxwell Laboratories Report MFD-TR-97-15, San Diego, CA, PL-TR-97-2150. ADA342321

Mitchell, B. J. (1981). "Regional Variations and Frequency Dependence of  $Q_\beta$  in the Crust of North America," Bull. Seism. Soc. Am., 71, pp. 1531 - 1538.

Mitchell, B. J. (1997). Personal Communication.

Mitchell, B. J., Y. Pan, and J. K. Xie (1996). "The Variation of  $L_g$  Coda Q Across Eurasia and Its Relation to Continental Evolution," PL-TR-96-2154, ADA317387.

Mooney, W.D, M.G. Laske, and T. G. Masters (1996). "CRUST 5.1: A Global Crustal Model at 5x5 Degrees," Journal of Geophysical Research (In Press).

Murphy, J. R., and T. J. Bennett (1982). "A Discrimination Analysis of Short-Period Regional Seismic Data Recorded at Tonto Forest Observatory," Bull. Seism. Soc. Am., 72, pp. 1351 - 1366.

Murphy, J. R., D. D. Sultanov, B. W. Barker, I. O. Kitov, and M. E. Marshall (1996). "Regional Seismic Detection Analyses of Selected Soviet Peaceful Nuclear Explosions," SSS-DFR-96-15503, PL-TR-96-2206, ADA323757.

Nuttli, O. W. (1981). "Similarities and Differences Between Western and Eastern United States Earthquakes, and Their Consequences for Earthquake Engineering," in *Earthquakes and Engineering; the Eastern United States*, J. E. Beavers, Editor, Ann Arbor Science Publishers, Ann Arbor, Michigan, pp. 25 - 51.

Pomeroy, P. W. (1977). "Aspects of Seismic Wave Propagation in Eastern North America - A Preliminary Report," Rondout Associates Report.

Pomeroy, P. W., and T. A. Nowak (1979). "An Investigation of Seismic Wave Propagation in Western USSR," Rondout Associates Semi-Annual Technical Report No. 2.

Pomeroy, P. W., W. J. Best, and T. V. McEvilly (1982). "Test Ban Treaty Verification with Regional Data - A Review," *Bull. Seism. Soc. Am.*, 72, pp. S89 - S129.

Ringdal, F. (1997). "Study of Low-Magnitude Seismic Events Near the Novaya Zemlya Nuclear Test Site," *Bull. Seism. Soc. Am.* (In Press).

SAC2000 Reference Manual, June 1995, LLNL, Livermore, CA, <http://www-ep.es.llnl.gov/tvp/sac.html>

Stevens, J. L., and K. L. McLaughlin (1997). "Improved Methods for Regionalized Surface Wave Analysis," Maxwell Laboratories Report MFD-TR-97-15887, San Diego, CA, PL-TR-97-2135. ADA337234

Taylor, S. R., M. D. Denny, E. S. Vergino, and R. E. Glaser (1989). "Regional Discrimination Between NTS Explosions and Western U. S. Earthquakes," *Bull. Seism. Soc. Am.*, 78, pp. 1142 - 1176.

Willis, D. E. (1963). "Comparison of Seismic Waves Generated by Different Types of Sources," *Bull. Seism. Soc. Am.*, 53, pp. 965 - 978.

Willis, D. E., J. DeNoyer, and J. T. Wilson (1963). "Differentiation of Earthquakes and Underground Nuclear Explosions on the Basis of Amplitude Characteristics," *Bull. Seism. Soc. Am.*, 53, pp. 979 - 987.

Xie, J. K., and B. J. Mitchell (1990). "A Back-Projection Method for Imaging Large-Scale Lateral Variations of Lg Coda Q with Application to Continental Africa," *Geophys. Jour. Int.*, 100, pp. 161 - 181.

THOMAS AHRENS  
SEISMOLOGICAL LABORATORY 252-21  
CALIFORNIA INST. OF TECHNOLOGY  
PASADENA, CA 91125

AIR FORCE RESEARCH LABORATORY  
ATTN: VSOE  
29 RANDOLPH ROAD  
HANSOM AFB, MA 01731-3010 (2 COPIES)

AIR FORCE RESEARCH LABORATORY  
ATTN: RESEARCH LIBRARY/TL  
5 WRIGHT STREET  
HANSOM AFB, MA 01731-3004

AIR FORCE RESEARCH LABORATORY  
ATTN: AFRL/SUL  
3550 ABERDEEN AVE SE  
KIRTLAND AFB, NM 87117-5776 (2 COPIES)

RALPH ALEWINE  
NTPO  
1901 N. MOORE STREET, SUITE 609  
ARLINGTON, VA 22209

MUAWIA BARAZANGI  
INSTOC  
3126 SNEE HALL  
CORNELL UNIVERSITY  
ITHACA, NY 14853

T.G. BARKER  
MAXWELL TECHNOLOGIES  
8888 BALBOA AVE.  
SAN DIEGO, CA 92123-1506

DOUGLAS BAUMGARDT  
ENSCO INC.  
5400 PORT ROYAL ROAD  
SPRINGFIELD, VA 22151

THON J. BENNETT  
MAXWELL TECHNOLOGIES  
11800 SUNRISE VALLEY  
SUITE 1212  
RESTON, VA 22091

WILLIAM BENSON  
NAS/COS  
ROOM HA372  
2001 WISCONSIN AVE. NW  
WASHINGTON DC 20007

JONATHAN BERGER  
UNIV. OF CALIFORNIA, SAN DIEGO  
SCRIPPS INST. OF OCEANOGRAPHY IGPP, 0225  
9500 GILMAN DRIVE  
LA JOLLA, CA 92093-0225

ROBERT BLANDFORD  
AFTAC  
1300 N. 17TH STREET  
SUITE 1450  
ARLINGTON, VA 22209-2308

LESLIE A. CASEY  
DEPT. OF ENERGY/NN-20  
1000 INDEPENDENCE AVE. SW  
WASHINGTON DC 20585-0420

CENTER FOR MONITORING RESEARCH  
ATTN: LIBRARIAN  
1300 N. 17th STREET, SUITE 1450  
ARLINGTON, VA 22209

ANTON DAINTY  
HQ DSWA/PMA  
6801 TELEGRAPH ROAD  
ALEXANDRIA, VA 22310-3398

CATHERINE DE GROOT-HEDLIN  
UNIV. OF CALIFORNIA, SAN DIEGO  
IGPP  
8604 LA JOLLA SHORES DRIVE  
SAN DIEGO, CA 92093

DIANE DOSER  
DEPT. OF GEOLOGICAL SCIENCES  
THE UNIVERSITY OF TEXAS AT EL PASO  
EL PASO, TX 79968

DTIC  
8725 JOHN J. KINGMAN ROAD  
FT BELVOIR, VA 22060-6218 (2 COPIES)

MARK D. FISK  
MISSION RESEARCH CORPORATION  
735 STATE STREET  
P.O. DRAWER 719  
SANTA BARBARA, CA 93102-0719

LORI GRANT  
MULTIMAX, INC.  
311C FOREST AVE. SUITE 3  
PACIFIC GROVE, CA 93950

HENRY GRAY  
SMU STATISTICS DEPARTMENT  
P.O. BOX 750302  
DALLAS, TX 75275-0302

I. N. GUPTA  
MULTIMAX, INC.  
1441 MCCORMICK DRIVE  
LARGO, MD 20774

DAVID HARKRIDER  
BOSTON COLLEGE  
INSTITUTE FOR SPACE RESEARCH  
140 COMMONWEALTH AVENUE  
CHESTNUT HILL, MA 02167

MICHAEL HEDLIN  
UNIVERSITY OF CALIFORNIA, SAN DIEGO  
SCRIPPS INST. OF OCEANOGRAPHY  
9500 GILMAN DRIVE  
LA JOLLA, CA 92093-0225

EUGENE HERRIN  
SOUTHERN METHODIST UNIVERSITY  
DEPT. OF GEOLOGICAL SCIENCES  
DALLAS, TX 75275-0395

VINDELL HSU  
HQ/AFTAC/TTR  
1030 S. HIGHWAY A1A  
PATRICK AFB, FL 32925-3002

THOMAS JORDAN  
MASS. INST. OF TECHNOLOGY  
BLDG 54-918  
CAMBRIDGE, MA 02139

LAWRENCE LIVERMORE NAT'L LAB  
ATTN: TECHNICAL STAFF (PLS ROUTE)  
PO BOX 808, MS L-208  
LIVERMORE, CA 94551

LAWRENCE LIVERMORE NAT'L LAB  
ATTN: TECHNICAL STAFF (PLS ROUTE)  
PO BOX 808, MS L-195  
LIVERMORE, CA 94551

LAWRENCE LIVERMORE NAT'L LAB  
ATTN: TECHNICAL STAFF (PLS ROUTE)  
PO BOX 808, MS L-200  
LIVERMORE, CA 94551

THORNE LAY  
UNIV. OF CALIFORNIA, SANTA CRUZ  
EARTH SCIENCES DEPARTMENT  
EARTH & MARINE SCIENCE BUILDING  
SANTA CRUZ, CA 95064

THOMAS HEARN  
NEW MEXICO STATE UNIVERSITY  
DEPARTMENT OF PHYSICS  
LAS CRUCES, NM 88003

DONALD HELMBERGER  
CALIFORNIA INST. OF TECHNOLOGY  
DIV. OF GEOL. & PLANETARY SCIENCES  
SEISMOLOGICAL LABORATORY  
PASADENA, CA 91125

ROBERT HERRMANN  
ST. LOUIS UNIVERSITY  
DEPT. OF EARTH & ATMOS. SCIENCES  
3507 LACLEDE AVENUE  
ST. LOUIS, MO 63103

RONG-SONG JIH  
HQ DSWA/PMA  
6801 TELEGRAPH ROAD  
ALEXANDRIA, VA 22310-3398

LAWRENCE LIVERMORE NAT'L LAB  
ATTN: TECHNICAL STAFF (PLS ROUTE)  
PO BOX 808, MS L-175  
LIVERMORE, CA 94551

LAWRENCE LIVERMORE NAT'L LAB  
ATTN: TECHNICAL STAFF (PLS ROUTE)  
PO BOX 808, MS L-202  
LIVERMORE, CA 94551

LAWRENCE LIVERMORE NAT'L LAB  
ATTN: TECHNICAL STAFF (PLS ROUTE)  
PO BOX 808, MS L-205  
LIVERMORE, CA 94551

LAWRENCE LIVERMORE NAT'L LAB  
ATTN: TECHNICAL STAFF (PLS ROUTE)  
PO BOX 808, MS L-221  
LIVERMORE, CA 94551

ANATOLI L. LEVSHIN  
DEPARTMENT OF PHYSICS  
UNIVERSITY OF COLORADO  
CAMPUS BOX 390  
BOULDER, CO 80309-0309

JAMES LEWKOWICZ  
WESTON GEOPHYSICAL CORP.  
325 WEST MAIN STREET  
NORTHBORO, MA 01532

LOS ALAMOS NATIONAL LABORATORY  
ATTN: TECHNICAL STAFF (PLS ROUTE)  
PO BOX 1663, MS F665  
LOS ALAMOS, NM 87545

GARY MCCARTOR  
SOUTHERN METHODIST UNIVERSITY  
DEPARTMENT OF PHYSICS  
DALLAS, TX 75275-0395

BRIAN MITCHELL  
DEPARTMENT OF EARTH & ATMOSPHERIC SCIENCES  
ST. LOUIS UNIVERSITY  
3507 LACLEDE AVENUE  
ST. LOUIS, MO 63103

JOHN MURPHY  
MAXWELL TECHNOLOGIES  
11800 SUNRISE VALLEY DRIVE  
SUITE 1212  
RESTON, VA 22091

ROBERT NORTH  
CENTER FOR MONITORING RESEARCH  
1300 N. 17th STREET, SUITE 1450  
ARLINGTON, VA 22209

JOHN ORCUTT  
INST. OF GEOPH. & PLANETARY PHYSICS  
UNIV. OF CALIFORNIA, SAN DIEGO  
LA JOLLA, CA 92093

PACIFIC NORTHWEST NAT'L LAB  
ATTN: TECHNICAL STAFF (PLS ROUTE)  
PO BOX 999, MS K6-40  
RICHLAND, WA 99352

PACIFIC NORTHWEST NAT'L LAB  
ATTN: TECHNICAL STAFF (PLS ROUTE)  
PO BOX 999, MS K5-12  
RICHLAND, WA 99352

KEITH PRIESTLEY  
DEPARTMENT OF EARTH SCIENCES  
UNIVERSITY OF CAMBRIDGE  
MADINGLEY RISE, MADINGLEY ROAD  
CAMBRIDGE, CB3 0EZ UK

LOS ALAMOS NATIONAL LABORATORY  
ATTN: TECHNICAL STAFF (PLS ROUTE)  
PO BOX 1663, MS F659  
LOS ALAMOS, NM 87545

LOS ALAMOS NATIONAL LABORATORY  
ATTN: TECHNICAL STAFF (PLS ROUTE)  
PO BOX 1663, MS C335  
LOS ALAMOS, NM 87545

KEITH MCLAUGHLIN  
CENTER FOR MONITORING RESEARCH  
SAIC  
1300 N. 17TH STREET, SUITE 1450  
ARLINGTON, VA 22209

RICHARD MORROW  
USACDA/IVI  
320 21ST STREET, N.W.  
WASHINGTON DC 20451

JAMES NI  
NEW MEXICO STATE UNIVERSITY  
DEPARTMENT OF PHYSICS  
LAS CRUCES, NM 88003

OFFICE OF THE SECRETARY OF DEFENSE  
DDR&E  
WASHINGTON DC 20330

PACIFIC NORTHWEST NAT'L LAB  
ATTN: TECHNICAL STAFF (PLS ROUTE)  
PO BOX 999, MS K6-48  
RICHLAND, WA 99352

PACIFIC NORTHWEST NAT'L LAB  
ATTN: TECHNICAL STAFF (PLS ROUTE)  
PO BOX 999, MS K6-84  
RICHLAND, WA 99352

FRANK PILOTTE  
HQ AFTAC/TT  
1030 S. HIGHWAY A1A  
PATRICK AFB, FL 32925-3002

JAY PULLI  
BBN SYSTEMS AND TECHNOLOGIES, INC.  
1300 NORTH 17TH STREET  
ROSSLYN, VA 22209

DELAIN REITER  
AFRL/VSOE (SENCOM)  
73 STANDISH ROAD  
WATERTOWN, MA 02172

MICHAEL RITZWOLLER  
DEPARTMENT OF PHYSICS  
UNIVERSITY OF COLORADO  
CAMPUS BOX 390  
BOULDER, CO 80309-0309

CHANDAN SAIKIA  
WOODWARD-CLYDE FED. SERVICES  
566 EL DORADO ST., SUITE 100  
PASADENA, CA 91101-2560

SANDIA NATIONAL LABORATORY  
ATTN: TECHNICAL STAFF (PLS ROUTE)  
DEPT. 9311  
MS 1159, PO BOX 5800  
ALBUQUERQUE, NM 87185-1159

SANDIA NATIONAL LABORATORY  
ATTN: TECHNICAL STAFF (PLS ROUTE)  
DEPT. 5736  
MS 0655, PO BOX 5800  
ALBUQUERQUE, NM 87185-0655

AVI SHAPIRA  
SEISMOLOGY DIVISION  
IPRG  
P.O.B. 2286 NOLON 58122 ISRAEL

MATTHEW SIBOL  
ENSCO, INC.  
445 PINEDA CT.  
MELBOURNE, FL 32940

JEFFRY STEVENS  
MAXWELL TECHNOLOGIES  
8888 BALBOA AVE.  
SAN DIEGO, CA 92123-1506

TACTEC  
BATTELLE MEMORIAL INSTITUTE  
505 KING AVENUE  
COLUMBUS, OH 43201 (FINAL REPORT)

LAWRENCE TURNBULL  
ACIS  
DCI/ACIS  
WASHINGTON DC 20505

PAUL RICHARDS  
COLUMBIA UNIVERSITY  
LAMONT-DOHERTY EARTH OBSERV.  
PALISADES, NY 10964

DAVID RUSSELL  
HQ AFTAC/TTR  
1030 SOUTH HIGHWAY A1A  
PATRICK AFB, FL 32925-3002

SANDIA NATIONAL LABORATORY  
ATTN: TECHNICAL STAFF (PLS ROUTE)  
DEPT. 5704  
MS 0979, PO BOX 5800  
ALBUQUERQUE, NM 87185-0979

SANDIA NATIONAL LABORATORY  
ATTN: TECHNICAL STAFF (PLS ROUTE)  
DEPT. 5704  
MS 0655, PO BOX 5800  
ALBUQUERQUE, NM 87185-0655

THOMAS SERENO JR.  
SAIC  
10260 CAMPUS POINT DRIVE  
SAN DIEGO, CA 92121

ROBERT SHUMWAY  
410 MRAK HALL  
DIVISION OF STATISTICS  
UNIVERSITY OF CALIFORNIA  
DAVIS, CA 95616-8671

DAVID SIMPSON  
IRIS  
1200 NEW YORK AVE., NW  
SUITE 800  
WASHINGTON DC 20005

BRIAN SULLIVAN  
BOSTON COLLEGE  
INSTITUTE FOR SPACE RESEARCH  
140 COMMONWEALTH AVENUE  
CHESTNUT HILL, MA 02167

NAFI TOKSOZ  
EARTH RESOURCES LABORATORY  
M.I.T.  
42 CARLTON STREET, E34-440  
CAMBRIDGE, MA 02142

GREG VAN DER VINK  
IRIS  
1200 NEW YORK AVE., NW  
SUITE 800  
WASHINGTON DC 20005

FRANK VERNON  
UNIV. OF CALIFORNIA, SAN DIEGO  
SCRIPPS INST. OF OCEANOGRAPHY  
9500 GILMAN DRIVE  
LA JOLLA, CA 92093-0225

JILL WARREN  
LOS ALAMOS NATIONAL LABORATORY  
GROUP NIS-8  
P.O. BOX 1663  
LOS ALAMOS, NM 87545      (5 COPIES)

RU SHAN WU  
UNIV. OF CALIFORNIA, SANTA CRUZ  
EARTH SCIENCES DEPT.  
1156 HIGH STREET  
SANTA CRUZ, CA 95064

JAMES E. ZOLLWEG  
BOISE STATE UNIVERSITY  
GEOSCIENCES DEPT.  
1910 UNIVERSITY DRIVE  
BOISE, ID 83725

TERRY WALLACE  
UNIVERSITY OF ARIZONA  
DEPARTMENT OF GEOSCIENCES  
BUILDING #77  
TUCSON, AZ 85721

DANIEL WEILL  
NSF  
EAR-785  
4201 WILSON BLVD., ROOM 785  
ARLINGTON, VA 22230

JIAKANG XIE  
COLUMBIA UNIVERSITY  
LAMONT DOHERTY EARTH OBSERV.  
ROUTE 9W  
PALISADES, NY 10964